LBL-22433
c.2

Lawrence Berkeley Laboratory
UNIVERSITY OF CALIFORNIA

Physics Division

RECEIVED
BY THE LIBRARY
MAR 2 1987
GOVERNMENT DOCUMENTS SECTION

HARD PHOTON PROCESSES IN ELECTRON-POSITRON ANNIHILATION AT 29 GeV

M.S. Gold
(Ph.D. Thesis)

November 1986

TWO-WEEK LOAN COPY
This is a Library Circulating Copy which may be borrowed for two weeks.

Prepared for the U.S. Department of Energy under Contract DE-AC03-76SF00098

LBL-22433
c.2

DISCLAIMER

This document was prepared as an account of work sponsored by the United States Government. While this document is believed to contain correct information, neither the United States Government nor any agency thereof, nor the Regents of the University of California, nor any of their employees, makes any warranty, express or implied, or assumes any legal responsibility for the accuracy, completeness, or usefulness of any information, apparatus, product, or process disclosed, or represents that its use would not infringe privately owned rights. Reference herein to any specific commercial product, process, or service by its trade name, trademark, manufacturer, or otherwise, does not necessarily constitute or imply its endorsement, recommendation, or favoring by the United States Government or any agency thereof, or the Regents of the University of California. The views and opinions of authors expressed herein do not necessarily state or reflect those of the United States Government or any agency thereof or the Regents of the University of California.

LBL-22433

Hard Photon Processes in Electron-Positron Annihilation at 29 GeV

Michael Steven Gold
(Ph.D. Thesis)

Lawrence Berkeley Laboratory
University of California
Berkeley, California 94720

November 1986

This work was supported by the Director, Office of Energy Research, Office of High Energy and Nuclear Physics, Division of High Energy Physics of the U.S. Department of Energy under Contract Number DE-AC03-76SF00098.

Hard Photon Processes in Electron-Positron Annihilation at 29 GeV

Michael Steven Gold

ABSTRACT

The hard photon processes $\mu\mu\gamma$ and hadrons + γ in e^+e^- annihilation at 29 GeV have been studied. The study is based on an integrated luminosity of 226 pb^{-1} taken at PEP with the Mark II detector. For the $\mu\mu\gamma$ process, a small fraction of non-planar events are observed with missing momentum along the beam direction. The resulting missing energy spectrum is consistent with that expected from higher order effects. The observed cross section is consistent with the predicted cross section for this process, $\sigma^{exp}/\sigma^{th} = .90 \pm .05 \pm .06$. The observed hard photon energy spectrum and mass distributions are found to be in agreement with $O(\alpha^3)$ QED. The measured charge asymmetry is in good agreement with the predicted value, $A_{exp}/A_{th} = .83 \pm .25 \pm .12$. The $\mu\gamma$ invariant mass distribution is used to place a limit on a possible excited muon coupling G_γ/M^* for excited muon masses in the range $1 < M^* < 21$ GeV of $(G_\gamma/M^*)^2 < 10^{-5}$ GeV^{-2} at a 95% confidence level. In the hadrons + γ process, evidence for final state radiation is found in an excess of events over that predicted from initial state radiation alone of $253 \pm 54 \pm 60$ events. Further evidence for final state radiation is found in a large hadronic charge asymmetry, $A_{\mathrm{Had}+\gamma} = (-24.6 \pm 5.5)\%$.

To my father, who inspired me to achieve all that I can
and taught me to never lose my sense of humor.

Acknowledgments

The Mark II experiment is "big" physics, and as such it is the result of the continuous devotion of a large number of people over a long period of time. I would like to thank the entire Berkeley-Stanford-Harvard collaboration, both past and present, for their dedication and hard work.

Special thanks goes to my advisor, Gerson Goldhaber, for his insight, experience, patience, enthusiasm, and , above all , humanity. Thanks also to George Trilling, George Gidal, Gerry Abrams, Martin Perl and Alfred Peterson for comments, criticism and frequent consultations. Thanks to Paul Tsai, Bob Cahn, and Stan Brodsky for useful and inspiring discussions.

Of those who formally taught me physics, I would like to thank in particular John McIntosh of Wesleyan University and Eugene Commins and Mahiko Suzuki of U.C. Berkeley. For teaching me physics on an informal basis I would like to thank my fellow graduate students.

On a personal level, I would like to thank my family for love, encouragement, and endless support: my mother Zelda, my brother Bruce, my in-laws Lou and Jim, and above all my wife Meg. Thanks to Peter Rowson for close companionship, endless good humor, and setting the fashion trend at the lab. Thanks to my office-mate Drew Baden for his devoted friendship and inimitable computer wizardry.

Finally, I would like to thank all those people in Pittsburgh, PA who helped me to see this day.

Table of Contents

Acknowledgments i

1. Introduction 1

1.1 The $\mu\mu\gamma$ Process 2

1.1.1 Cross section 3

1.1.2 Asymmetry 4

1.1.3 Excited muons 7

1.2 The Hadrons+ γ Process 11

2. The Mark II Detector 16

2.1 Vertex Chamber 16

2.2 Main Drift Chamber 18

2.3 Time of Flight 19

2.4 Magnet Coil 19

2.5 Liquid Argon System 19

2.6 Endcaps 24

2.7 Muon System 24

2.8 Small Angle Tagging System 24

2.9 Triggering 25

3. The $\mu\mu\gamma$ Process 26

3.1 Normalization 26

3.2 Event Selection 29

3.3 Angular resolution 32

3.4 Higher order correction and infrared divergence 37

3.5 Monte Carlo Generator 44

3.6 Kinematic fitting 45

3.7 Fitted distributions 54

3.8 Asymmetry 54

3.9 μ^* coupling limit 58

3.9.1 μ^* Monte Carlo 58

3.9.2 Maximum likelihood limit 60
4. Hadrons + γ 68
4.1 Event Selection 68
4.2 Jet axes 71
4.3 Direct Photon Spectrum 73
4.4 Charge Asymmetry 75
4.5 Monte Carlo 82
5. Conclusion 96
Appendix A. Charge Asymmetry 97
Appendix B. Estimate of $\pi\pi\gamma$ background 100
Appendix C. Statistical error on asymmetry 102
Appendix D. μ^* formulae 103
D.1 Decay rate 103
D.2 Two body phase space 103
D.3 P* parameterization 104
REFERENCES 106

1. Introduction

Although initially suprising, the abundent production of hard photons (photon energy $k > .5$ GeV) in e^+e^- annihilation at 29 GeV is a simple consequence of quantum electrodynamics (QED). [1] In lowest order the annihilation process proceeds via the one photon virtual intermediate state. This is the so-called s channel process because the virtual photon propagates with momentum $q^2 = s$, where s is the square of the e^+e^- center of mass energy. In the absence of any mass scale, the cross section will be inversely proportional to s. The higher order process of hard photon production contains an additional factor α/k due to the real photon emission. However, if the photon is emitted in the initial state then the annihilation occurs at the reduced center of mass energy squared, $s' = s(1 - 2k/\sqrt{s})$. The reduced center of mass can become quite small, being limited only by the threshold for producing the mass of the final state. The effect of this reduced center of mass after photon emission is therefore to increase the cross section for hard photon emission to $\sim 10\%$ of the lowest order cross section.

The annihilation process produces all pairs of charged fermions above threshold. Hadronic final states are considered to be the result of the production of a quark, anti-quark pair which hadronize as a result of long distance strong interactions. This property of confinement is believed to be a consequence of the theory of strong interactions, quantum chromodynamics (QCD). For leptonic final states the threshold is simply twice the lepton mass, whereas for hadrons it is the mass of the lowest lying hadronic state, twice the pion mass. In the standard model the strong, weak and electromagnetic forces are represented by the gauge bosons of $SU(3)_{color} \otimes SU(2)_L \otimes U(1)_Y$. The weak and electromagnetic forces are unified in the Glashow-Weinberg-Salam model of weak isospin $SU(2)_L$ and hypercharge $U(1)_Y$. The photon (and QED) emerge after spontaneous breaking of this symmetry via the Higgs mechanism as the gauge boson of the remaining unbroken $U(1)_{EM}$

symmetry. As in simple QED the photon then couples to the electromagnetic current via the minimal coupling, $\mathcal{L}_{int} = -ej \cdot A$. The current j_μ, given by

$$j_\mu = \sum_i q_i \bar{\psi}_i \gamma_\mu \psi_i,$$

is the usual Dirac current for pointlike fermions of charge q_i in units of the electric charge $e = |e|$. The known elementary charged fermions are the charged leptons e, μ, τ and the quarks u, d, s, c, b. Muon pair production allows us to study the annihilation process in its simplest form, without the complications of the weak decay modes of the τ or the hadronization of the quarks. For this reason, μ-pair production is essential to e^+e^- physics, and we begin our study of hard photons with μ-pairs. This is important in itself as a direct test of higher order QED as well as being preliminary to the study of hard photon hadronic events. The study of hard photons hadronic events has been recognized as an important test of the quark hypothesis, the pointlike coupling of quarks to photons, and short distance QCD. [2 3 4]

1.1 THE $\mu\mu\gamma$ PROCESS

The study of radiative muon pair production is important as a direct test of higher order QED. QED is an enormously successful theory. [5] It is the prototype for all locally gauge-invariant relativistic quantum field theories, and in particular for those constituting the standard model. The success of the theory rests on the smallness of the coupling constant $\alpha \approx 1/137$ and the ability to carry out the perturbation expansion in this parameter. The contributions of successive terms become smaller in this expansion after infinities are removed by the well known technique of renormalization. That the finite contributions of higher order terms get more important at higher energies is then best understood within the framework of the renormalization group where the coupling constant α is replaced by the running coupling constant $\alpha(s)$ defined at the energy scale $\sqrt{s}$. The contributions to $\alpha(s)$

come from the vacuum polarization and in the pure electroweak theory are given by, [6]

$$\alpha(s) = \alpha\Big\{1 + \frac{\alpha}{3\pi}\sum_i q_i^2\theta(s - m_i^2)\log(\frac{s}{m_i^2})\Big\}$$

where the sum is over all particles of mass m_i coupling to the photon and θ is the step function. (To account for QCD effects, the sum over the quarks is usually replaced by a dispersion relation.) As we go to higher energy, the running coupling constant becomes larger and therefore contributions of higher order terms are more significant. For example, at the energy scale of m_Z the running coupling constant is $\alpha(m_Z^2) \approx 1/128$. [7] Higher order contributions are expected to be essential to the precision tests of the Glashow-Weinberg-Salam theory at the soon to be operating Z^0 factories, the e^+e^- colliders operating near the mass of the Z^0, SLC and LEP. [7] In particular, hard photon effects are expected to play a crucial role in the measurement of the μ-pair cross section and the charge asymmetry, two of the most important tests of the theory at m_Z.

1.1.1 Cross section

Photon bremsstrahlung in the initial state affects the μ-pair production kinematics, causing the final muon momenta to be acollinear. A muon pair can only be defined by a collinearity requirement. This is a consequence of the well known infrared divergence which says that the probability of emitting any finite number of photons in any scattering of charged particles is zero– ie., the probability of detecting two exactly collinear muons is zero. This is the familiar Bloch-Nordsieck limit. We will encounter the same problem in attempting to measure the $\mu\mu\gamma$ cross section, where the additional photons will result in an aplanarity distribution of the events. Fig. 1.1 shows the effect of hard photon bremsstrahlung on the μ-pair cross section at 29 GeV and near the Z^0 resonance. The effect of initial state radiation

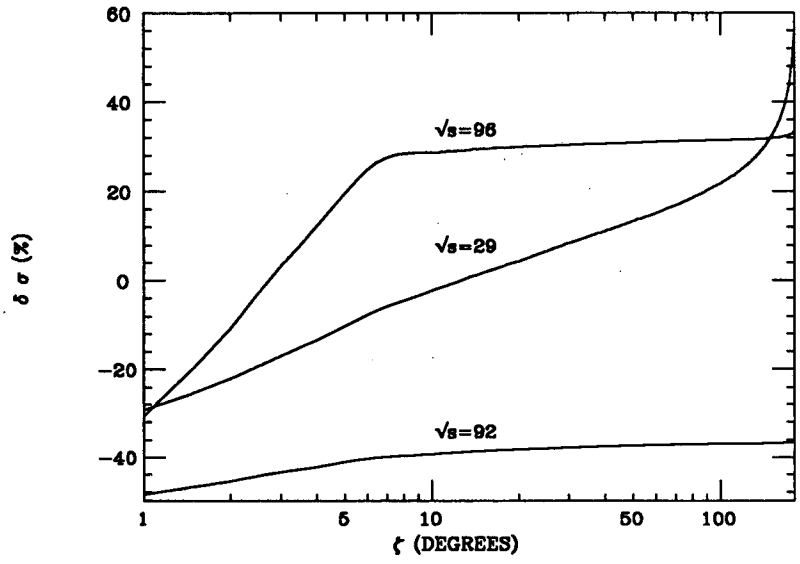

Figure 1.1. Sensitivity ($\delta\sigma$) of μ-pair cross section to hard photon radiation at 29 GeV and near $\sqrt{s} = m_Z$ ($\delta\sigma = (\sigma(\varsigma) - \sigma_0)/\sigma_0$, where σ_0 is the lowest order cross section).

is most dramatic just above resonance where the energy loss due to the radiation pushes the amplitude back on resonance.

1.1.2 Asymmetry

Hard photon effects are also expected to strongly affect the μ-pair charge asymmetry at the Z^0 resonance. The electroweak forward-backward asymmetry is defined by,

$$A = \frac{\sigma_\mu(f) - \sigma_\mu(b)}{\sigma_\mu(f) + \sigma_\mu(b)}$$

where σ_μ is the cross section for μ^+ scattering in the forward (backward) direction with respect to the initial e^+ beam direction. This is not a parity violating effect as it only depends on the axial vector coupling of the Z^0. It results from the interference of the axial vector component of the Z^0 which creates a $C = +1$ μ-pair final state with the s channel photon amplitude which necessarily creates a $C = -1$ final state due to the negative C parity of the photon and the charge parity

invariance of the electromagnetic interaction. In fact, as was first pointed out by Putzolu, [8] in general the interference of amplitudes of opposite charge parity leads to charge asymmetries. The radiative corrections to the electroweak asymmetry include the interference of diagrams of differing C-parities as can be seen in Fig. 1.2 by counting the number of photons in the intermediate state. Fig. 1.3 shows how the μ-pair asymmetry is changed by radiative corrections at 29 GeV and near m_Z.

In the process $ee \rightarrow \mu\mu\gamma$ a pure QED asymmetry arises from the interference of initial and final state amplitudes S_I and S_F. The initial (final) state amplitude gives rise to a $C = -1$ (C=+1) $\mu\mu$ final state. The asymmetry is defined in an analogous fashion to the μ-pair case,

$$A = \frac{d\sigma(\mu^+\mu^-\gamma) - d\sigma(\mu^-\mu^+\gamma)}{d\sigma(\mu^+\mu^-\gamma) + d\sigma(\mu^-\mu^+\gamma)}, \tag{1.1}$$

where the notation indicates the exchange of $\mu+$,$\mu-$ momenta. (A more precise experimental definition will be given later.) As shown in Appendix A, this quanitity is proportional to the interference of initial and final state radiation amplitudes, $A \propto 2\Re\{S_I S_F^*\}$. Clearly, the magnitude of the interference depends on the size of the amplitudes S_I and S_F. To get a feeling for these amplitudes we can look at the integrated photon spectrum in pure QED which is a charge symmetric quantity and therefore contains no interference (neglecting weak effects): [9]

$$\frac{d\sigma}{dk} = (\frac{d\sigma}{dk})_{initial} + (\frac{d\sigma}{dk})_{final} \tag{1.2}$$

$$(\frac{d\sigma}{dk})_{initial} = \frac{\alpha}{\pi}\frac{1}{k}[\log(\frac{s}{m_e^2}) - 1][1 + (\frac{s'}{s})^2]\sigma_0(s')$$

$$(\frac{d\sigma}{dk})_{final} = \frac{\alpha}{\pi}\frac{1}{k}[\log(\frac{s}{m_\mu^2}) - 1 + \log\frac{s'}{s}][1 + (\frac{s'}{s})^2]\sigma_0(s)$$

$$\sigma_0(s) = \frac{4\pi\alpha^2}{3s}$$

These formulas are plotted in Fig. 1.4 We note that the final state amplitude falls off with increasing k as it does not benefit from a reduced center of mass.

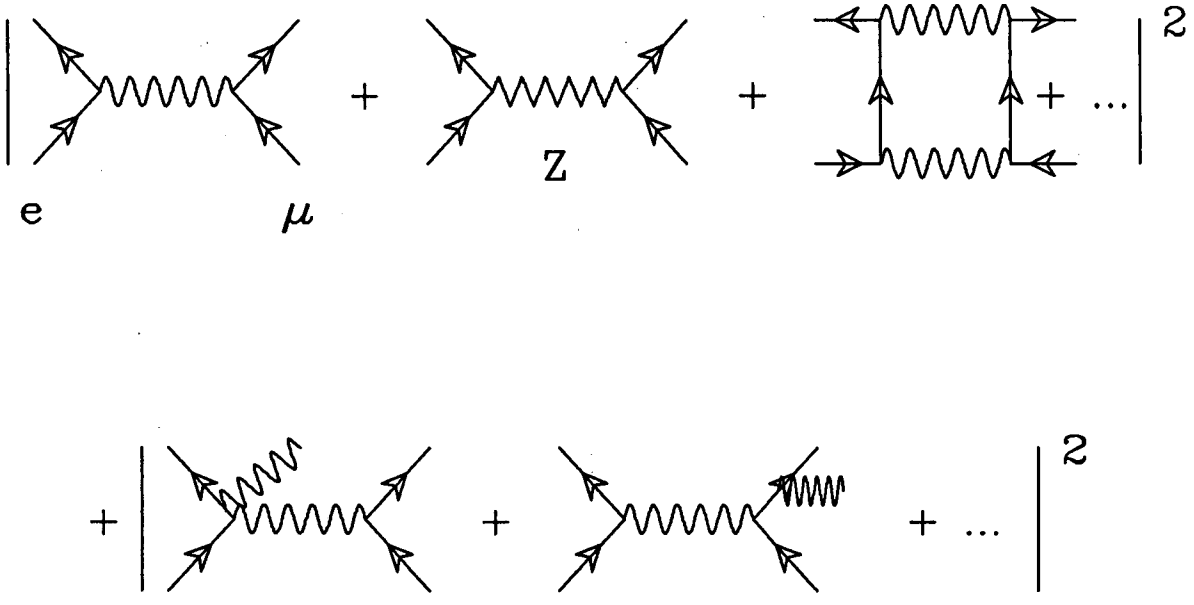

Figure 1.2. Higher order corrections to the process $ee \rightarrow \mu\mu$. The interference of amplitudes of different charge parity produces a forward-backward charge asymmetry in the $\mu^+\mu^-$ final state. The interference of the first two diagrams produces such an asymmetry due to the axial vector coupling of the Z. For the remaining diagrams, the charge parity of the amplitude follows from the number of photons (C=−1) in the intermediate state. Thus, the "box" diagram, which has a two photon intermediate state, will also produce an asymmetry upon interference with the one photon annihilation amplitude. Similarly, the interference of the two bottom diagrams also contributes to the asymmetry.

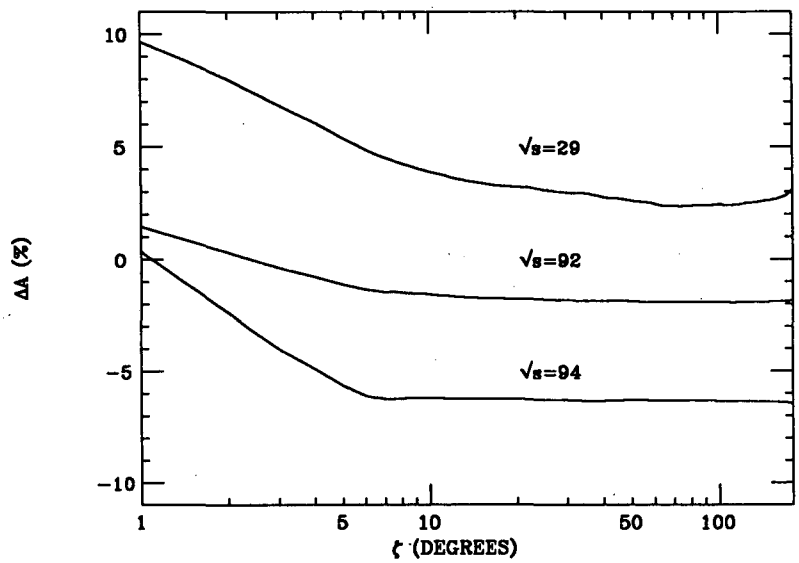

Figure 1.3. Effect of radiative corrections on μ-pair charge asymmetry at 29 GeV and near $\sqrt{s} = m_Z$ ($\Delta A = A(\varsigma) - A_0$, where A_0 is the asymmetry to lowest order).

1.1.3 Excited muons

In order to quantify the momentum transfer (or distance scale) to which QED has been tested, it is natural to introduce modifications of the theory parameterized by some mass scale Λ representing the energy scale of hypothetical QED breakdown. Initially the modification of the photon propagator was motivated by the photon cut-off introduced as a renormalization technique,

$$\frac{-ig_{\mu\nu}}{q^2} \rightarrow -ig_{\mu\nu}\left(\frac{1}{q^2} \pm \frac{1}{q^2 - \Lambda^2}\right)$$

or, in position space corresponding to a modification of the potential by,

$$\frac{1}{r} \rightarrow \frac{1}{r} \pm \frac{1}{r}e^{-\Lambda r}.$$

Low suggested that a natural theoretical framework for parameterizing QED breakdown would be to introduce new hypothetical heavy bosons and leptons. [10] For

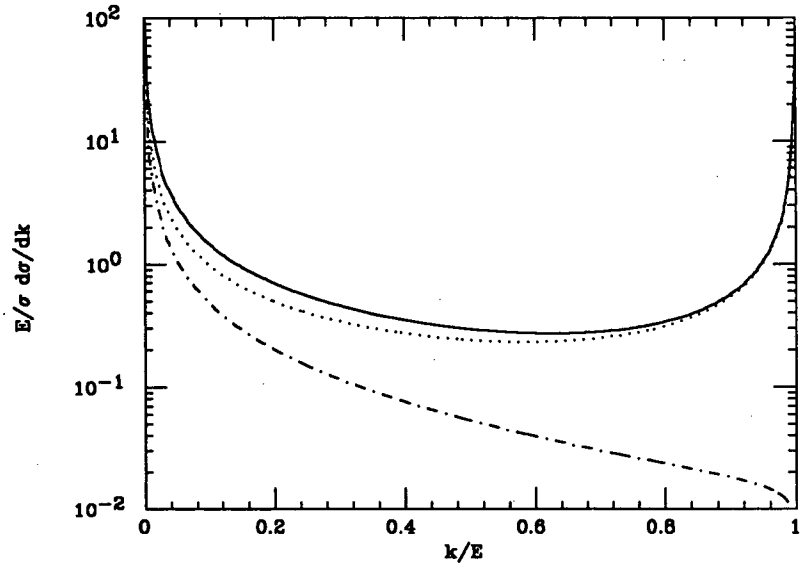

Figure 1.4. Photon energy spectrum at $\sqrt{s} = 29$ GeV (solid curve) showing contributions from initial state radiation (dotted curve), final state radiation (dot-dashed curve)

example, the above modification with the choice of the plus sign can be thought of as the exchange of a heavy vector boson coupling in the same way to the electromagnetic current as the photon. In fact, the minus sign can result from a vector boson coupling with an imaginary coupling. [11] [12] Another breakdown mechanism introduced by Low was the non-minimal coupling of an excited lepton (for example, a μ^*)

$$\mathcal{L}_{int} = \frac{eG}{2M^*}\bar{\psi}_{\mu^*}\sigma_{\mu\nu}\psi_\mu F^{\mu\nu} + h.c. \tag{1.3}$$

where $F^{\mu\nu} = \partial^\mu A^\nu - \partial^\nu A^\mu$ is the electromagnetic field strength tensor. This interaction is gauge invariant and parity conserving– the minimal coupling would not be gauge invariant. It is however only an effective, non-renormalizable interaction since it necessarily contains a dimensionfull coupling constant which we have

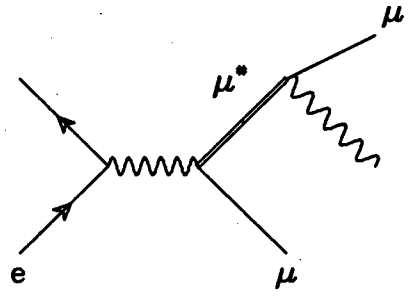

Figure 1.5. The amplitude contributing to $ee \rightarrow \mu\mu\gamma$ due to the existence of an excited muon coupling of the lagrangian 1.3. The μ^* will be virtual or real depending upon whether the center of mass energy is below or above the threshold for production of the $\mu^*\mu$ final state.

written explictly. Such a coupling would result in an extra amplitude contributing to the $\mu\mu\gamma$ final state. (see Fig. 1.5)

The existence of excited leptons is intriguing from the viewpoint of compositeness– the leptons (and quarks) may not be fundemental, point-like particles but may in fact reveal some structure at short enough distances. This conjecture is motivated by the generation puzzle: the existence of three generations of quarks and leptons, identical except for their masses and weak interactions. The three generations, grouped in their $SU(2)_L$ weak isospin doublets are,

$$\begin{pmatrix} \nu_e \\ e \end{pmatrix} \quad \begin{pmatrix} \nu_\mu \\ \mu \end{pmatrix} \quad \begin{pmatrix} \nu_\tau \\ \tau \end{pmatrix}$$

$$\begin{pmatrix} u \\ d' \end{pmatrix} \quad \begin{pmatrix} s \\ c' \end{pmatrix} \quad \begin{pmatrix} t \\ b' \end{pmatrix}$$

where the primes indicate that the weak isospin eigenstates are linear combinations of the mass eigenstates. The sixth quark, denoted t, has not yet been observed but is generally presumed to exist in order to complete the third generation. This pattern of generations might be explained by postulating constituents for the quarks and leptons, just as the periodic table is explained by the atomic constituents electron,proton and neutron and as the hadronic mass spectrum is explained by the quark hypothesis. Many composite models have been proposed. [13] If such substructure were to exist, it is natural that excited states of quarks and leptons should exist. Their coupling to ordinary leptons might be by the effective coupling Eqn. 1.3 . A stringent constraint for e^*, μ^* couplings of this type results from the measurement of the anamolous magnetic moments of the electron and muon. These measurements are some of the most precise tests of the standard model. The anamolous magnetic moments arise from vertex corrections, and the effect of e^*, μ^* can be calculated. [14] [15] (See Fig. 1.6) The present agreement between theory and experiment for $a = (g-2)/2$ is striking: [16]

$$\delta a = |a_\mu^{th} - a_\mu^{exp}| < 8.5 \times 10^{-9}$$

Brodsky and Drell [15]argue that the contributions to the anamolous magnetic moment of the muon due to Eqn. 1.3 must be linear in the mass ratio, $\delta a \sim m_\mu/M^*$ and thus obtain a lower bound on the μ^* mass of $M^* > 10^6$ GeV.

This limit can be avoided by the imposition of chiral symmetry. [15] [17] In this case the contribution to the magnetic moment is $|\delta a| \sim (m_\mu/M^*)^2$. The lagrangian is then, [18]

$$\mathcal{L}_{int} = \frac{eG}{2M^*}\bar{\psi}_{\mu^*}\sigma_{\mu\nu}(1+\gamma_5)\psi_\mu F^{\mu\nu} + h.c. \tag{1.4}$$

In an explicit calculation Renard has shown that the limit from the muon magnetic moment is then reduced to [18] [19]

$$\left(\frac{G}{M^*}\right)^2 = \frac{\pi}{9\alpha}\frac{\delta a}{m_\mu^2} < \left(\frac{1}{160\ \text{GeV}}\right)^2 \tag{1.5}$$

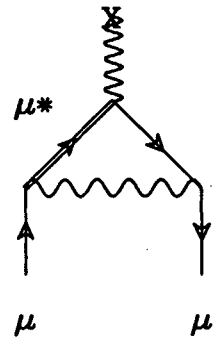

Figure 1.6. Contribution to the anamolous magnetic moment of the muon due to an excited muon coupling.

where the arbitrary coupling G is now included in the limit. We will be able to obtain a better limit from $ee \rightarrow \mu\mu\gamma$. Recently, what at first appeared to be anamolous $Z \rightarrow ee\gamma, \mu\mu\gamma$ events have revived interest in a light μ^*. [20] The couplings to the photon and to the Z are however entirely independent, so that $\mu\mu\gamma$ at $\sqrt{s} =$ 29 GeV cannot constrain the μ^* coupling to the Z. [21]

1.2 THE HADRONS+ γ PROCESS

Interest in hard photon hadronic events stems from the possibility of final state radiation of direct photons. Direct photons are by definition not the decay products of radiatively decaying hadrons. As already noted, this can yield important information about the elementary production mechanism.

By now the evidence for the existence of quarks is compelling. The wealth of meson and baryon spectroscopic data and the baryon magnetic moments fit neatly into the quark model. Perhaps the most dramatic evidence for quarks comes from

the existence of jets in e^+e^- annihilation with the angular distribution expected from spin 1/2 particles. [22]

In the quark model the total cross section for e^+e^- annihilation to hadrons is simply related to the lowest order (point) cross section for μ-pair production,

$$R = \frac{\sigma_{had}}{\sigma^0_{\mu\mu}} = 3\sum_i Q_i^2,$$

where the charges Q_i are in units of the electric charge, the point μ-pair cross section is $\sigma^0_{\mu\mu} = 4\pi\alpha^2/3s$, and the sum is over all flavors (u,d,s,c,b). The factor of three is due to color. This number has been measured and found to be in excellent agreement with the predicted value, taking into account radiative corrections and higher order QCD effects. [23]

The R measurement does not, however, uniquely determine the quark charge. The standard quark charge assignment (Gell-Mann–Zweig) assumes that color symmetry is absolute, unbroken by electromagnetism, and assigns fractional charges to the quarks. However, any charge assignment for the colors r,y,b of $Q_r, Q_y, Q_b, Q_r - 1, Q_y - 1, Q_b - 1$ for the up and down weak isospin components is possible provided $Q_r + Q_y + Q_b = 2$. [24] In particular, the Han-Nambu model assigns integer charges with the choice $Q_r = 0, Q_y = Q_b = 1$. The fractional and integer charge assignments are listed in Table 1.1.

Table 1.1. Fractional (Gell-Mann–Zweig) and Integer (Han-Nambu) charge assignments for the colors r,y,b for flavors u and d. Similar assignments are made for the c,s and t,b generations.

	Fractional					Integer				
	r	y	b	$\langle\lvert Q\rvert\rangle$	$\langle Q^2\rangle$	r	y	b	$\langle\lvert Q\rvert\rangle$	$\langle Q^2\rangle$
u	2/3	2/3	2/3	2/3	4/9	0	1	1	2/3	2/3
d	−1/3	−1/3	−1/3	1/3	1/9	-1	0	0	1/3	1/3

To see why R does not distinguish between these two models, we first note that for fractional charge assignments the electromagnetic current is a color singlet,

$$J_F^1 = \sum_{c=r,y,b} \left\{ \frac{2}{3}\bar{u}_c u_c - \frac{1}{3}\bar{d}_c d_c - \frac{1}{3}\bar{s}_c s_c + \frac{2}{3}\bar{c}_c c_c - \frac{1}{3}\bar{b}_c b_c \right\}$$

The current with the integer charge assignments can be trivially rewritten as a color singlet and a color octet piece:

$$\begin{aligned} J_I &= \bar{u}_y u_y + \bar{u}_b u_b - \bar{d}_r d_r - \bar{s}_r s_r - \bar{b}_r b_r + \bar{c}_y c_y + \bar{c}_b c_b \\ &= \sum_{c=r,y,b} \left\{ \frac{2}{3}\bar{u}_c u_c - \frac{1}{3}\bar{d}_c d_c - \frac{1}{3}\bar{s}_c s_c + \frac{2}{3}\bar{c}_c c_c - \frac{1}{3}\bar{b}_c b_c \right\} \\ &\quad - \sum_{q=u,d,s,c,b} \left\{ \frac{2}{3}\bar{q}_r q_r - \frac{1}{3}\bar{q}_y q_y - \frac{1}{3}\bar{q}_b q_b \right\} \\ &= J_I^1 - J_I^8 \end{aligned}$$

Since the hadronic final state is, as a result of confinement, a color singlet only J_I^1 contributes to R and therefore gives the same prediction as the fractional charge assignment and is consistent with experiment. A different prediction for R would only result if color were to become "unfrozen" at some threshold allowing the production of color non-singlet hadronic states. In this sense R only measures the color average of the quark charges, $\langle |Q_i| \rangle^2$.

Brodsky, Carlson and Suaya [2] have argued that final state radiation of direct photons can in principle distinguish between fractional and integer charged quark models. For photons detected at large momentum perpendicular to the jet axis the photon couples directly to the quark as illustrated in Fig. 1.7 In this case the intermediate quark, anti-quark state need not be a color singlet because quarks are asymptotically free in QCD. In particular they suggest that the charge asymmetry

in hard photon events is a sensitive measure of the quark charge. They predict that the ratio of this asymmetry to that observed in $\mu\mu\gamma$,

$$R^3 = \frac{d\sigma(q^+q^-\gamma) - d\sigma(q^-q^+\gamma)}{d\sigma(\mu^+\mu^-\gamma) - d\sigma(\mu^-\mu^+\gamma)} = 3\sum_i \langle |Q_i| \rangle \langle Q_i^2 \rangle, \tag{1.6}$$

where the definition is analogous to Eqn. 1.1 . Here the notation indicates the exchange of q^+, q^- momenta. From Table 1.1 we find that R^3 will have the values $\frac{19}{9}$ and $\frac{11}{3}$ for fractional and integer assignments respectively. Another quantity that is sensitive to $\langle Q_i^2 \rangle$ is the total cross section for $e^+e^- \rightarrow$ hadrons$+\gamma$. It can be shown that this cross section is a measure of $\langle Q_i^2 \rangle^2$. (In the same way the total cross section for inclusive hadron production in two photon annihilation is also a measure of $\langle Q_i^2 \rangle^2$ [3] .) An additonal quantity sensitive to $\langle Q_i^2 \rangle$ has also been recognized. [25] This is the azimuthal dependence of the photon momentum with respect to the positve quark momentum. This quantity is, however, less quantitative. Finally, we note that recent arguments have been proposed suggesting that these experiments do not in fact distinguish between fractional and integer charged quark models below color threshold when effects of charged gluons in integer charged quark models are properly taken into account. [26] Despite these suggestions these quantities remain interesting, although the experimental hurdles are, as we shall see, quite formidable.

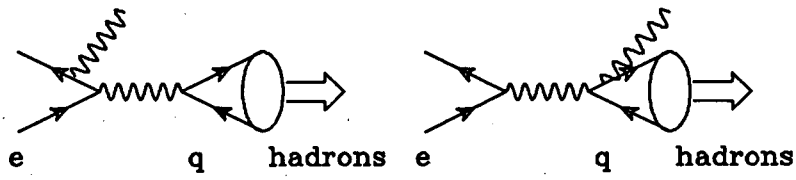

Figure 1.7. Feynman diagrams for $ee \rightarrow$ hadrons $+ \gamma$ for photons detected at large perpendicular momentum to the quark momenta.

2. The Mark II Detector

The data described in this thesis was collected over a four year period with the Mark II detector at the PEP (Positron Electron Project) e^+e^- storage ring at SLAC (Stanford Linear Accelerator Center). The two mile long linear accelerator/injector injects electrons and positrons at 14.5 GeV as counter rotating beams into the 2.2 km in circumference PEP ring. Each beam consists of three bunches rotating at a frequency of 136 kHz and colliding every 2.4 μsec at each of 6 interaction regions. Typical currents are about 15 mA for the sum of the three bunches in a beam. Typical peak luminosities were 3×10^{31} cm^{-2}/sec, with an average luminosity of about 1 pb^{-1}/day. A total of about 227 pb^{-1} was collected by the Mark II.

The Mark II was a multipurpose magnetic spectrometer designed to study a broad class of events resulting from e^+e^- collisions. [27], [28]. Designed with an overall cylindrical symmetry about the beamline (z axis), the detector was made up of eight major systems (see Fig. 2.1) Proceeding radially outward from the beamline, these systems were the Vertex Chamber (VC), Main Drift Chamber (DC), Time of Flight counters (TOF), magnet coil, Lead-liquid Argon Calorimeter (LA), endcap calorimeters, muon system, and Small Angle Tagging system (SAT). The detector at PEP had several configurations. Only the final configuration which included the VC and accounts for the majority (211 pb^{-1}) of the data, will be described here. [29]

2.1 Vertex Chamber

The VC was a high resolution drift chamber designed to measure the secondary verticies from particle decays. [30] It also allowed precise extrapolation of tracks to the beam interaction point. The error on the extrapolation (σ_{ex}) is made up of two components: a multiple coulomb scattering term, and the term due to measurement error.

The multiple coulomb scattering term is proportional to the inner radius of the chamber (r_b), the square root of the thickness of the inner wall in radiation lengths (t) , and inversely proportional to the track momentum. The radius r_b is chosen

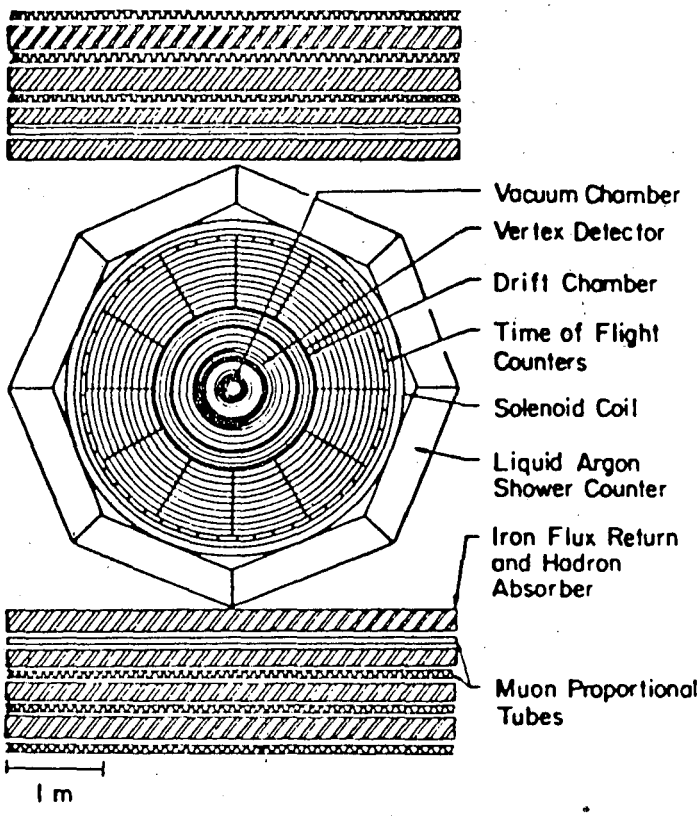

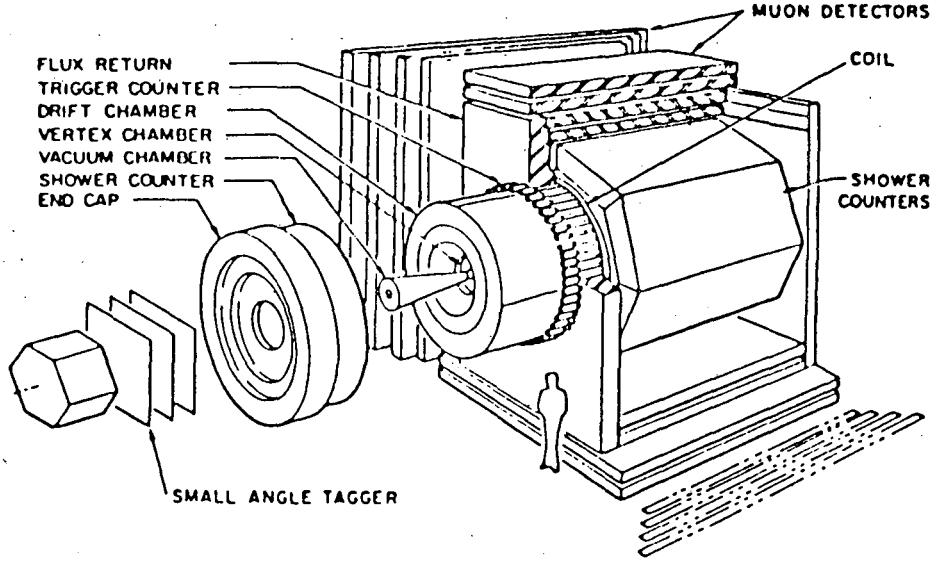

Figure 2.1. Cross sectional and isometric representations of the Mark II detector at PEP.

to be 7.8 cm, the minimum radius necessary to contain the synchrotron radiation from the final focusing quadrupole magnets. To minimize t, the inner wall of the chamber also served as a beam pipe and was made of 1.4 mm of beryllium (z=4 and t=0.006) which was strong enough to withstand the pressure differential of two atmospheres.

The VC wires were arranged in two narrow bands to optimize the extrapolation measurement, an inner band of four layers at a mean radius of about 10 cm, and an outer band of three layers at a mean radius of about 30 cm. The measured spatial resolution of the chamber was 100 μm per layer. The combined rms error on extrapolation to the origin was,

$$\sigma_{ex}^2 = (95/p(\mathrm{GeV}))^2 + (85)^2 \quad \mu\mathrm{m}^2.$$

The tracking at small radii provided by the VC significantly improved the overall momentum resolution of the combined VC and DC tracking system.

2.2 Main Drift Chamber

Central to the tracking of particles was the DC. [31] The chamber consisted of 16 equally spaced concentric layers of drift wires with radii between 41 cm and 145 cm. To provide z information, axial layers were alternated with layers at $\pm 3°$ with respect to the z axis. The gas mixture was 50% argon, 50% ethane. The rms spatial resolution obtained was 220 μm per wire. With a magnetic field of 2.3 kG, the combined VC and DC tracking information determined the track parameters with rms resolutions,

$$(\frac{\delta p_\perp}{p_\perp})^2 = (0.025)^2 + (0.011 p_\perp)^2$$

$$(\delta \tan\lambda)^2 = (3.1/p_\perp \cos^{\frac{3}{2}}\lambda)^2 + (3.9)^2 \quad \mathrm{mr}^2$$

$$(\delta\phi)^2 = (1.0/p_\perp)^2 + (0.4)^2 \quad \mathrm{mr}^2$$

In these formulas the first terms are due to multiple coulomb scattering , the second are the measurement errors, and $p_\perp$ is the momentum in the x,y plane measured in GeV. Tracking was provided over about 80% of the solid angle.

2.3 Time of Flight

The TOF consisted of 48 plastic scintillators surrounding the DC at a mean radius of 1.5 meters. Each 25 mm thick, 20 cm wide, and 3.4 mm long strip was instrumented on both ends by photomultiplier tubes. The rms timing resolution was about 350 ps. For a particle of mass m, momentum p and time of flight T one expects to measure the mass to within $\Delta m = \Delta T(p^2/mT)$. For example, $\pi - k$ separation can be performed up to about 1 GeV. The TOF's primary function at PEP was in triggering.

2.4 Magnet Coil

The 2.3 kG magnetic field was provided by a magnetic coil at a mean radius of 1.6 m. The coil consisted of 2 layers of water cooled aluminum conductor. At normal incidence, the magnet is 1.4 radiation lengths thick. For almost the entire data set only the outer layer was powered due to a short that developed between the inner and outer windings. The field was uniform to within 0.5 % over the tracking volume.

2.5 Liquid Argon System

Detection of electromagnetic energy (photons and electrons) as well as electron/hadron and electron/muon discrimination was provided by a lead/liquid argon calorimeter. The principle of the electromagnetic colorimeter is to use a high Z material to induce an electromagnetic shower, thereby absorbing the incident particle's energy as the ionization produced by a large number of minimum ionizing tracks. A fraction of this ionization is then sampled by an active, charge carrying medium. The choice of liquid argon as the active medium was made for the following reasons. [32] First it is dense ($\rho = 1.4$ g/cm^3) so that a large fraction of

the charge is deposited in a narrow sampling region, thereby reducing measurement error due to sampling fluctuations. Second, argon does not attach free electrons and the electrons can be made to drift readily ($V_{drift} \sim 5$ mm/μsec in a 1 kV/mm electric field) so that an appreciable fraction of the deposited charge is collected in a reasonable amount of time. Finally, argon is inert so that the system is stable.

The calorimeter consists of eight rectangular (3.8 m x 1.8 m x .3 m) modules mounted in a cryogenic vacuum tank and surrounding the magnetic coil at a mean radius of 1.9 meters. [33] The system covers 69% of the polar angle with full azimuthal coverage except for 3° between each pair of modules. Each module consists of a "trigger gap" and a "lead stack". The trigger gap was designed to measure ionization due to showers initiating in the 1.4 X_o of material (mostly the magnetic coil) preceeding the calorimeter and consisted of three aluminum planes 1.6 mm thick and separated by 8 mm liquid argon gaps. The lead stack was constructed out of 37 antimony strengthened lead planes 2 mm thick and separated by 3 mm LA gaps. Alternate layers were at 3.5 kV and segmented to provide spatial information. The azimuthal angle ϕ and polar angle θ were measured by 3.8 cm wide 'F' and 'T' strips running parrallel and perpendicular to the beam. In addition, ambiquity resolution was provided by 5.4 cm 'U' strips running at 45° to the beam. Neglecting the lateral spread of the shower, one expects a position resolution $\sigma \sim$ (strip width)/$\sqrt{12}$. The lateral shower spread is of the order of the Moliere radius in lead (1.8 cm) so that the position resolution achieved for high energy (> 1 GeV) photons and electrons is $\approx$ 20% of a strip width. The strips are ganged together as shown in Fig. 2.2 to reduce signal readout.

The liquid argon calorimeter is a single carrier device due to the low mobility of the positive ions. There is no charge multiplication in the argon, so the observed charge is the integrated current across the argon gap. The electrons drift only half the gap on the average so the observed charge is one-half the number of initial ion pairs. Hence the energy loss per observed charge is twice the ionization energy of argon or 2×26.4 eV $= 52.8$ eV. This gives a signal of .6 pC for 1 GeV of energy deposited in the LA. This signal was detected via low noise, FET input, charge

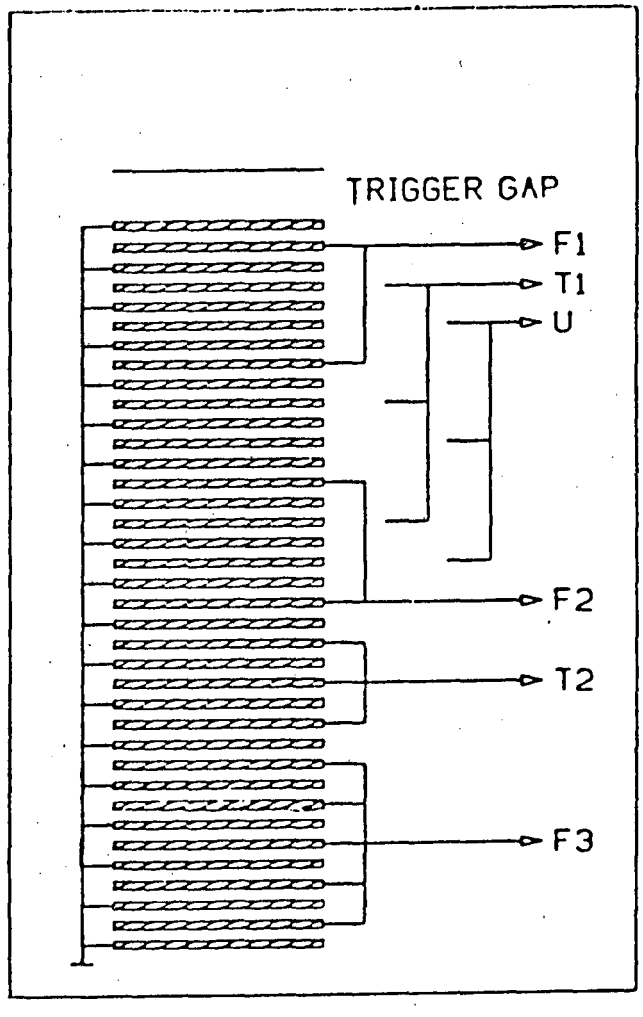

Figure 2.2. The Liquid Argon calorimeter channel ganging scheme.

sensitive preamplifiers located on the exterior of the vacuum cage alongside each of the modules.[33] A transformer was used to minimize the noise due to the impedence mismatch between the FET and the detector, the detector capacitance being large ($\sim$ 5000 pf) compared to the FET. The signal was shaped to form a bipolar pulse whose rise time ($\sim$ 600 ns) is determined by the drift velocity in the argon. In the final stage of amplification a "push-pull" amplifier provides the power gain necessary to drive the output line. The output signal peak voltage was $\sim$ 1 V. The signal was then read out by a sample and hold module and ADC microprocessor. The amplification and signal readout is depicted schematically in Fig. 2.3 . The noise level limits detection to $\approx$ 200 MeV showers.

The charge measured by the calorimeter is deposited by the large number of minimum ionizing tracks that constitute the electromagnetic shower, the number of such tracks being proportional to the energy of the incident particle. Hence the measurement is limited by the poisson statistics of measuring the number of tracks and we expect that the energy resolution $\Delta E \propto \sqrt{E}$. The proportionality constant is determined by sampling fluctuations, leakage, and noise. The sampling fluctuations are dominated by the fraction of ionization sampled. For minimum ionizing particles in liquid argon $(dE/dX)_{la} = 2.2$ MeV/cm and in lead $(dE/dX)_{pb} = 12.8$ MeV/cm so the fraction of charge (energy) sampled was $\Delta E(LA)/\Delta E(LA+PB) \approx 20\%$. The measured energy was then corrected for several factors:

$$E_{corrected} = \alpha E_{la} + \Delta E_{front} + \Delta E_{leak}$$

where,

- α is determined for each module from bhabhas
- ΔE_{front} = correction for energy loss in the 1.4 X_o before the calorimeter calculated using trigger gap information
- ΔE_{leak} = correction for energy leakage, $\approx$ 10% for electrons and photons at the beam energy, the total thickness of the calorimeter being $14X_o$.

The result is an energy resolution of $\Delta E/E = .14\sqrt{E}$.

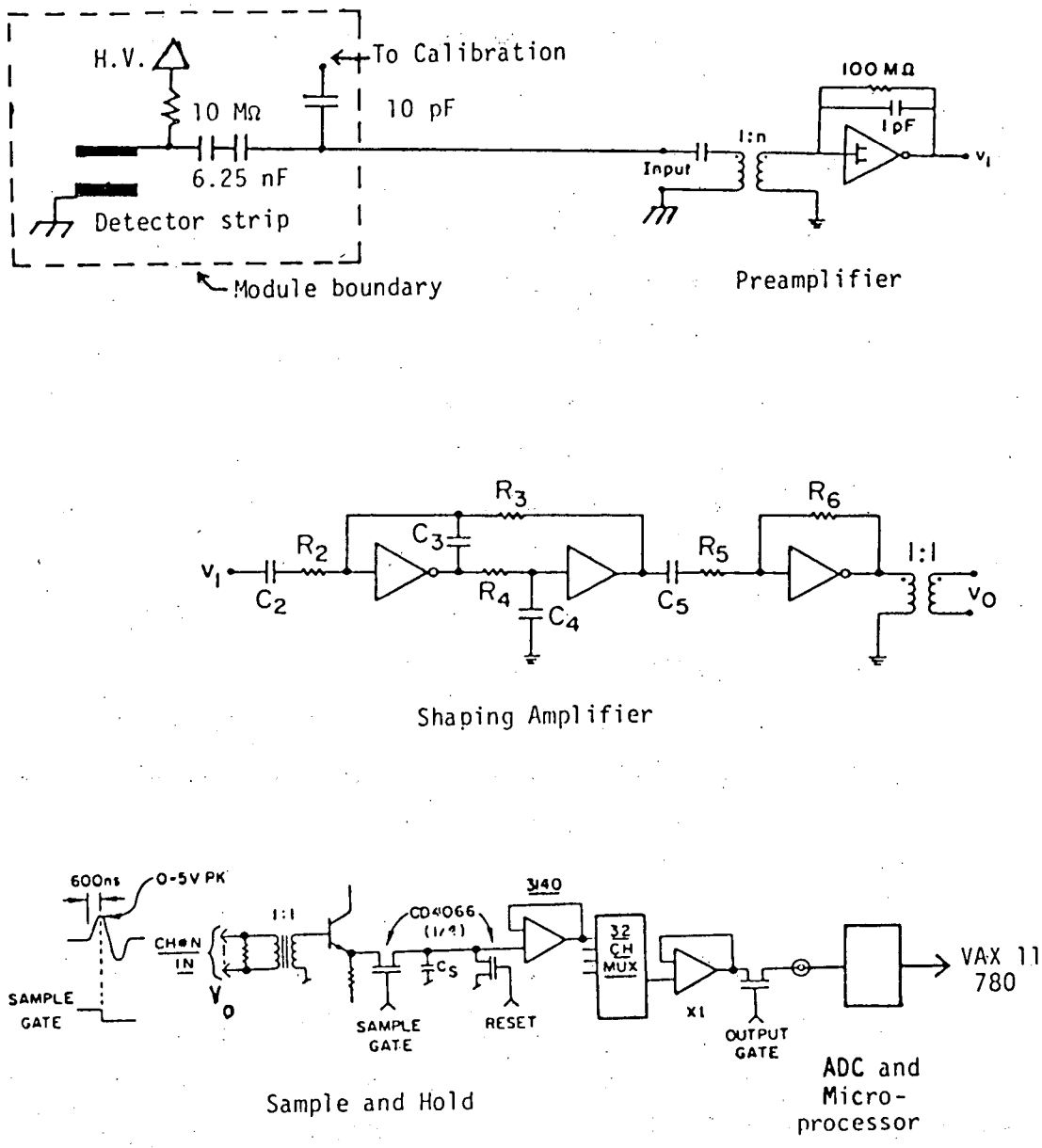

Figure 2.3. Schematic drawing of the liquid argon signal amplification and readout electronics.

2.6 Endcaps

Additional calorimetry was provided by endcaps covering the polar angle in the range $.77 < |\cos\theta| < .96$. Each endcap consisted of two layers of proportional chambers and lead, 4.7 radiation lengths thick. The rms energy resolution obtained was about $\sigma/E = .50/\sqrt{E}$.

2.7 Muon System

The Muon system consisted of four walls above, below, and on either side of the central detector. [34] Each wall consisted of four layers of iron hadron absorber and extruded aluminum proportional tubes with 45 μm sense wires. The tubes in the first layer measure the polar angle, while the remaining three layers measure the azimuthal angle. About 1.4 interaction lengths of material preceeds the muon system, so the total amount of material traversed by a particle at normal incidence at levels one to four is 2.6, 4.0, 5.8, and 7.4 interaction lengths respectively. For a muon dE/dx is only due to ionization losses (the large mass suppresses bremsstrahlung and the muon does not undergo strong interactions) and is a constant independent of path length x determined by the material. At normal incidence, a muon with momentum greater then 2 GeV will penetrate all four layers of absorber. The hadron punch through to the fourth layer is less then 1 %. The muon system covers about 45 % of the solid angle.

2.8 Small Angle Tagging System

Tracking and calorimetry at small polar angles, 21 to 82 mr, was provided by two SAT devicies placed symmetrically at either end of the central detector. Each SAT consisted of (proceeding radially outward from the interaction point) three layers of planar drift chambers, three layers of scintillators which served to define the acceptance, and lead-scintillator shower counters with an energy resolution of $\sigma/E = .15/\sqrt{E}$. The system was designed to identify electrons resulting from low momentum transfer bhabha scattering, as well as the scattered electrons from two

photon processes. The rate of small angle collinear bhabha events was used as an online measure of the luminosity.

2.9 TRIGGERING

Selective data aquisition was controlled by a two-level hardware trigger system. [35] With a beam crossing rate of a little over 400 kHz, the combination of a fast (≈ 1 μsec) , simple primary trigger and a slower (≈ 30 μsec) but clever secondary trigger held the event rate to a few hertz.

The primary trigger is satisfied by either charged, neutral, or Bhabha primary trigger requirements in coincidence with a beam crossing signal derived from a pickup electrode located inside the beam pipe near the interaction point. The charged primary requirement is at least nine DC hits and one TOF hit. The neutral primary requirement is at least two calorimeter modules with 1 GeV or more of energy deposited in the front half of the module, or if the total energy deposited in the front half of all the modules exceeds 4 GeV. The Bhabha primary trigger requirement was derived from the SAT system. The primary trigger rate was typically 100 Hz.

The secondary trigger used hardware trackfinding to determine whether the pattern of drift chamber hits was consistent with a particle track. The track finding microprocessor searched for hardware tracks consisting of combinations of VC and DC hits lying within programed curvature masks which defined "roads" in the x,y plane. The secondary trigger was then satisfied by any of four conditions: 1) at least two hardware tracks, or 2) the neutral primary trigger was satisfied, or 3) the neutral primary requirement was met for a single module and a hardware track was found, or 4) the Bhabha primary trigger is satisfied. To reduce the Bhabha trigger rate, this trigger was scaled by a factor of 16.

3. The $\mu\mu\gamma$ Process

The event selection for $\mu\mu\gamma$ is motivated by two essential experimental considerations. First, the limited solid angle coverage of the muon system which covers only about 45% of the total solid angle. For this reason we will rely on the liquid argon calorimeter which has considerably better solid angle coverage (almost 70%). Second, the desire to maintain a high efficiency to keep Monte Carlo depended efficiency corrections to a minimum. For this reason we use minimal selection criteria motivated by significant known backgrounds.

In testing QED we wish to compare the number of detected $\mu\mu\gamma$ events with the theoretical prediction. For this, knowledge of the luminosity is essential since $N_{events} = \mathcal{L}\sigma$, where $\mathcal{L}$ is the integrated luminosity. The luminosity must be determined by measuring the rate of some well known cross section because the beam parameters in an e^+e^- storage ring are not sufficiently well measured. We therefore begin by understanding the luminosity.

3.1 Normalization

The luminosity was monitored using the small angle tagging system (SAT). The small angle bhabha scattering involves low momentum transfer, $-q^2 \approx .6$ (GeV/c)^2 where QED is well understood. However, because the bhabha cross section is strongly peaked in the forward direction and changes rapidly for small angles, $d\sigma/d\Omega \sim 1/\theta^4$, the SAT luminosity is very sensitive to alignment, edge effects in the shower counters, and beam position. For this reason, the luminosity is best measured from wide angle bhabhas which, although they involve large momentum transfers ($-q^2 > 126$ (GeV/c)^2) are well calculated in QED, and have virtually no background. The cross section for WAB scattering, $\sigma_{ee}^{vis} \approx .75$ nb, is over an order of magnitude larger then the mupair cross section and 5 times the $ee \rightarrow \gamma\gamma$ cross section. Backgrounds are therefore a priori small, and cuts are chosen for maximal efficiency.

To allow for track reconstruction errors and electron interaction in the material, events were selected with 1 to 4 charged tracks reconstructed in the main drift

chamber. We then require two energetic (> 8 GeV) showers in the liquid argon calorimeter. As shown in Fig. 3.1 and Fig. 3.2 the mean energy of these showers can be used to define the liquid argon fiducial volume. The fiducial volume is defined to be $|z| < 1.7$ m and $|\phi| < .33$ rad measured from the center of the module. To minimize the effects of higher order radiative processes, these showers were then required to be collinear to within 20° where the collinearity angle is defined by,

$$\varsigma = \cos^{-1}(\hat{R}_1 \cdot \hat{R}_2)$$

where $\hat{R}$ is the direction of the shower defined with respect to the shower centroid and the beam position as monitored by the beam position monitor on a run-by-run basis. We then require at least one reconstructed track with the requirements,

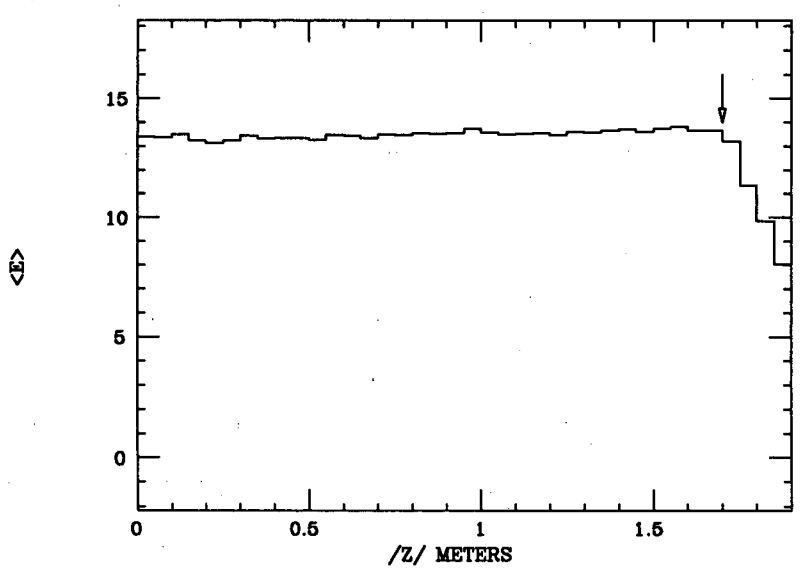

Figure 3.1. Average energy per shower from wide angle bhabhas showing edge of calorimeter in z. The fiducial volume is $|z| < 1.7$ m. Note: no collinearity cut has been applied .

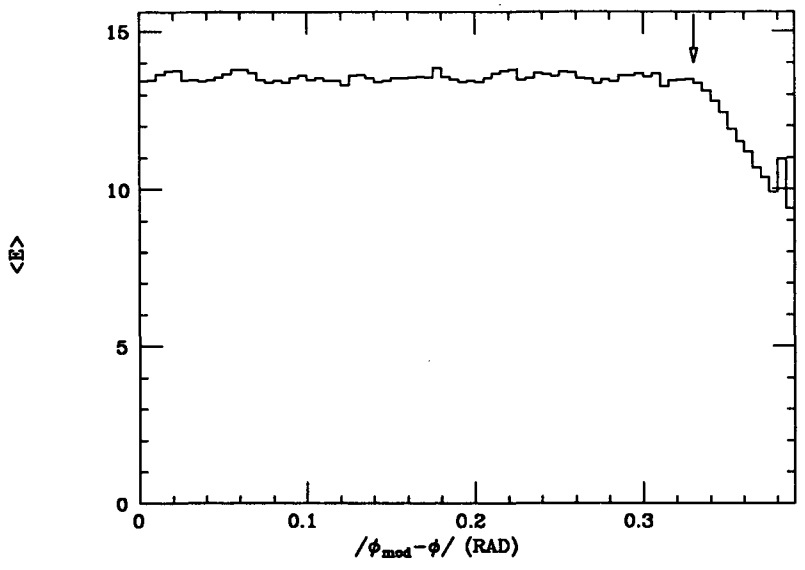

Figure 3.2. Average energy per shower from wide angle bhabhas showing edge of calorimeter in ϕ measured from the module center. The fiducial volume is $|\phi_{mod} - \phi| <$ .33 rad. Note: no collinearity cut has been applied .

1. projected minimum distance to the beam origin less then .05 m in radius and .08 m in z
2. $|\cos\theta| < .65$

Furthermore, at least one track satisfying these requirements must have its momentum within a cone of half angle 40 mr with respect to one of the shower directions. Finally to remove a small background expected from $ee\gamma$ events where only the $e\gamma$ are observed, a check is made to ensure that at least 4 drift chamber hits are found within a cone of half angle equal to 20° about each shower direction. This background is found to be .8%. We find that the inefficiency due to track reconstruction is quite low, .2% of the events have only one track, and that 95.6% of the events have exactly two tracks. The remaining 4.2% of the events have more then two tracks due to external brehemsstralung in the material preceeding the drift chamber.

The background from $\tau\tau$ events in this sample is negligible (.02% as estimated from Monte Carlo study). Other backgrounds are assumed to be negligible. The systematic uncertainty due to these cuts is estimated to be about 1.5%. The collinearity angle distribution is plotted in Fig. 3.3 as a check of the radiative corrections. We note that the data is slightly broader then the $O(\alpha^3)$ Monte Carlo with exponentiation. [36] Exponentiation, which takes into account the emmission of an infinite number of soft photons, will be discussed in the section on the higher order correction and the infrared divergence. Here we note that the exponentiation makes the collinearity distribution less broad because it increases the probability of soft photon (collinear) events and therefore decreases the probability of hard photon emission (acollinear events).

The results of the this luminosity measurement are shown in Table 3.1 We will take the WAB luminosity to be the best measurement of the luminosity and estimate a 5% systematic uncertainty based on the discrepancy between the two measurements. This result is in good agreement with a previous study of the WAB luminosity. [37]

3.2 Event Selection

The event selection begins with the requirement of two charged tracks reconstructed in the main drift chamber. These tracks must both satisfy the requirements,

1. Projected minimum distance to the beam origin less then .05 m in radius and .08 m in z.
2. $p_\perp > 0.1$ GeV
3. $|\cos\theta| < 0.65$
4. The projected drift chamber track at the entrance to the liquid argon system to be within its fiducial volume, and the associated energy of the track less then 2 GeV .

These requirements distinguish the $\mu\mu(\gamma)$ process from the dominant two prong background, the ee(γ) process, because the muon is minimum ionizing in the liquid

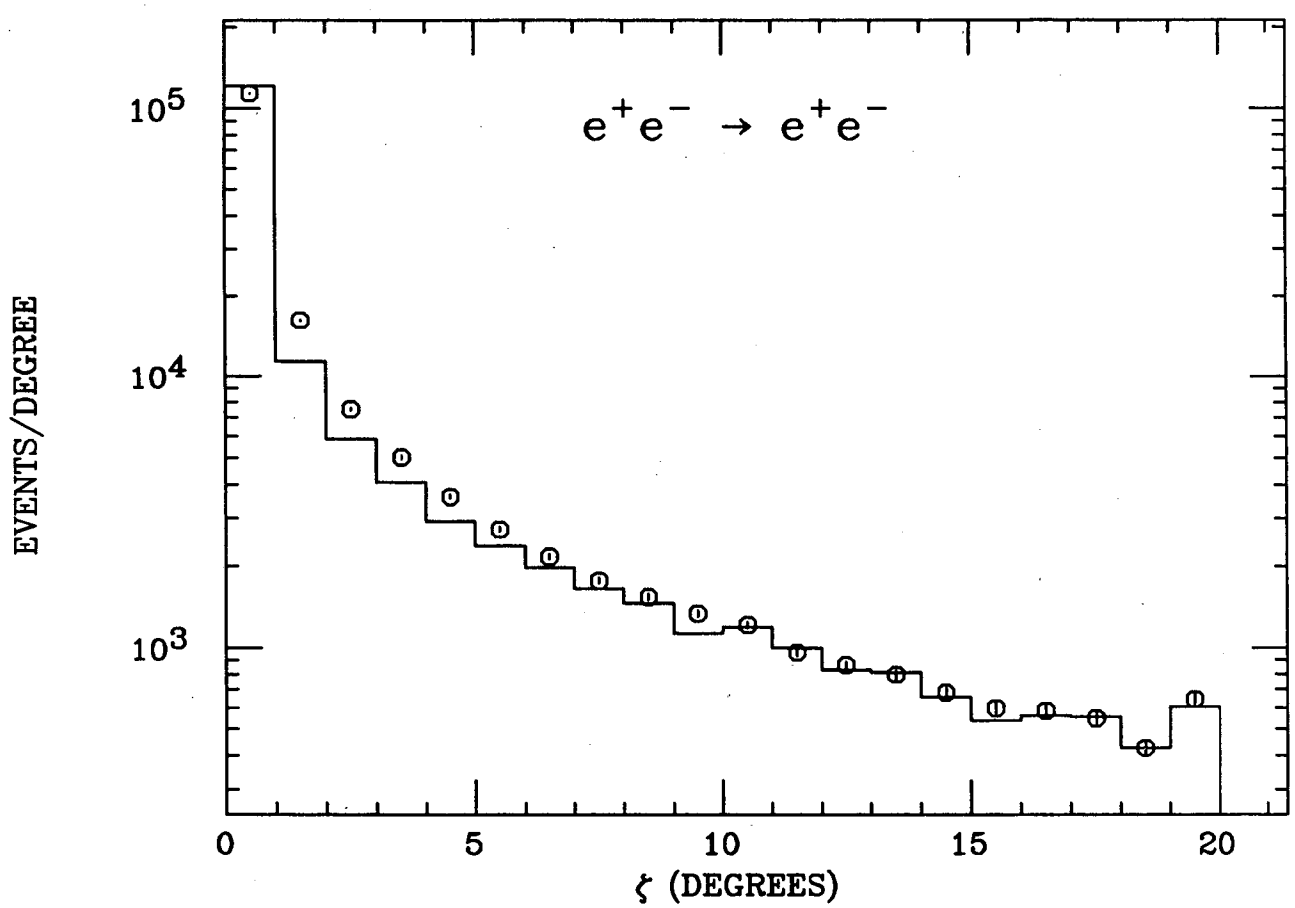

Figure 3.3. Acollinearity distribution of wide angle bhabhas determined from track momenta for events with two reconstructed charged tracks. Solid histogram is $O(\alpha^3)$ Monte Carlo with exponentiation, normalized to the number of events in the data

Table 3.1. Integrated luminosity for various data sets determined from SAT and WAB methods.

data set	runs	events	$\mathcal{L}_{SAT}$	$\mathcal{L}_{WAB}$	$\mathcal{L}_{WAB}/\mathcal{L}_{SAT}$	$\Delta\%$
1	6353-8067	10164	15.11	14.65	.970	-3.0
2	8068-9905	27382	41.86	39.46	.943	-6.0
3	9906-10838	35090	53.87	50.57	.939	-6.5
4	10839-11472	27777	41.55	40.03	.963	-3.8
5	11473-12584	28746	42.92	41.43	.965	-3.5
6	12585-13311	28051	42.15	40.43	.959	-4.3
total	all	15720	237.47	226.57	.954	-4.8

argon. For two prongs collinear to within 10° this separation is shown in Fig. 3.4 Using muons identified by all four layers of the muon system we measure the efficiency of the less then 2 GeV requirement to be 99.2% per track. This is only a .5% per track inefficiency over our detector simulation.

The events were then required to have exactly one neutral track satisfying the requirements,

1. Shower centroid in the liquid argon fiducial volume
2. Separated by more then 30 cm from a charged track
3. $E_{la} > .3$ GeV, where E_{la} is the energy in the liquid argon calorimeter.

Events with showers > 1 GeV in the endcaps were removed. To reduce the background from the two photon process $ee\mu\mu$ and from $\tau\tau(\gamma)$ events the sum of the visible energy, $E_{vis} = p_{\mu+} + p_{\mu-} + E_{la}$ is required to be greater then half the center of mass energy.

With these requirements, a large background remained from $\tau\tau(\gamma)$ were one τ decays to $\mu\nu_\mu\nu_\tau$ and the other decays via the $\tau \rightarrow \pi^{\pm}\pi^0\nu_\tau$ mode. The charged pion will deposite little energy in the liquid argon and the π^0 can fake a photon. This background is large because the process is lowest order in QED and the branching fractions are substantial ($\approx$ .2 and .25 respectively). Fig. 3.5 shows the $\theta_{\mu\gamma}$ angular

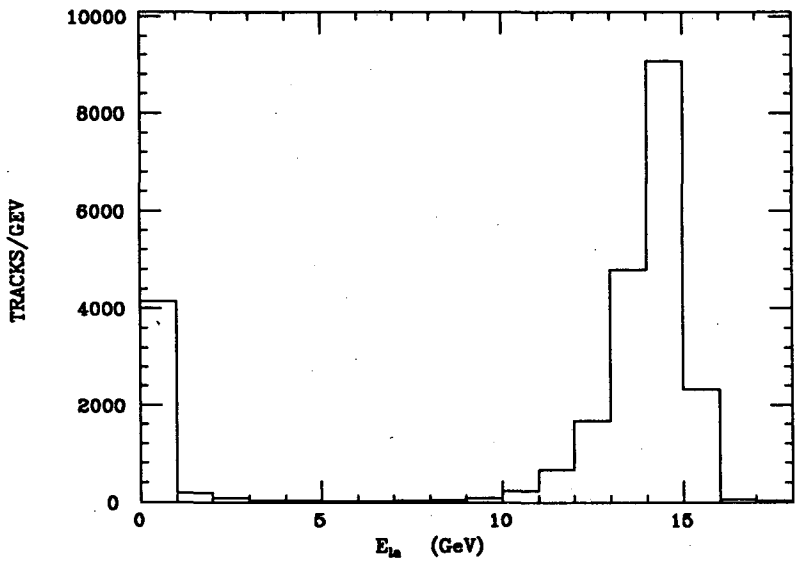

Figure 3.4. e/μ separation for collinear < 10° two prongs by the energy deposited in the liquid argon.

distribution, where $\theta_{\mu\gamma}$ is the angle between the muon and photon momenta, which gives a measure of the expected contamination from these events. We therefore require that the opening angle between the photon and the nearest charged track be greater then 20°. The resulting photon energy spectrum is shown in Fig. 3.6

3.3 ANGULAR RESOLUTION

The process $e^+e^- \rightarrow \mu^+\mu^-\gamma$ is highly kinematically constrained. There are 6 independent kinematic variables of interest: three momenta ($3 \times 3 = 9$) minus two variables that specify the event plane and minus a rotation in that plane which

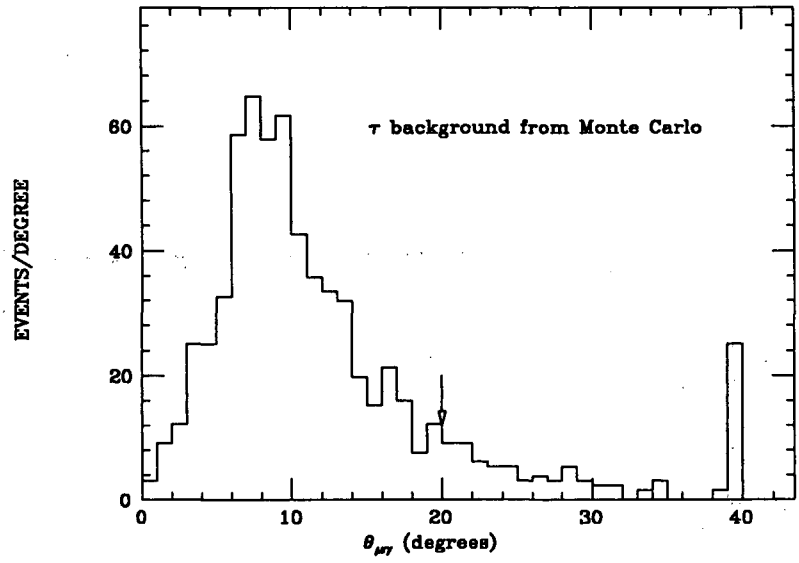

Figure 3.5. Number of events due to $\tau\tau(\gamma)$ expected from Monte Carlo A cut is made at $\theta_{\mu\gamma} > 20°$. The peak at 40° is the overflow bin.

are irrelevant. Energy-momentum conservation then gives four constraints, and therefore only two suitably chosen measured quantities are necessary to specify the kinematics of a particular event. Angle measurements are by far the most precisely measured quantities. We will therefore measure kinematic quantities with angle measurements alone. A suitable choice of variables would thus be any two of the three space angles, where the space angles are defined by $\theta_i = \cos^{-1}(\hat{p}_j \cdot \hat{p}_k)$ $(i, j, k = \mu_1, \mu_2, \gamma)$ where $\hat{p}_i = \vec{p}_i/|\vec{p}_i|$.

The photon angular error is made up of two components: the uncertainty in the beam position and the liquid argon shower resolution. The beam position monitor was used to measure the beam position on a run by run basis. This does not give the best measurement of the interaction point in z due to the size of the beam. A better measurement can be obtained from the distance of closest approach (DCA) to the beam postion for drift chamber tracks. For this analysis, we take the interaction point to be the mean DCA of the charged tracks, $z_{AV} = (z_1 + z_2)/2$.

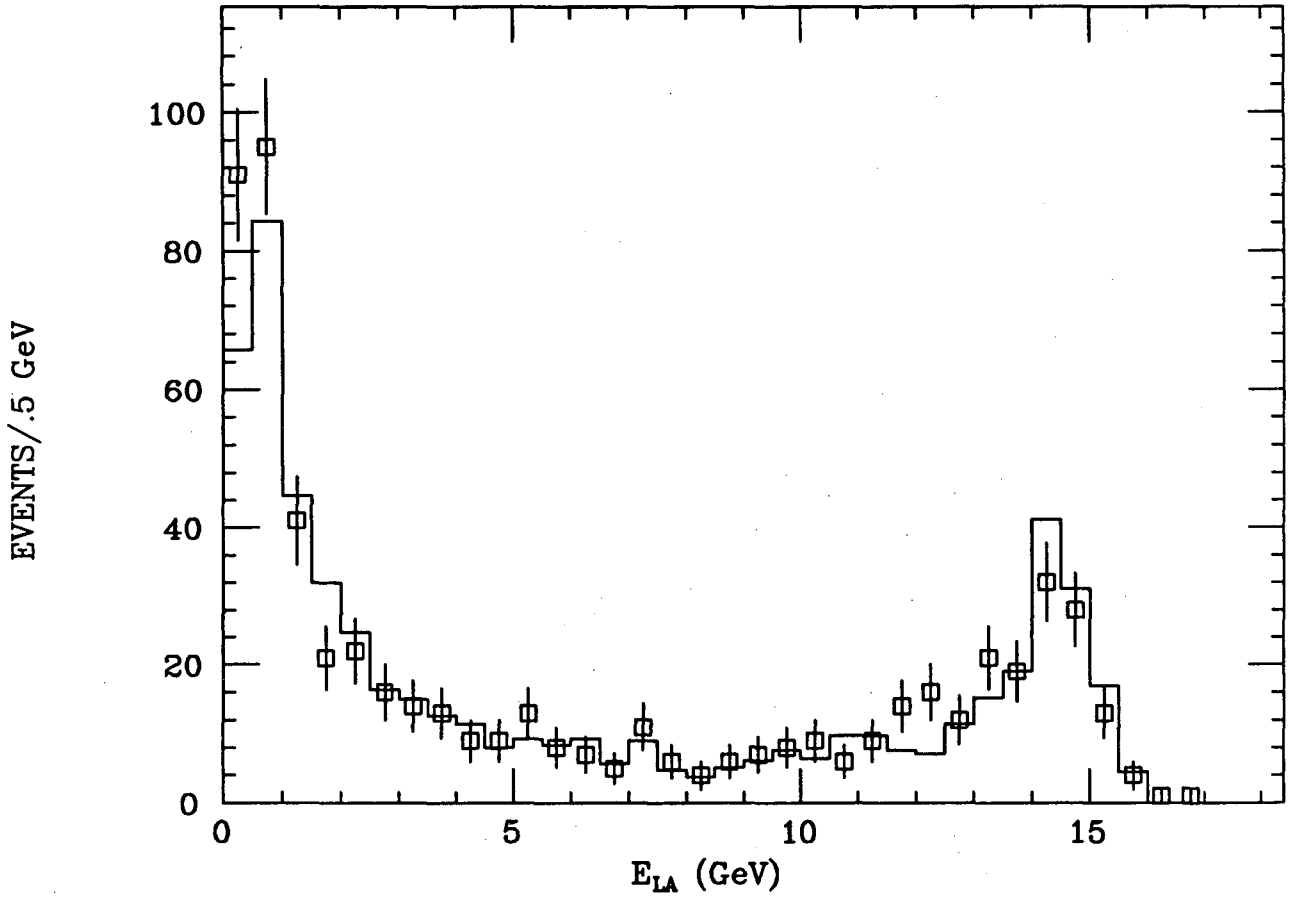

Figure 3.6. Energy of neutral track as measured in the liquid argon calorimeter.

The contribution to the error in z, δz is then 1 cm. This is compared to the beam position monitor measurement z_{IR} in Fig. 3.7.

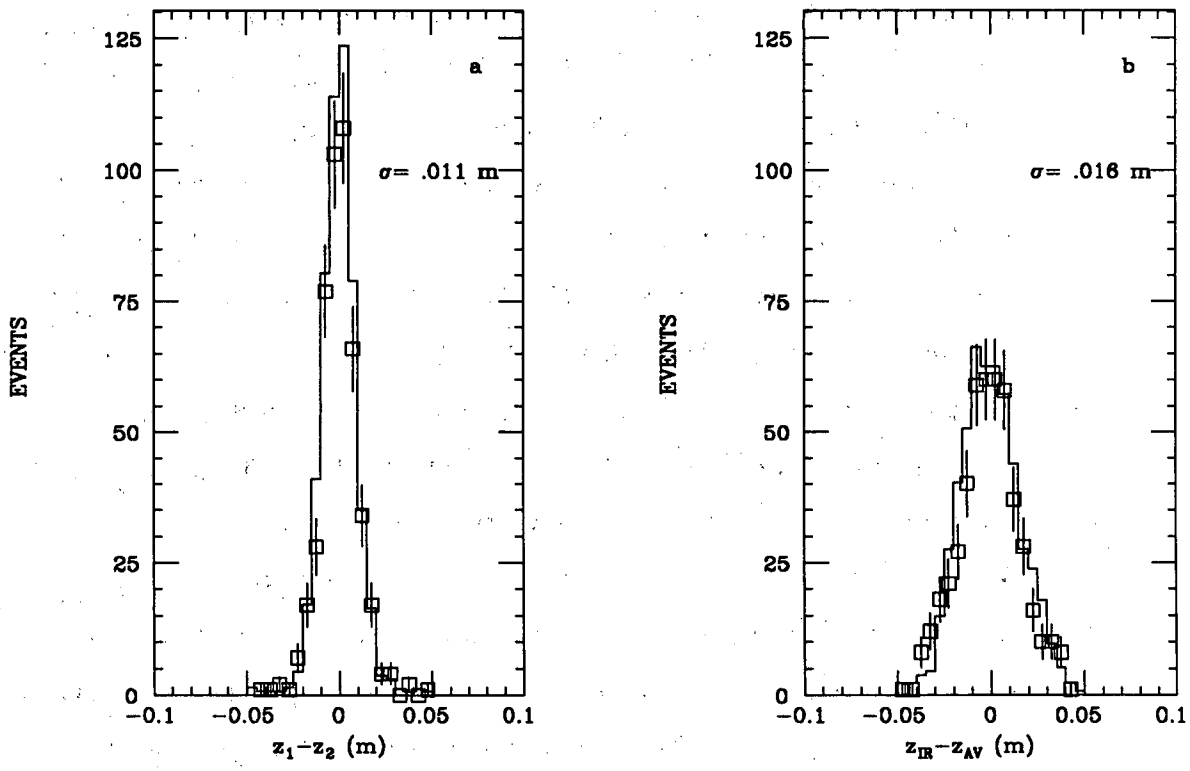

Figure 3.7. a. z difference for the two tracks b. comparison of interaction point as measured by beam position monitor (z_{IR}) and mean z of charged tracks (z_{AV}) Solid histogram is Monte Carlo.

The position resolution of the shower in the liquid argon may be measured directly in the process $ee \rightarrow \gamma\gamma$. For this purpose we look at the aplanarity of the γ momenta, which is defined to be the acollinearity in the x-y plane, or $\eta = \pi - |\phi_1 - \phi_2|$. The acollinearity itself is not used because of the broading due to initial

state radiation. The η distribution is shown in Fig. 3.8 The agreement between the data and the Monte Carlo is at first very poor. This is due to an approximation in the detector simulation. To speed up the detector simulation, an algorithm called OVREZY was used whereby individual showers are not created for each produced particle, but rather are chosen from a shower library. The choice of shower library did not correctly account for shower position. This shortcoming can be redressed by adding a gaussian fluctuation to the shower angle. The angular error measured in the data is $\approx$ 3.5 mr per track corresponding to a position resolution of about .7 cm or 18% of a stripwidth which is what we expect.

The error on the angle measurements of the charged tracks are derived from the chisquared of the track fitting algorithm. As a check that these are well reproduced in the Monte Carlo we can calculate the errors in the space angles, $\delta\theta_\gamma$ and $\delta\theta_\mu$, from the errors on the track fits using error propagation. The result shown in Fig. 3.9 shows that these errors are well reproduced by the detector simulation.

To satisfy the kinematics of $\mu\mu\gamma$ the events must be planar. As a measure of the planarity of the event we use the quantity $\Delta\phi = 2\pi - \Sigma\theta_i$. This quantity is plotted in Fig. 3.10 where the solid histogram shows the effect of detector resolution on $\mu\mu\gamma$ events. Since the known backgrounds are small and the angular error is well understood, we conclude that the deviation from the Monte Carlo calculation is an effect of higher order radiation. Limiting ourselves to only those events lying within our detector resolution would give us a smaller number of events then predicted by $O(\alpha^3)$ QED. As a further check we can look at the momentum conservation in events with large $\Delta\phi(> 20$ mr) along the x,y and z directions. Since initial state radiation is highly peaked along the forward direction, the missing momentum distribution along the z direction in these events should be considerably broader then along the x or y directions. The missing momentum distribution is shown in Fig. 3.11 . The solid histogram is a Monte Carlo calculation of $ee \rightarrow \mu\mu\gamma$ including additional initial state radiation as will be described in the following section.

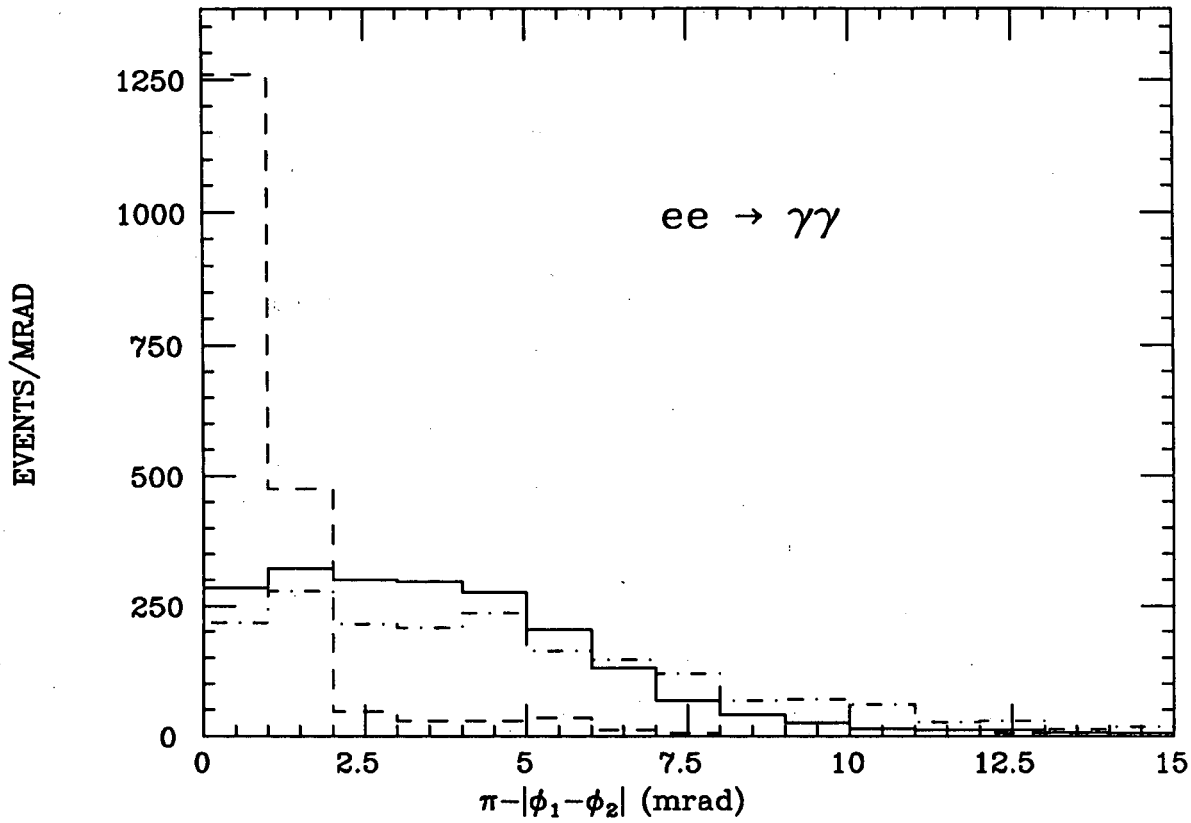

Figure 3.8. Aplanarity in $ee \rightarrow \gamma\gamma$ events. Solid histogram is the data. The dashed histogram is OVREZY, the dot dashed histogram is OVEREZY with added gaussian smearing.

3.4 Higher order correction and infrared divergence

The shape of the planarity distribution is the result of additional photons emitted in the initial state (final state photons would not change the planarity). To calculate this correctly in QED one needs to go the the next higher order in the perturbation expansion, $O(\alpha^4)$. Such a calculation is difficult to perform, and although analytic calculations exist they do not exist conveniently as a Monte Carlo

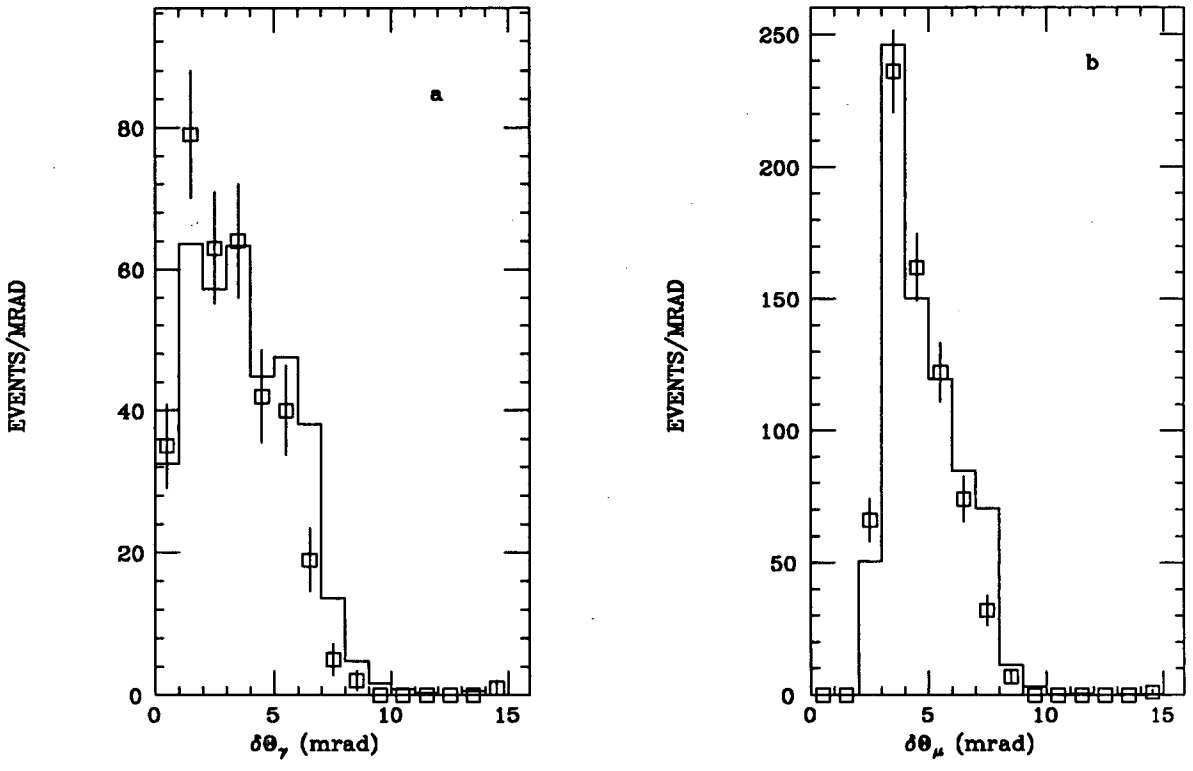

Figure 3.9. Errors on space angles derived from track fitting in the data compared with the detector simulation (solid histogram).

generator such as we desire. [38] Fortunately, a simple approximation will suffice for our purpose.

Soft photon radiation may be treated semi-classically in the Weizsäcker-Williams approximation as the probability for the semi-classical photon emission times the quantum mechanical probability for the process without photon emission. [39] One considers the classical electromagnetic radiation emitted when the e^+e^- are accelerated from their initial velocities to rest during a very short time

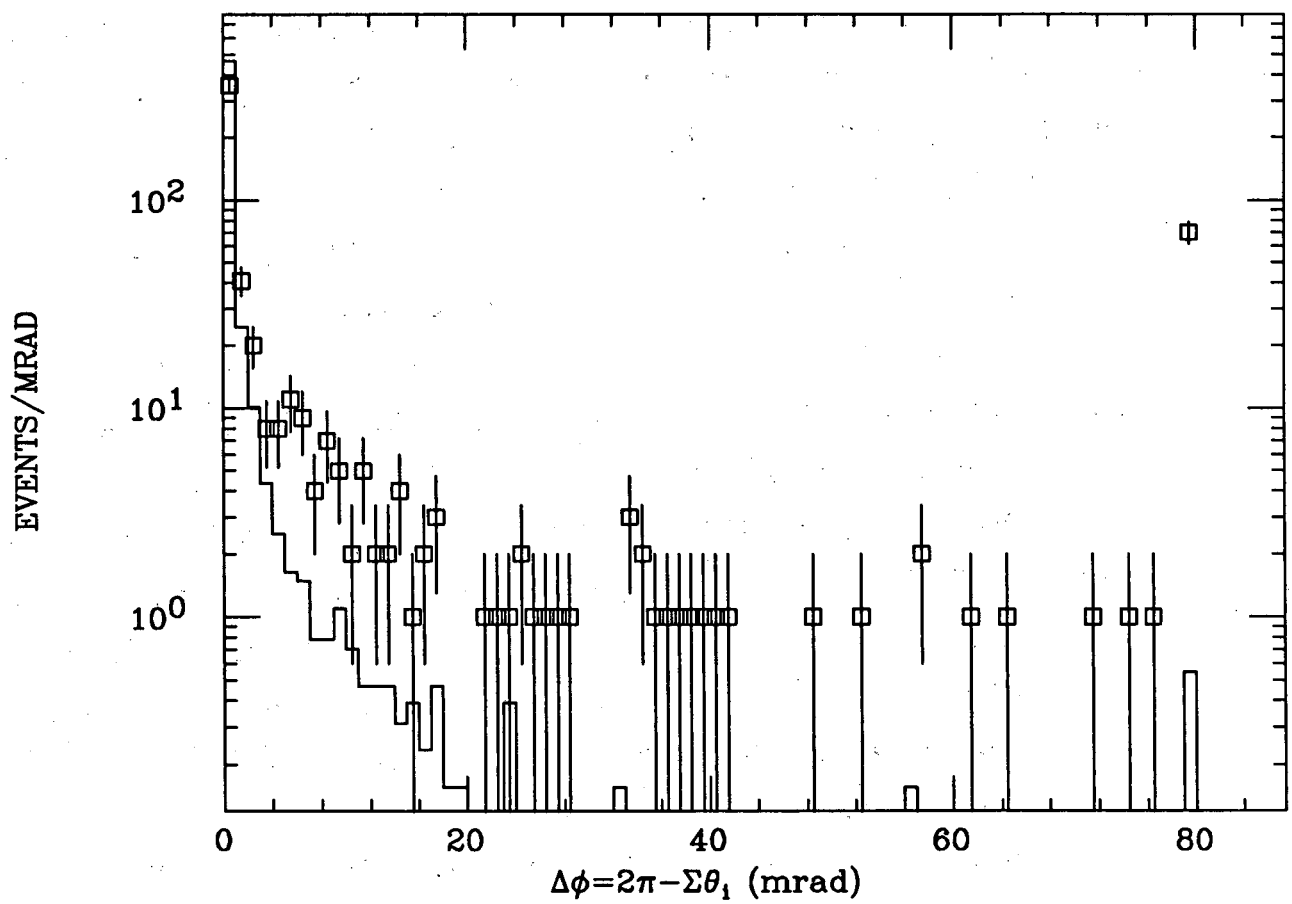

Figure 3.10. Planarity of event as measured by the sum of the space angles. Solid histogram is the Monte Carlo showing detector resolution effects only. The long tail of the distribution has been combined into the overflow bin at the far right.

interval. The intensity spectrum is then converted into the probability for emitting a photon of energy k by dividing by k. When one includes the disappearance of the magnetic moments as well as the charges one obtains the expression, [40]

$$d\sigma'[s] = t_e\Big(\frac{1+(1-x)^2}{2}\Big)\frac{dx}{x}\sigma_o[s(1-x)] \tag{3.1}$$

where $x = k/E_{beam}$ and $t_e = \frac{2\alpha}{\pi}(\log\frac{S}{m_e^2} - 1)$ is the equivalent radiator thickness for the electron. This is the same as the expression for initial state radiation given in equation 1.2 and is the correct quantum mechanical result for the initial state radiation in any e^+e^- annihilation process. [41] [42]

The above formula exhibits the familiar infrared divergence and must be modified. Semi-classically, the infrared divergence arises simply because the classical intensity spectrum is independent of frequency as frequency goes to zero, implying that the number of soft photons emitted diverges. Quantum mechanically, the infrared divergence arises in two contexts. First, just as in the semi-classical treatment, the emission probability for soft photons diverges. Second, the radiative corrections diverge for soft virtual photons. In QED the electron mass and wave function renormalizations cancel, so that only the infrared divergence resulting from the vertex correction (charge renormalization) remains. In QED the problem of the infrared divergence is solved because the divergence from the vertex renormalization and the real soft photon emission cancel.

The cancellation of the infrared divergences in QED arises because the final state energy cannot be defined experimentally with finite precision as was first pointed out by Block and Nordsieck. [43] Another way of stating the result is that the probability of a finite number of photons escaping detection is exactly zero. For example, the probability of detecting no photons in μ-pair production is zero (exactly collinear μ-pair). Thus the μ-pair cross section can only be measured in the context of a collinearity distribution. Similarly, the missing energy due to initial state radiation in $\mu\mu\gamma$ is manifest in an aplanarity distribution, and the $\mu\mu\gamma$ cross

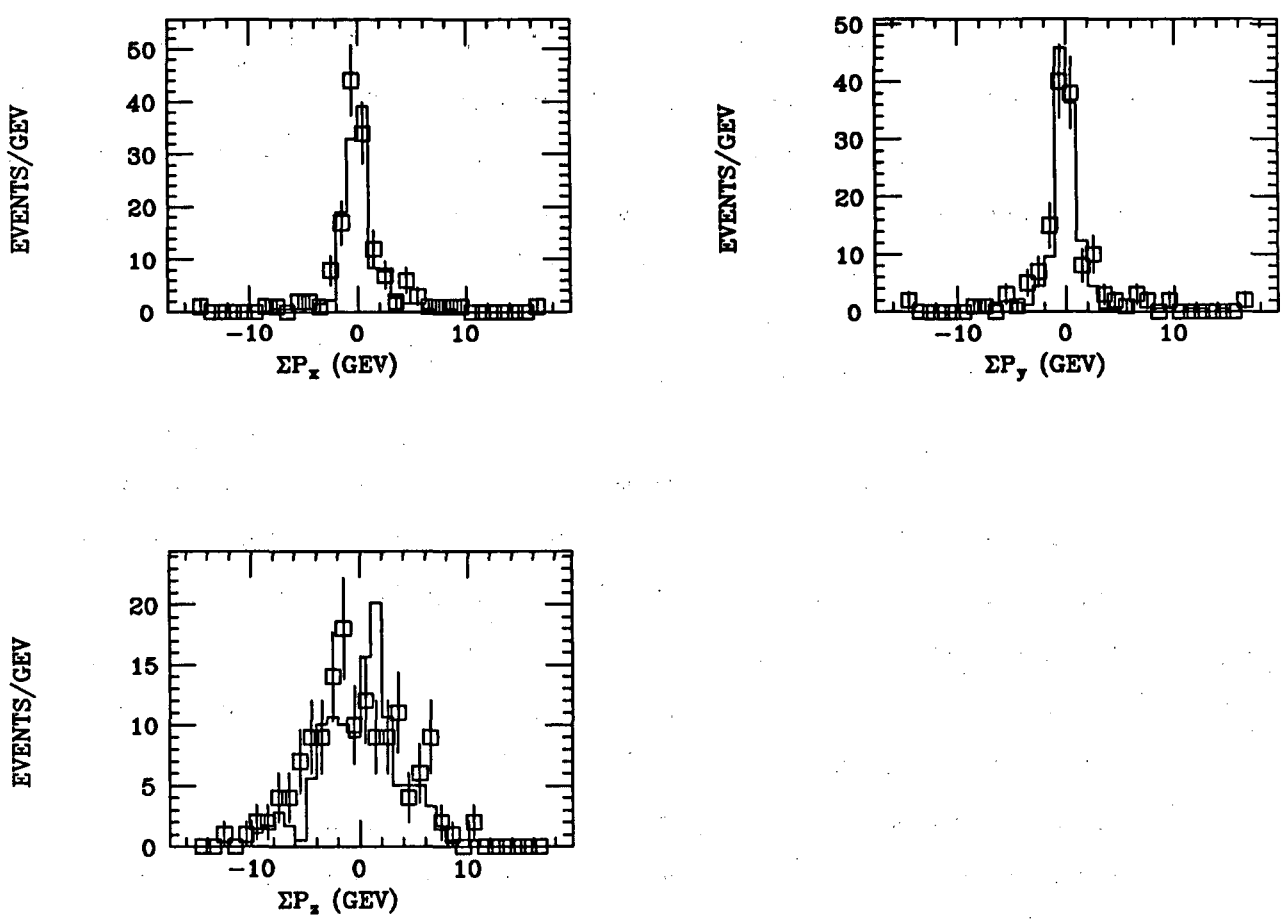

Figure 3.11. Momentum conservation along the x,y, and z axis for events with $\Delta\phi > 20$ mr. The solid histogram is a monte carlo calculation including additional initial state radiation.

section can only be defined in the context of this distribution. In QED the infrared divergence is not a real divergence but an artifact of the perturbation expansion.

The cancellation of infrared divergences is clearly apparent in the important case of μ-pair production. To calculate the cross section to $O(\alpha^3)$ one has to calculate two pieces, a soft piece and a hard piece. The soft piece is the square of the sum of all amplitudes with no photon in the final state that contribute to $O(\alpha^3)$, and the hard piece is the square of the sum of all amplitudes to this order with one photon in the final state. The infrared divergence is then parameterized in terms of the minimum energy photon (k_{min}) that distinguishes the two regions. It is chosen to be smaller then any practically detectable energy. The sum of soft and hard cross sections then gives the total cross section for detecting a μ-pair with a photon up to some detectable energy k_{max} :

$$\sigma^{\mu\mu(\gamma)}(k < k_{max}) = \sigma_o^{\mu\mu}(s)\Big(1 + \delta_P(s) + \delta_D(s, k_{min})\Big) + \int_{k_{min}}^{k_{max}} \frac{d\sigma^{\mu\mu\gamma}}{dk} dk \quad (3.2)$$

where $\sigma_o^{\mu\mu}$ is the point cross section.. The cancellation occurs because $\sigma^{\mu\mu(\gamma)}$ is independent of k_{min}. The term δ_P is finite and arises from the vacuuum polarization. The term δ_D contains all the other radiative corrections including the divergent piece. The total radiative correction $1 + \delta = 1 + \delta_P + \delta_D$ is plotted in Fig. 3.12 and Fig. 3.13 for the simplest case of initial state radiation only. [9]In this case the term δ_D takes on a simple form, $\delta_D = t_e \log(k_{min}/E_{beam}) = t_e \log x_{min}$. In figure 3.13 it is seen that for small enough values of k_{min} , $1+\delta$ becomes negative. This is because we have considered only single photon emission. For small values of k_{min} we should modify the formula to include the effects the emission of an infinite number of soft photons, [9]

$$\sigma_{soft} = \sigma_o^{\mu\mu}(1 + \delta_P + \delta_D) \rightarrow \sigma_o^{\mu\mu}(1 + \delta_P)e^{\delta_D}$$

where if only initial state radiation is included this takes on the simple form,

$$\sigma_{soft} = \sigma_o^{\mu\mu}(1 + \delta_P)e^{t_e \log x_{min}} = \sigma_o^{\mu\mu}(1 + \delta_P)x_{min}^{t_e}$$

Now as $k_{min} \rightarrow 0$, $\sigma_{soft} \rightarrow 0$. In order to maintain the cancellation between soft and hard pieces it is necessary to modify the hard emission,

$$\sigma^{\mu\mu(\gamma)}(k < k_{max}) = \sigma_o^{\mu\mu}(1+\delta_P)x_{min}^{t_e} + \int_{k_{min}}^{k_{max}} \left(\frac{d\sigma^{\mu\mu\gamma}}{dk}x^{t_e} + \frac{t_e}{k}\delta_P x^{t_e}\sigma_o^{\mu\mu}\right)dk$$

since $\frac{d\sigma^{\mu\mu\gamma}}{dk} \approx \frac{t_e}{k}\sigma_o^{\mu\mu}$ we have $\frac{d\sigma^{\mu\mu(\gamma)}}{dk_{min}} = 0$. When the emission of an infinite number of soft photons is included, the infrared divergence no longer appears.

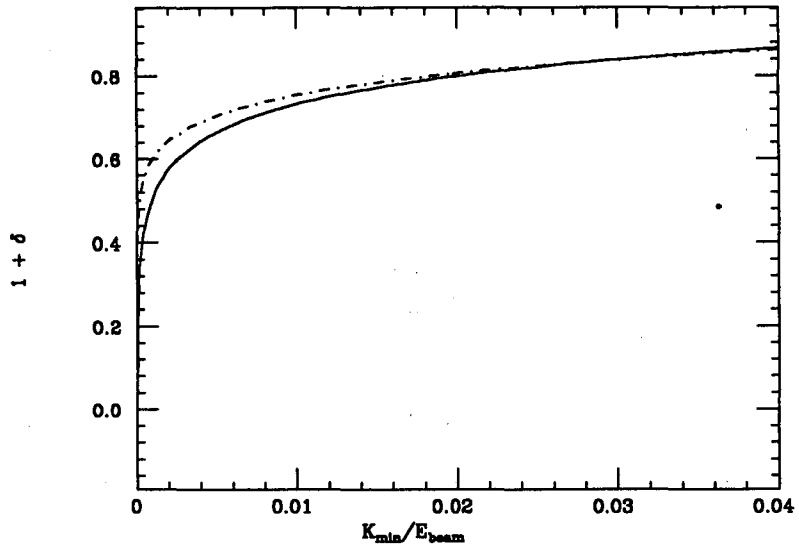

Figure 3.12. Radiative correction for initial state radiation only. Solid curve is without and dot dashed curve is with exponentiation.

Tsai has shown that the exponentiation arises naturally when radiative corrections are done to all orders in α using the renormalization group. [44] The modification of the soft photon cross section is then done in a general fashion applicable to the radiative corrections of hard photon processes. In general we have for the radiatively corrected cross section,

$$\sigma' = \sigma_o e^{\delta}$$

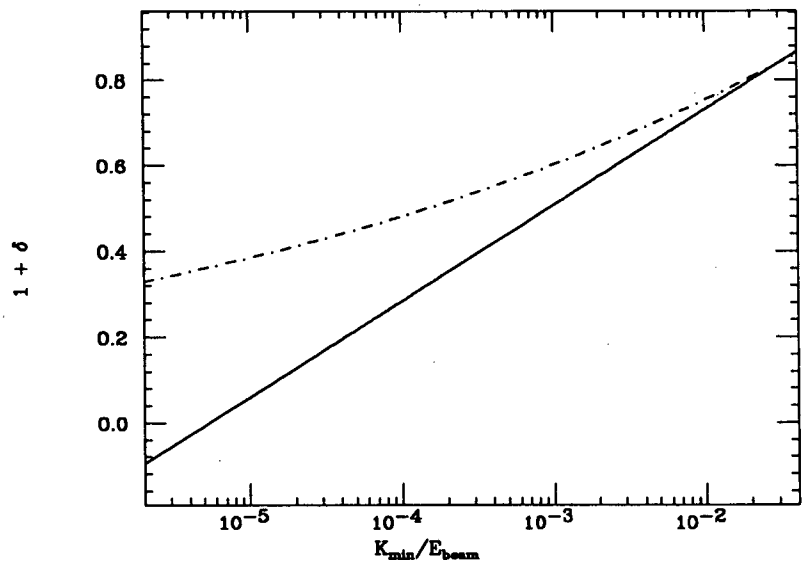

Figure 3.13. Same as 3.12 except the x axis is a logarithmic scale. The unexponentiated curve (solid) becomes negative and eventually diverges. The exponentiated curve (dot dashed) goes to zero at $k_{min}/E_{beam} = 0$.

In the simplest case of initial state radiation only, $\delta = t_e \log x$. Differentiating with respect to x then leads to the form of the cross section for hard photon emission with radiative corrections,

$$\frac{d\sigma'}{dx} = t_e x^{t_e - 1} \sigma_o$$

Since the lowest order cross section for hard photon emission is approximately $\frac{t_e}{k}\sigma_o$ we are led to modify formula 3.1 by the replacement, [45] [46]

$$\frac{1}{x} \rightarrow \left(\frac{1}{x}\right)^{1-t_e}.$$

3.5 Monte Carlo Generator

The Monte Carlo event simulation was built around the program of Berends, Kleiss, and Jadach (BKJ) which is valid for hard photon emission up to the kinematic limit and includes weak effects. [47] First, the infrared photon is generated.

In applying equation 3.1 we ignore the dependence on s' of $\sigma_{\mu\mu\gamma}$. This is done to simplify the generation and because the approximate formula 3.1 is only valid for small x– as $x \to 1$ the size of the cross section increases and it is necessary to go to higher order, $O(\alpha^4)$.

The infrared photons were generated according to the distribution,

$$f(x) = \frac{t_e}{2}(1 + (1-x)^2)x^{t_e - 1} \tag{3.3}$$

This form is convenient because the integral is trivial to perform analytically,

$$\mathcal{F}(x) = \int_0^x f(x')dx' = t_e\Big[\frac{1}{t_e}x^{t_e} - \Big(\frac{1}{t_e+1}\Big)x^{t_e+1} + \frac{1}{2}\Big(\frac{1}{t_e+2}\Big)x^{t_e+2}\Big]$$

A random number χ distributed according to $f(x)$ is then obtained from a random number η uniformly distributed between 0 and 1 by inverting $\mathcal{F}(x)$,

$$\chi = \mathcal{F}^{-1}(\eta).$$

The function $\mathcal{F}$ was inverted numerically using a self-learning binary search algorithm.

The generation of the $\mu\mu\gamma$ event according to the program of BKJ was the performed at the reduced center of mass energy, $s' = s(1-x)$. The 4-vectors p_+, p_-, p_γ were then boosted along the z axis to the laboratory frame by the boost $\beta = \pm x E_{beam}/(\sqrt{s} - xE_{beam})$, the sign being chosen at random with equal probability. Finally, since we are interested in events with a hard (visible) photon in the final state, only events with $E_\gamma > .15$ GeV and $|\cos\theta_\gamma| < .8$ were accepted. The cross section for these hard photon events is $\sigma^{\mu\mu\gamma} = 18.69$ pb . A sample corresponding to an integrated luminosity of $\mathcal{L} = 360$ pb^{-1} was generated.

3.6 Kinematic fitting

The events are fitted assuming that the missing energy due to initial state radiation E_Δ is radiated along the beam direction. This is an excellent approximation

since the angular distribution of initial state radiation is highly peaked along the beam direction. The angular distribution is given by , [41]

$$\frac{d\sigma^{\mu\mu\gamma}}{d\Omega_\gamma} \propto \frac{\sin^2\theta_\gamma}{(1-\beta^2\cos^2\theta_\gamma)^2}$$

where $\beta = \sqrt{1-\frac{4m_e^2}{s}}$ is the velocity of the incident electron. Then the probability for emitting a photon with $|\cos\theta_\gamma| > x$ is,

$$P(x) = 1 - \frac{\log(\frac{1+\beta x}{1-\beta x}) - \frac{4m_e^2}{s}(\frac{x}{1-\beta^2x^2})}{\log\frac{s}{m_e^2} - 1}$$

Some examples of P(x) at $\sqrt{s} = 29$ GeV are shown in Table 3.2 We can check that this is a good approximation by studying the angular distribution of the missing momentum, $\vec{P}^{miss} = -\vec{p}_+ - \vec{p}_- - \vec{p}_\gamma$ for events with large aplanarity , $\Delta\phi > 20$ mr. This distribution is shown in Fig. 3.14 The comparison with the Monte Carlo, which assumed the missing energy is along the z axis, demonstrates that for our purposes the angular distribution may be safely neglected. As a further check in Fig. 3.15 we see that Monte Carlo reproduces the aplanarity distribution.

Table 3.2. The probability P(x) for an initial state photon to be emitted with $|\cos\theta| > x$ at $\sqrt{s} = 29$ GeV.

x	.9999	.999	.99	.9	.8	.7
P(x)	.53	.64	.74	.86	.90	.92

Using the angle measurements alone and assuming that the missing energy E_Δ is along the beam direction, energy-momentum conservation gives four equations for the four quantities p_+, p_-, E_γ, and E_Δ .

$$E_+ + E_- + E_\gamma + E_\Delta = \sqrt{s}$$

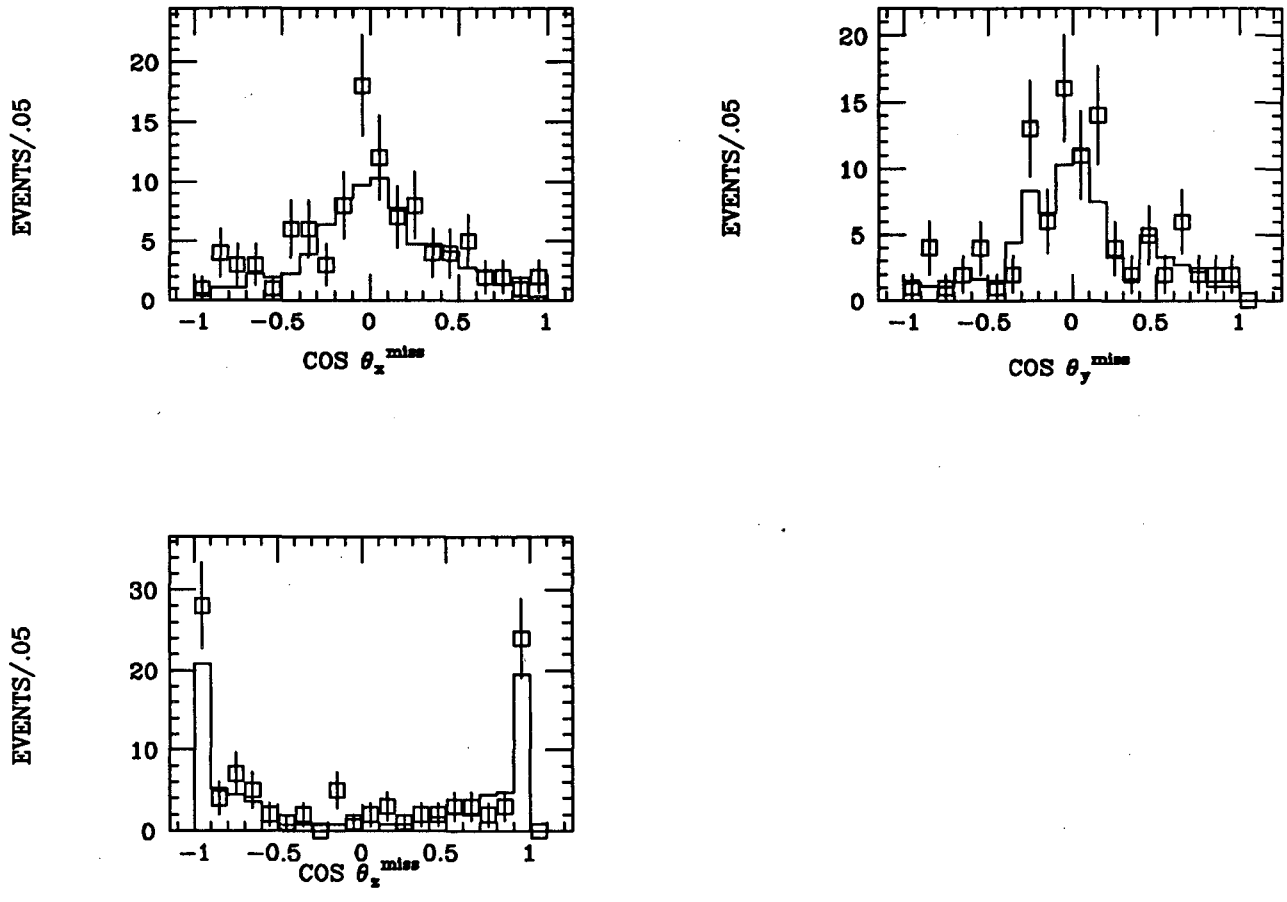

Figure 3.14. The projections of the missing momentum along the x, y, and z axes for $\mu\mu\gamma$ events with $\Delta\phi > 20$ mr. The angles θ_i^{miss} are defined by $\cos\theta_i^{miss} = p_i^{miss}/p^{miss}$ for i= x, y, and z. The solid histogram is Monte Carlo with missing momentum generated along the beam axis only.

$$\vec{p}_+ + \vec{p}_- + \vec{p}_\gamma + \epsilon E_\Delta \hat{z} = \vec{0}$$

where $\epsilon = \pm 1$ and will be determined by the requirement $E_\Delta > 0$. If we ignore the muon mass and set $E_\pm = p_\pm$ then these equations are easily solved. Writing $X_i = \vec{p}_i \cdot \hat{x}$ *etc.* for $i = +, -, \gamma$:

$$R_i = X_j Y_k - Y_j X_k \qquad i, j, k \;\; cyclic$$

$$D = \sum_i (\epsilon - Z_i) R_i$$

The solution is then,

$$E_\Delta = \frac{-\sqrt{s}}{D} \sum Z_i R_i$$

$$p_i = \frac{\epsilon\sqrt{s}}{D} R_i$$

As a check we note that $\sum p_i + E_\Delta = \frac{\sum(\epsilon - Z_i)R_i}{D}\sqrt{s} = \sqrt{s}$. The missing energy E_Δ is shown in Fig. 3.16 and agrees very well for small E_Δ.

We can use the Monte Carlo to check the energy resolution for the fitted E_γ energy compared to the energy measured in the liquid argon, E_{LA}. We find that the fitted energy is on the average better then $.5\sigma_E = .07\sqrt{E}$ even for the smallest energy, $E = .5$ GeV. This is shown in Fig. 3.17. As a further check we compare the fitted quantities $p_\pm$ and E_γ with the quantities measured in the detector. This comparison, shown in Fig. 3.18, is done in units of the measured error. The distributions are all approximately gaussian with width equal to the measurement error, demonstrating that the error on the fitted quantities is small compared to the measured errors.

We now make the following final cuts on fitted quantities:

1. $E_\gamma > .5$ GeV
2. $E_\Delta < 1$ GeV
3. $M_{\mu\mu} > 1.2$ GeV

The first cut was made because the fitted energy E_γ is more precisely measured then the liquid argon energy. The second cut is made to reduce the contribution

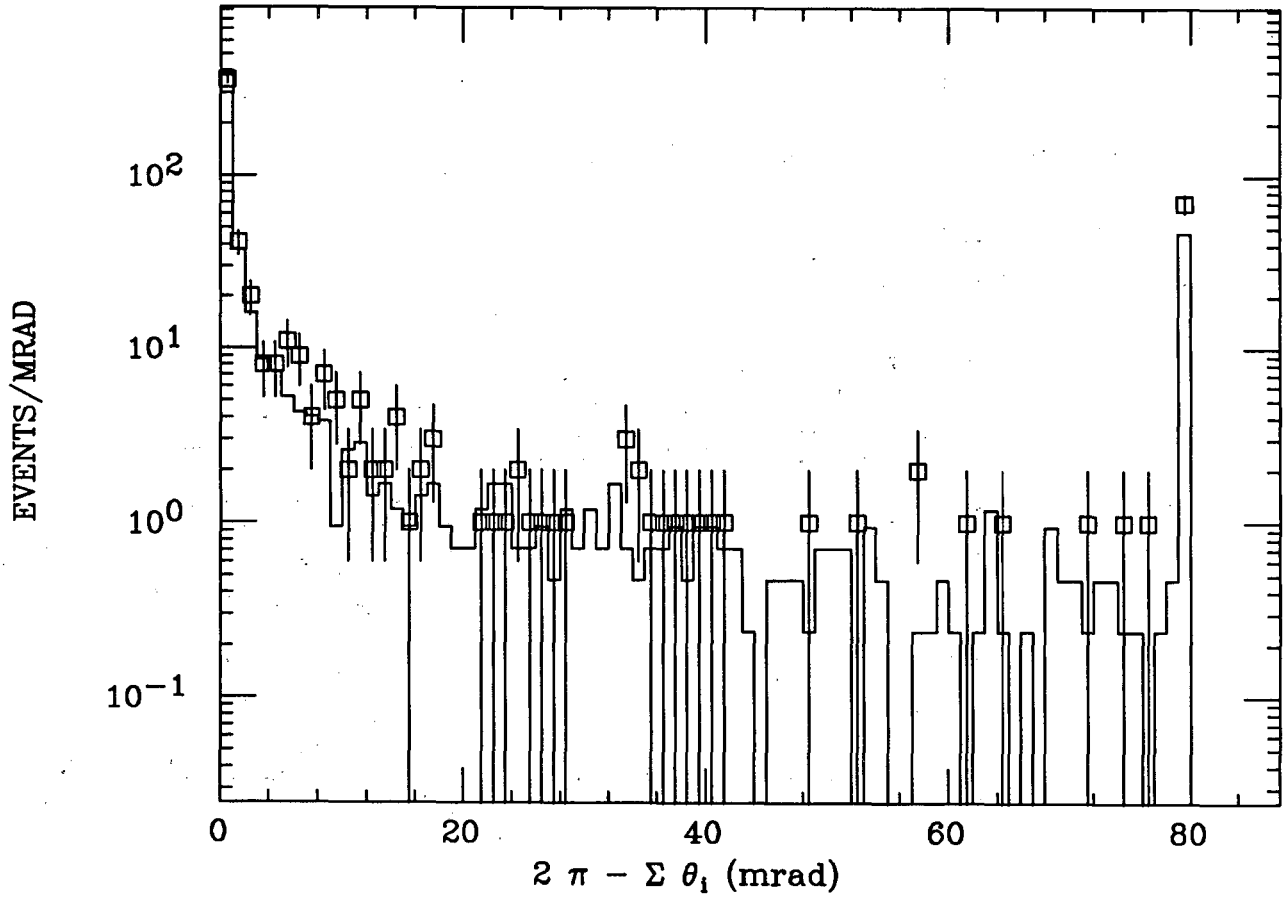

Figure 3.15. Monte Carlo calculation (solid histogram) of aplanarity distribution including higher order initial state radiation. The data (points) are the same as 3.10 . The last bin is an overflow bin, the complete distribution having a long tail that is reproduced by the monte carlo.

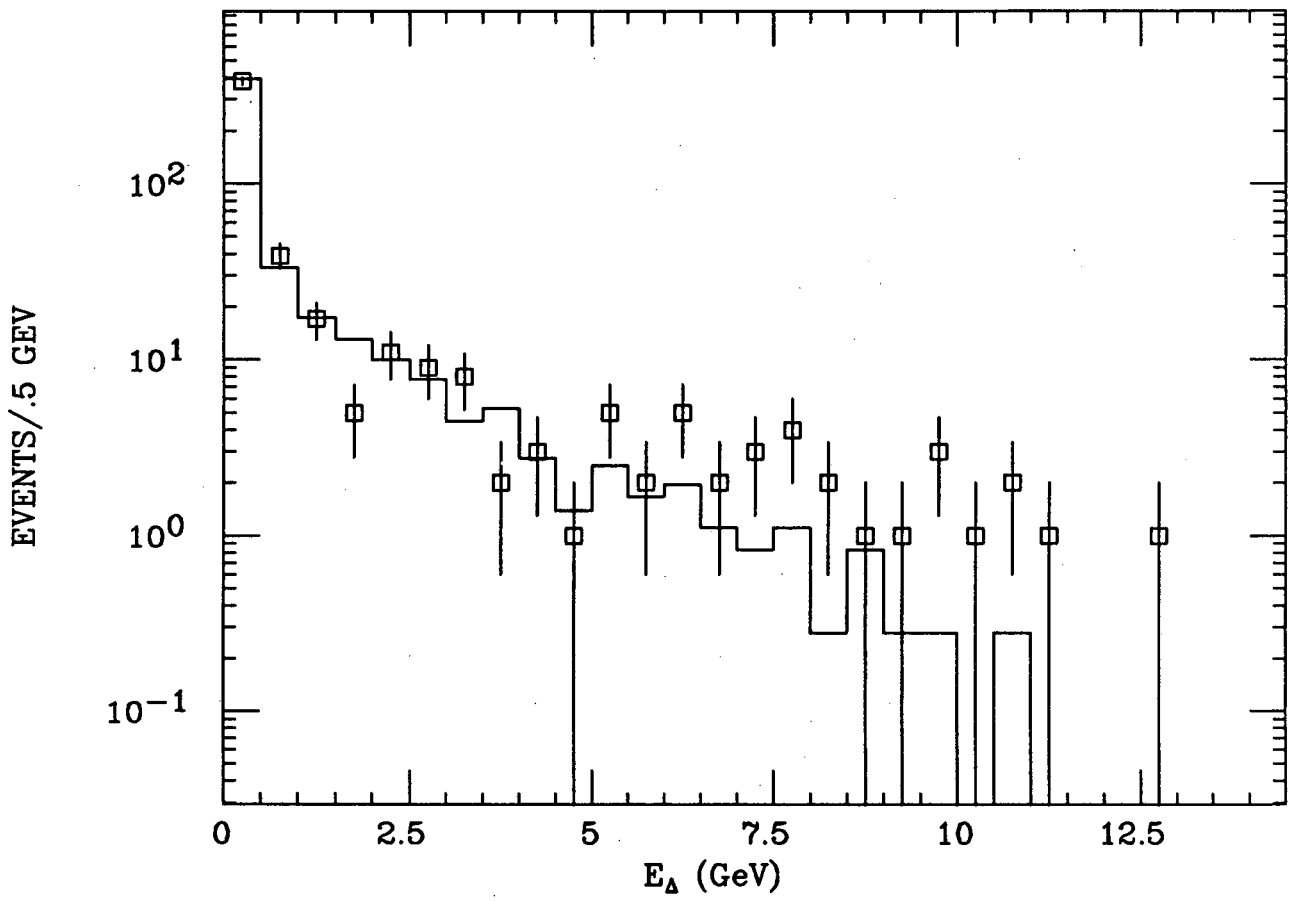

Figure 3.16. The missing energy E_Δ in the data (points) and the Monte Carlo (solid histogram).

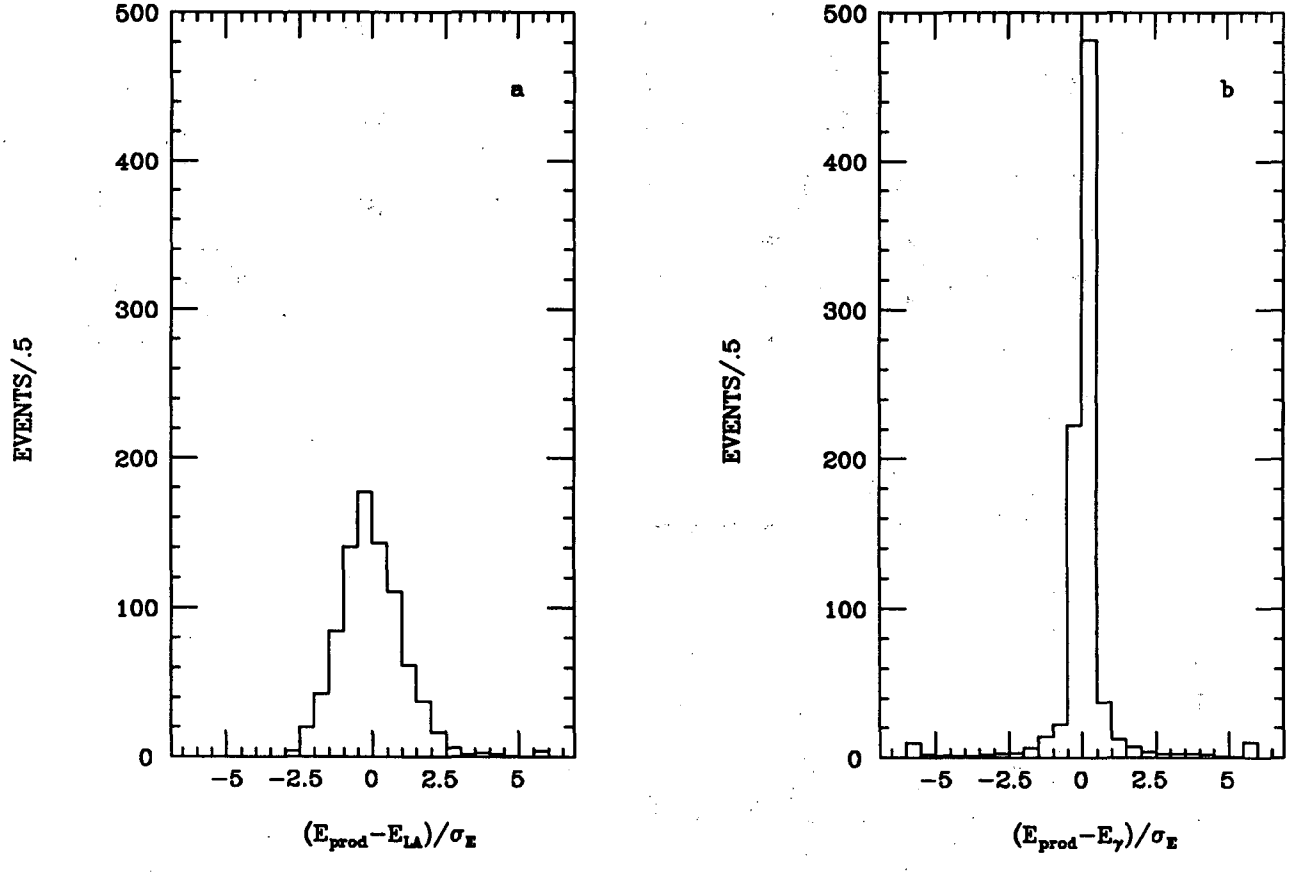

Figure 3.17. The liquid argon energy E_{LA} (a) and fitted energy E_γ (b) compared to the produced energy in the Monte Carlo in units of the liquid argon energy resolution.

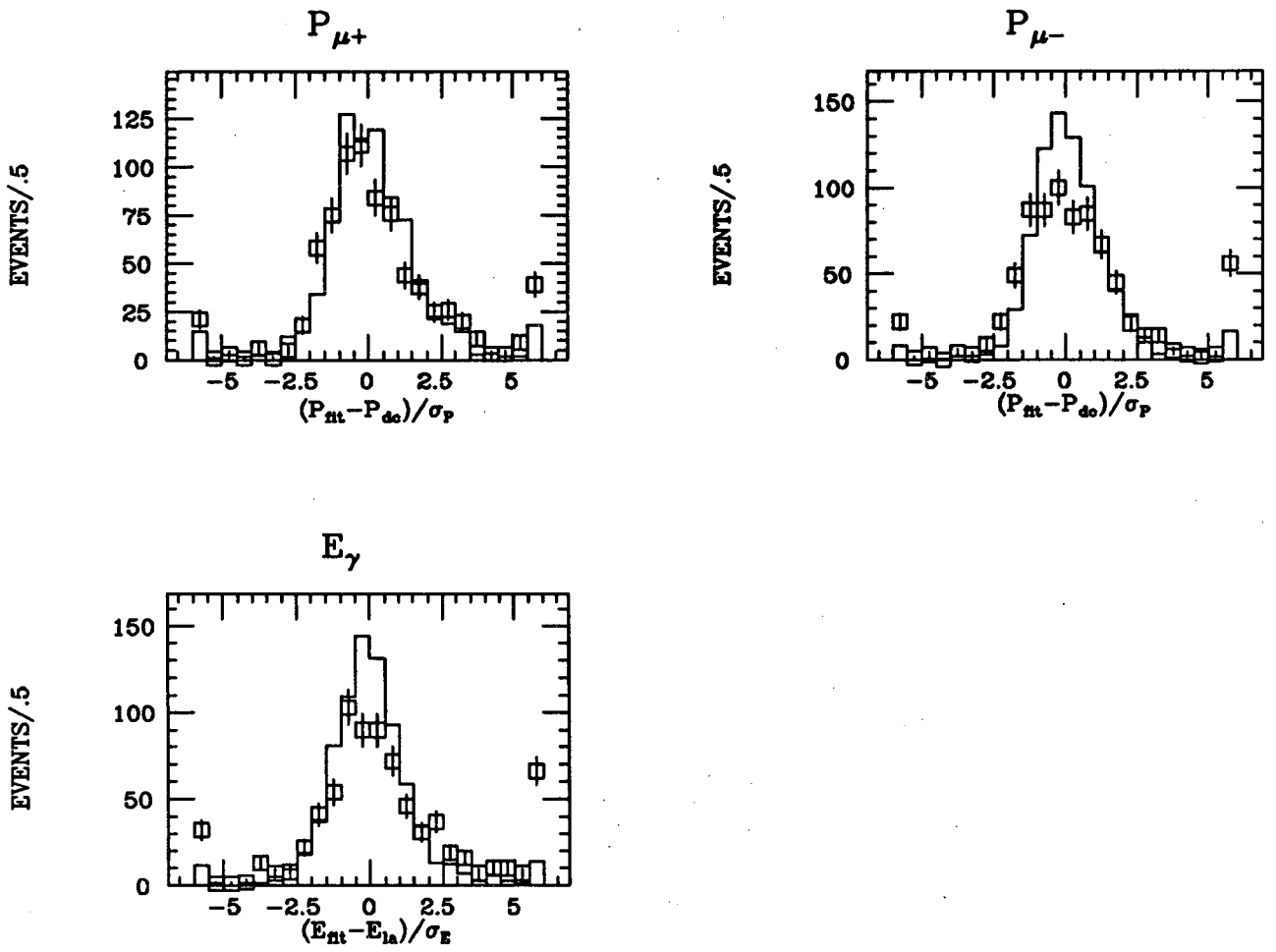

Figure 3.18. The difference between fitted and measured quantities in units of the measured error.

from higher order QED processes. The third cut is made for two reasons: 1) the efficiency is reduced for tracks very close together due to the "anti-chatter" feature of the hardware trigger and the track reconstruction in the drift chamber; the background from $ee \rightarrow \pi\pi\gamma$ is expected to be large when the $\pi\pi$ mass recoiling against the photon is near the mass of the ρ . The cross section for $ee \rightarrow \pi\pi\gamma$ due to the ρ is estimated in Appendix B and is consistent with the number of events seen and our estimated efficiency in this region.

With these cuts we find 350 events. The Monte Carlo calculation predicts 379 events. The only non-negligible background remaining is due to $\tau\tau(\gamma)$. This background is estimated with the Monte Carlo to be $(2 \pm .7)\%$ or 8 ± 3 events. Adding in this backgound we find the ratio of detected (exp) to predicted (th) events,

$$\frac{\sigma^{exp}}{\sigma^{th}} = .90 \pm .05 \pm .06$$

where the first error is statistical. In addition to the systematic uncertainty from the luminosity we estimate a systematic uncertainty of 3% from our cuts as sumarized in Table 3.3. This ratio has been measured previously by the MAC collaboration who found $.97 \pm .06$ and by the JADE collaboration who obtained $.92 \pm .06$. [48] [49] (The errors on these measurements are statistical only.)

Table 3.3. Summary of systematic uncertainties due to cuts.

cut	N_{exp}	$\Delta N_{exp}/N_{exp}$	$\Delta N_{th}/N_{th}$	$\Delta N/N$
$E_\gamma > .7$	305	-.12	-.10	-.02
$E_\gamma > .3$	383	.10	.08	.02
$E_\Delta < .5$	311	-.10	-.06	-.04
$E_\Delta < 1.5$	356	.03	.04	-.01

3.7 FITTED DISTRIBUTIONS

The distributions for the fitted quantities E_γ, $M_{\mu\mu}$, and $M_{\mu\gamma}$ are shown in Fig. 3.19, Fig. 3.20, Fig. 3.21, The E_γ distribution has the shape characteristic of QED– falling off inversely with increasing energy but with a sharp peak at high photon energy due to the initial state amplitude being inversely proportional to the square of the center of mass energy after radiation. The cut-off of the $\mu\gamma$ spectrum for small masses is a result of the cut on $\theta_{\mu\gamma}$. at 20°. This eliminates events with very small $M_{\mu\gamma}$ which would otherwise result in a large peak for small ($M_{\mu\gamma} < 1$ GeV) masses due to final state radiation. The Cello collaboration has observed an excess of high $\mu\gamma$ mass events at a slightly higher center of mass energy. For center of mass energy in the range $33 < \sqrt{s} < 46$ GeV and $M^2_{\mu\gamma}/s > .8$ they observe 11 events where 2.6 are expected from QED. [50] In a the same kinematic region at $\sqrt{s} = 29$ GeV, $M_{\mu\gamma} > 26$ GeV , we clearly see no excess of events: 14 where 16 are expected from QED. This situation, if the Cello result is not a statistical accident (1/16000) or the result of a systematic error, cannot be explained by the μ^* coupling of the lagrangian 1.3 or lagrangian 1.4 , but might be described by an $ee\mu\mu^*$ contact interaction. [51]

3.8 ASYMMETRY

As discussed in the introduction, the interference between initial and final state radiation gives rise to a forward-backward charge asymmetry in $\mu\mu\gamma$ events. As a generalization of the forward-backward asymmetry in collinear events we consider the polar distribution of both μ^+ and μ^- in each event and define the charge asymmetric quantity,

$$A = \frac{N_f - N_b}{N_f + N_b}, \tag{3.4}$$

where $N_f(N_b)$ is the number of muons with $q\cos\theta > 0 (q\cos\theta < 0)$, θ is the angle between the charged particle momenta and the positron beam, and q is the muon charge in units of $|e|$. A small number of events (5 out of 350) were removed that did

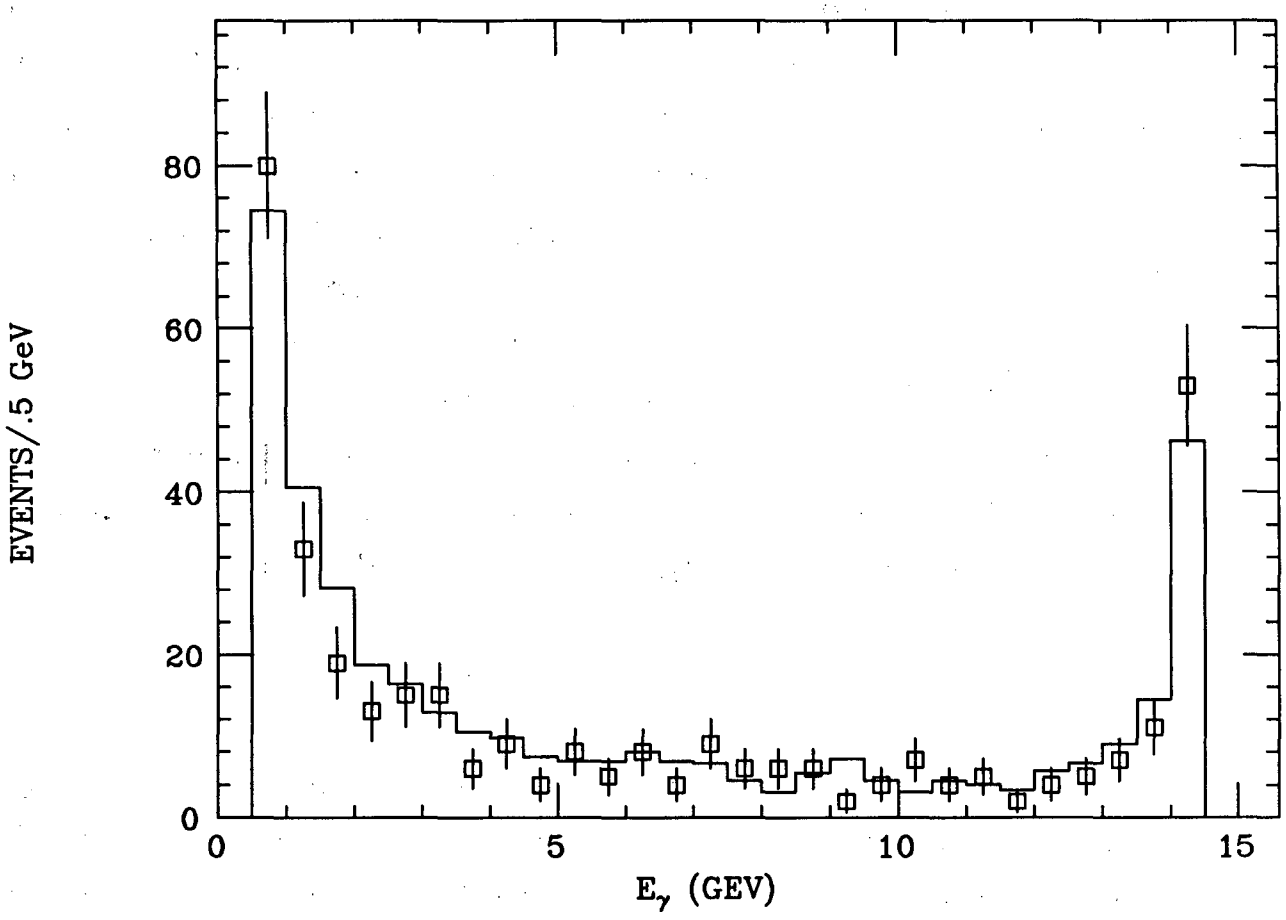

Figure 3.19. Result of kinematic fit for the energy of the detected photon. The solid histogram is the Monte Carlo calculation.

not satisfy $q_1 q_2 = -1$, a number consistent with that expected from charge missasignments. (In fact, we can take this as a measure of the probability w of assigning the correct charge to a track: $(2w-1)^2 = -\langle q_1 q_2 \rangle$ so that $w = -.993 \pm .002$.) [52]

The charge asymmetry in this process exhibits strong dependence on various kinematic variables that change the relative strengths of the initial and final state amplitudes. This behavior is illustrated in Table 3.4. for θ_γ , the angle of the photon momentum with respect to the positron beam, and for the photon energy E_γ. The depedence on θ_γ is understood in terms of the forward peaking of initial state radiation– the initial, final state amplitudes are more comparable for wide angle photons. Similarly, the dependence on E_γ is understood in terms of the rapid fall off of the final state amplitude with increasing E_γ as shown in Fig. 1.3.

The $q \cos\theta$ distrubution is shown in Fig. 3.22, which exhibits a strong asymmetry for the $\mu^\pm$ to be in the backward hemisphere with respect to the $e^\pm$ beam. The contribution from background to the asymmetry A is negligible (.4%). The systematic uncertainty due to the cuts is small in comparison to the statistical error. In Table 3.5. we estimate the systematic uncertainty due to the cuts on E_γ and E_Δ to be .12 for the ratio A_{exp}/A_{th}. We find for the ratio,

$$\frac{A_{exp}}{A_{th}} = .83 \pm .25 \pm .12,$$

where the statistical error of the measurement has been added in quadrature to the statistical error of the Monte Carlo calculation. The statistical errors were calculated according to the formula given in Appendix C. In terms of the asymmetries themselves we find,

$$A_{exp} = (-19.4 \pm 4.6 \pm 2.8)\% \quad .$$

$$A_{th} = (-23.5 \pm 2.2)\% \quad .$$

The Monte Carlo calculation includes electroweak corrections. The contribution from electroweak corrections is small and is estimated by letting $m_Z \to \infty$ to be $(3 \pm 2)\%$. Other experiments have found similar agreement. [48] [49]

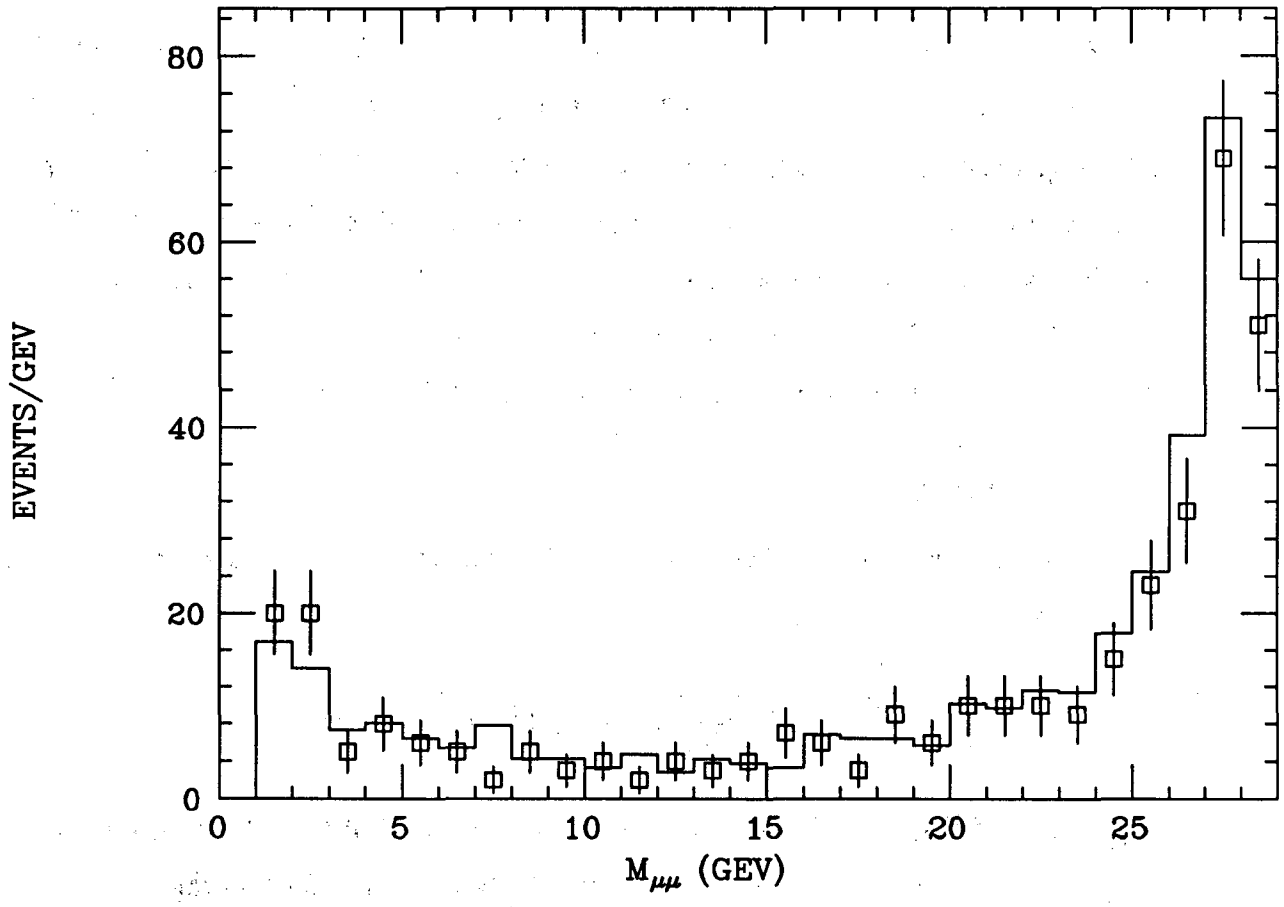

Figure 3.20. Result of the kinematic fit for the μ-pair mass. The solid histogram is the Monte Carlo calculation.

3.9 μ^* COUPLING LIMIT

The $\mu\gamma$ distribution can be used to place a limit on the electromagnetic coupling of a possible excited muon (μ^*) to the muon and the photon. The limit depends on the following factors (in this section, the excited muon mass will be denoted by M):

$$\left(\frac{G_\gamma}{M}\right)^2 < \frac{1}{A(M)}\frac{1}{\tilde{\sigma}(M,s)}\frac{1}{L}N(M).$$

$A(M)$ is the acceptance for detecting a μ^* . $\tilde{\sigma}(M,s)$ is the radiatively corrected cross section for producing the μ^* divided by the factor $\left(\frac{G_\gamma}{M}\right)^2$. L is the gross integrated luminosity. $N(M)$ is the number of possible excited muons that could be hidden in the data based on the number of detected events, the number of predicted QED events, and the $\mu\gamma$ mass resolution of the detector. The most reliable way to calculate A and N is with the construction of a μ^* Monte Carlo generator with which we can use our full detector simulation and exactly reproduce our $\mu\mu\gamma$ analysis.

3.9.1 μ^* Monte Carlo

The angular distribution for μ^* production can be calculated from the lagrangian 1.3 and is given by, [11]

$$\frac{d\sigma}{d\Omega} = \frac{\alpha^2}{2}\left(\frac{G_\gamma}{M}\right)^2(1-\rho)(1-\rho^2)(1-\beta\cos^2\theta)$$

where $\rho = M^2/s$ and $\beta = (1-\rho)/(1+\rho)$is the velocity of the μ^* in the laboratory. The decay of the μ^* to $\mu\gamma$ can also be calculated from the lagrangian 1.3 . As shown in Appendix D the decay is isotropic with the rate $\Gamma = \frac{1}{2}\alpha\left(\frac{G_\gamma}{M}\right)^2 M^3$. For $\left(\frac{G_\gamma}{M}\right)^2 \sim 10^{-5}$ GeV^{-2} this gives a lifetime of $\tau \sim 10^{-17}/M(\text{GeV})^3$ sec, so that we assume the lifetime is negligible.

Event generation was performed with the event generation package SAGE. [53] The events are generated according to the phase space distribution and then

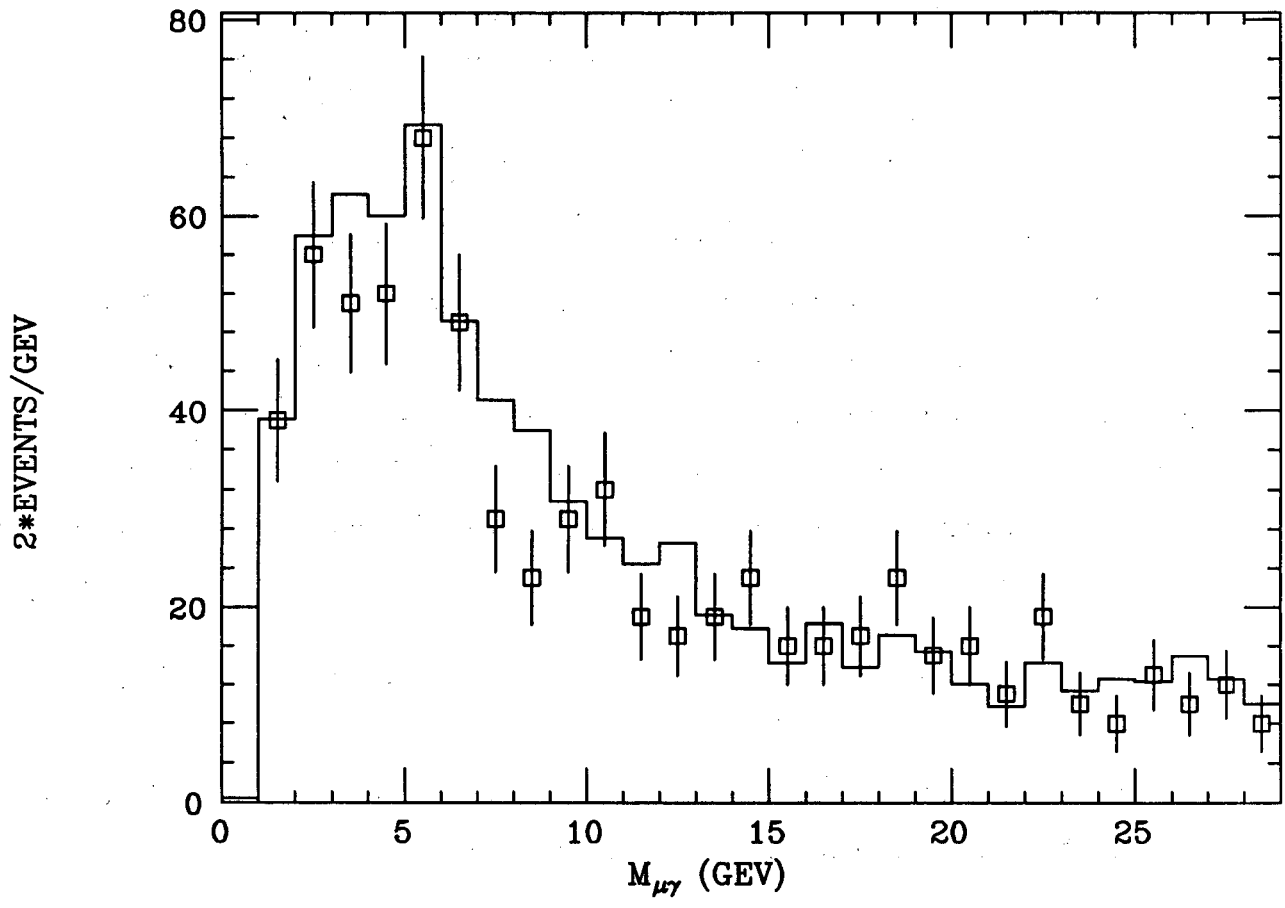

Figure 3.21. Result of the kinematic fit for the $\mu\gamma$ mass. Both masses are plotted for each event. The solid histogram is the Monte Carlo calculation.

Table 3.4. The charge asymmetry A exhibits a strong dependence on the angle of the photon with respect to the beam θ_γ and on photon energy E_γ.

cut	A_{exp}	A_{th}
$\cos\theta_\gamma < .2$	-27.6 ± 5.9	-33.2 ± 2.8
$.2 < \cos\theta_\gamma < .4$	5.4 ± 13.2	-6.9 ± 5.9
$\cos\theta_\gamma > .4$	-4.4 ± 7.2	-0.6 ± 3.4
$E_\gamma < 3$	-31.3 ± 7.4	-34.3 ± 3.4
$3 < E_\gamma < 13$	-18.1 ± 8.1	-18.7 ± 3.7
$3 < E_\gamma > 13$	4.2 ± 6.4	-4.4 ± 3.5

weighted by the square of the matrix element. (see Appendix D) Radiative corrections were done for initial state radiation. [54] This tended to decrease the acceptance. Events were generated for selected masses and then passed through our detector simulation. The calculated acceptance function is shown in Fig. 3.23.

Radiative corrections to the cross section are calculated according to equation 3.2 ,

$$\tilde{\sigma}' = \tilde{\sigma}_o(M,s)(1+\delta_P + t_e \log x^1) + \int_{x^1}^{x_{max}} \tilde{\sigma}_o(M,s')t_e\Big(\frac{1+(1-x)^2}{2}\Big)\frac{dx}{x}$$

where $\tilde{\sigma}_o(M,s) = 2\pi\alpha^2(1-\rho^2)(1-\rho)(1-\beta/3)$ and $x_{max} = 1-(M+m_\mu)^2/s$. The effect of the radiative correction is shown in Fig. 3.24,

3.9.2 Maximum likelihood limit

The function N(M) is calculated using the maximum likelihood method. To use this method we need to know the probibility density functions for the QED background $P(m)$ and for the μ^* of mass M, $P^*(M,m)$ where m is the $\mu\gamma$ mass. For $P(m)$ we use our QED Monte Carlo as described previously. We also use this to measure the $\mu\gamma$ mass resolution function $r(m)$. This function is shown in Fig. 3.25. The function $P^*(M,m)$ is needed as a continuous function of M so that we require

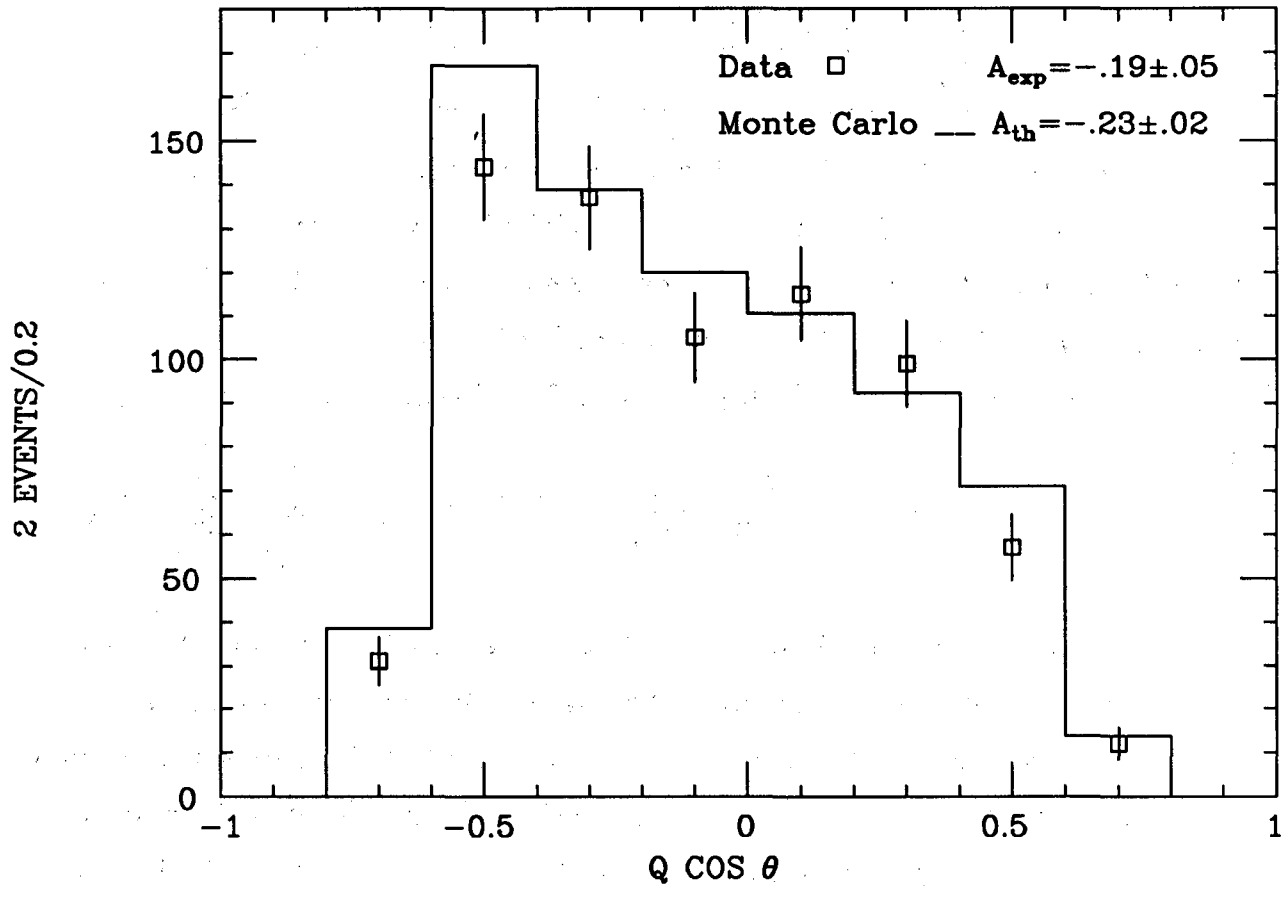

Figure 3.22. The forward-backward charge asymmetry for $ee \to \mu\mu\gamma$. The solid histogram is $O(\alpha^3)$ QED Monte Carlo with electroweak corrections. The error on the calulation is due to statistics.

Table 3.5. Summary of systematic uncertainties on the ratio $R_A = A_{exp}/A_{th}$.

cut	A_{exp}	$\Delta A_{exp}/A_{exp}$	$\Delta A_{th}/A_{th}$	$\Delta R_A/R_A$
$E_\gamma > .7$	-.16	-.17	-.06	-.11
$E_\gamma > .3$	-.20	.03	- .07	.10
$E_\Delta < .5$	-.19	-.04	-.06	-.02
$E_\Delta < 1.5$	-.18	-.07	-.04	-.03

a parameterization. The function is simply parameterized by a gaussian of width $r(M)$ together with a combinatoral background function (see Appendix D). This function is shown in Fig. 3.26 for two representative values of M and is seen to reproduce the shape of the Monte Carlo distribution.

We then minimize the negative logarithm of the likelihood function,

$$-\log \mathcal{L}(N, N^*) = -\sum_{i=1}^{2N_{evts}} \log\left[\frac{NP(m_i) + N^*P^*(M, m_i)}{N + N^*}\right] + \frac{(N - N_o)^2}{2\Delta N_o}.$$

The first term comes from the product in the likelihood $\mathcal{L}$ of the probability for measuring each data point $m_i = M_{\mu\gamma}$ measured. The second term takes into account the uncertainty in the normalization of the QED process. The minimization was done using the program MINUIT. [55] The resulting limit is shown in Fig. 3.27. For excited muon masses in the range $1 < M < 21$ GeV we find the limit, $(G_\gamma/M)^2 < 10^{-5}$ GeV^{-2} at a 95% confidence level. A comparable limit has been obtained previously. [49]

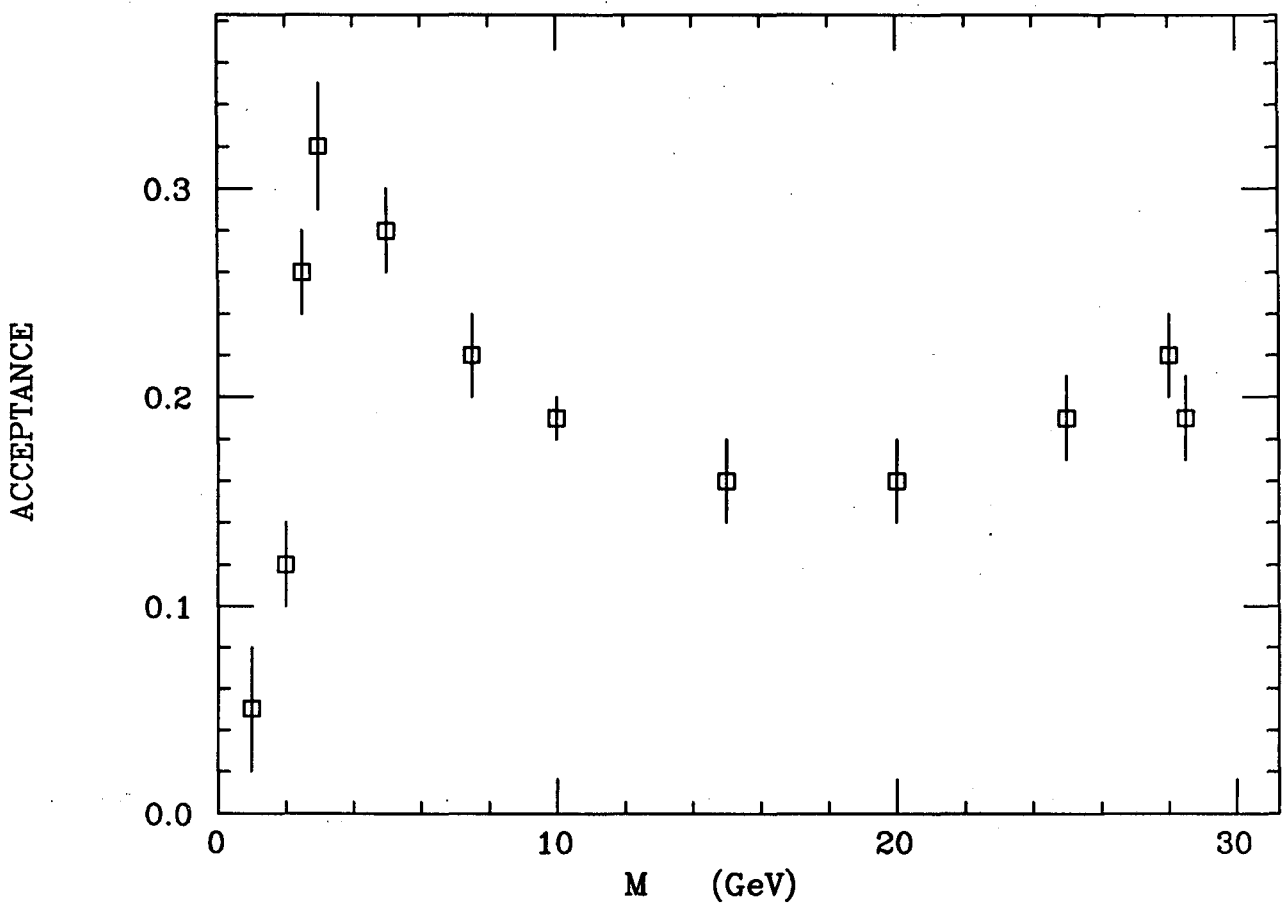

Figure 3.23. Acceptance function for μ^* as a function of mass M.

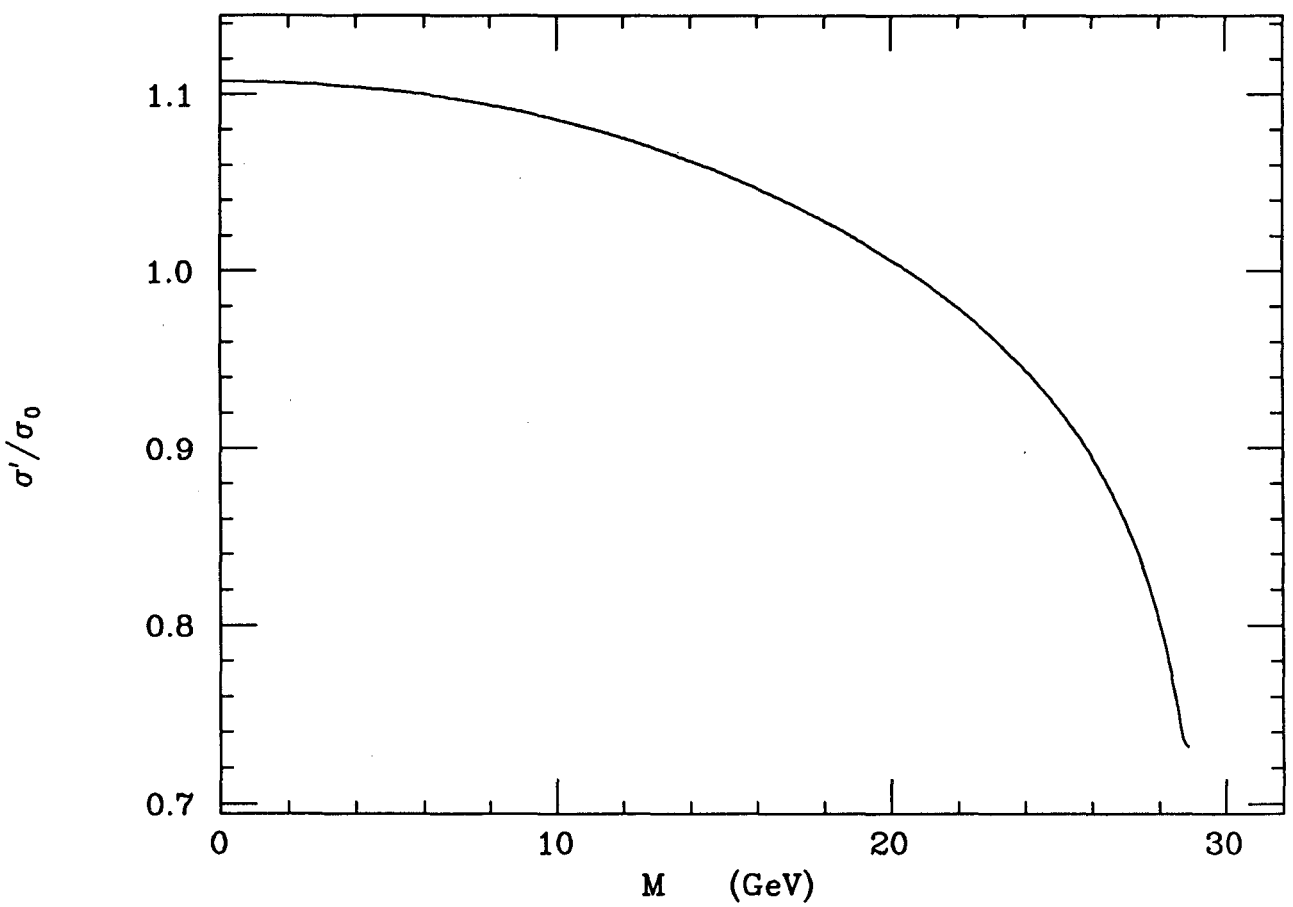

Figure 3.24. Radiative correction to the μ^* cross section.

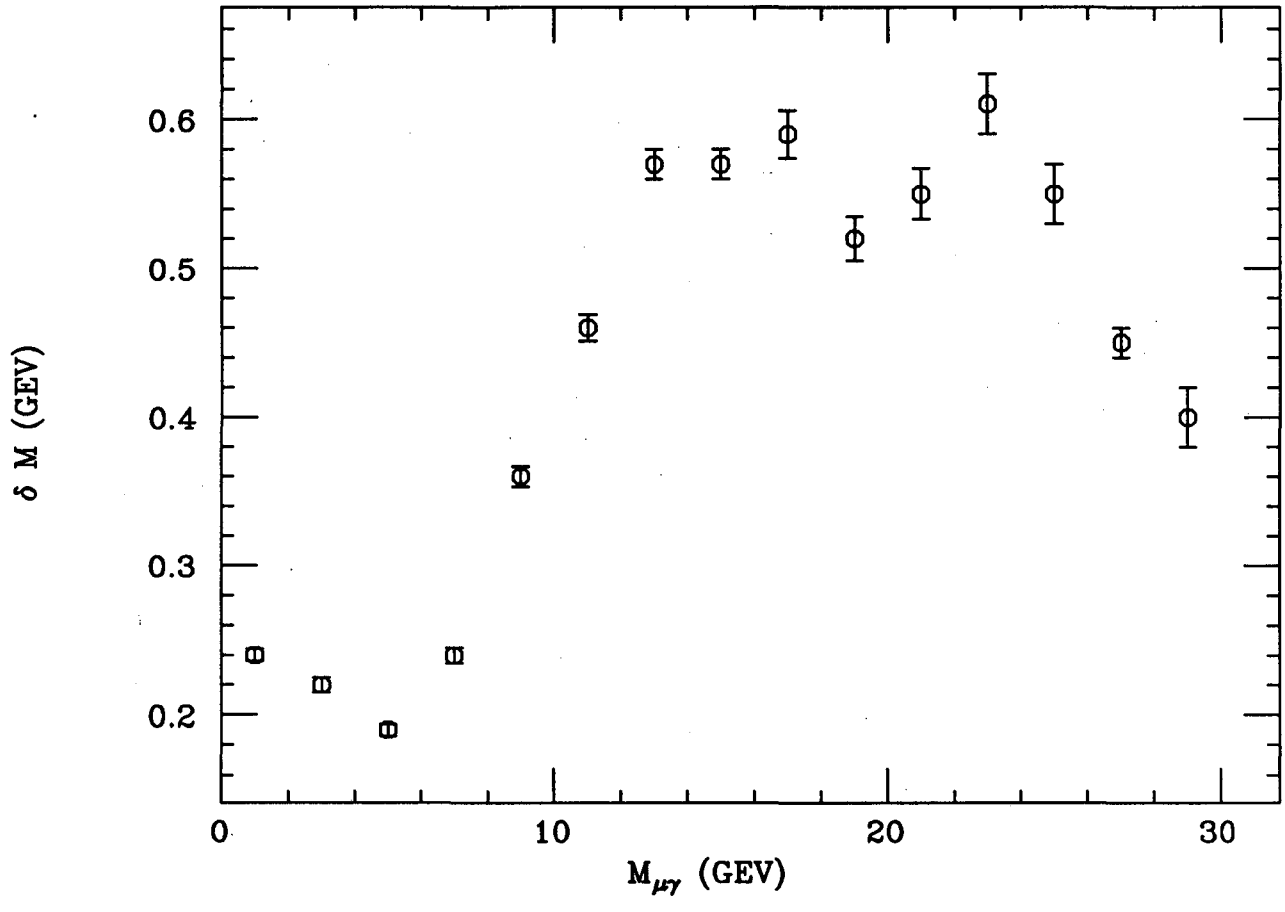

Figure 3.25. $\mu\gamma$ mass resolution calculated from Monte Carlo.

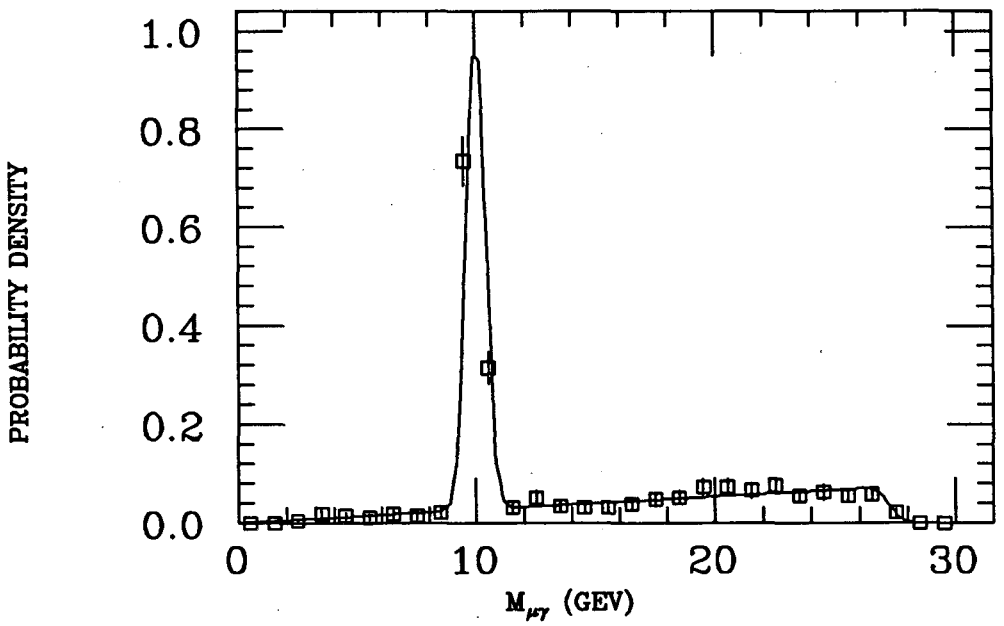

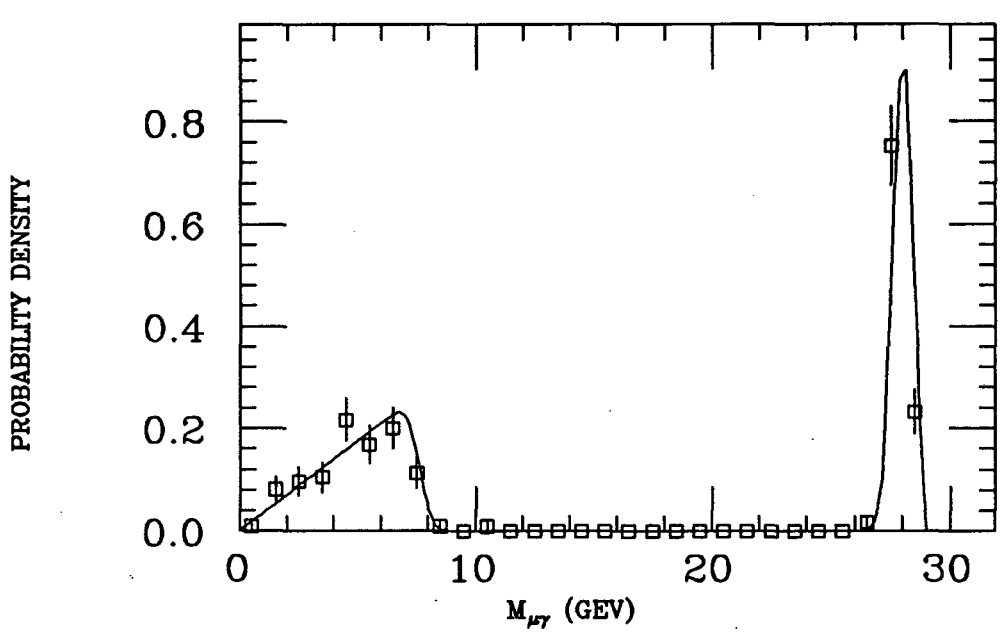

Figure 3.26. $M_{\mu\gamma}$ distribution for $M = 10$ GeV (top) and $M = 28$ GeV (bottom). Points are the SAGE Monte Carlo calculation, and the solid curve is the parameterization. The low mass bump in the lower plot is due to kinematics.

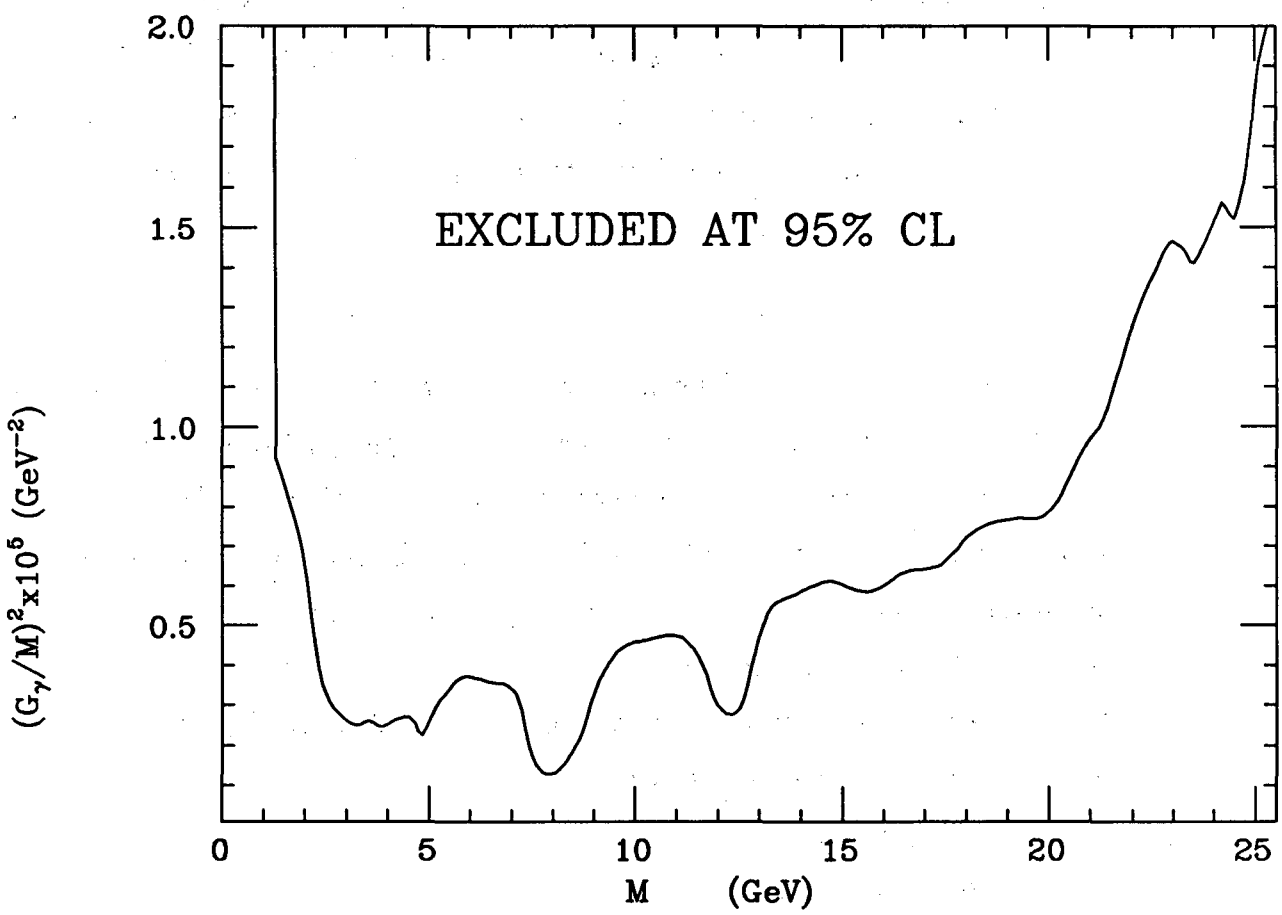

Figure 3.27. Limit on μ^* coupling to the photon as a function of μ^* mass at 95% CL. The peculiar dips in the curve reflect statistical fluctuations in the data.

4. Hadrons + γ

To study the analogous process to $\mu\mu\gamma$ for the hadronic final state we select hadronic events with hard photons ($E_\gamma > 3.0$ GeV) where the hard photon has a high probability of being direct. By direct photons we will mean photons which are not the decay products of radiatively decaying hadrons. The primary source of non-direct background comes from π^0, η decays. We can make use of the "2-jettiness" of hadronic events at 29 GeV and the high multiplicity ($\langle N_{ch} \rangle = 13$) [56] by selecting events with hard and isolated neutral tracks. We will find that these requirements yield a high signal to noise ratio with little ambiguity (the probabilty of an event having more then one hard photon is small).

4.1 Event Selection

Hadronic events are characterized by a high particle multiplicity. The primary backgrounds are the multiparticle decay modes of the τ, higher order hadronic processes (two photon production of hadrons and radiative bhabha events where the radiated photon materializes as hadrons) , and interactions of the beams with residual gas in the vacuum pipe. These backgounds can be significantly eliminated by the following requirements.

1. At least 5 charged tracks reconstructed in the main drift chamber.
2. A reconstructed vertex with

   $Z_v < .08$ m

   $R_v < .02$ m

   measured with respect to the interaction region as determined by the beam position monitor.
3. Good charged tracks must satisfy

   $p_\perp > .1$ GeV

   $r_m < .05$ m

   $z_m < .08$ m

   The number of good charged tracks (N_{ch}) was required to be greater then 4.

4. Good neutral tracks must satisfy,

   Shower centroid located within the fiducial volume of the liquid argon system

   $E_{la} > .3$ GeV

   $D_{min} > .1$ m, where D_{min} is the minimum distance of the shower centroid to the nearest projected charged track at the liquid argon entrance.

5. A minimum charged energy and a minimum total energy,

$$E_{ch} = \sum_{i=1}^{N_{ch}} \sqrt{p_i^2 + m_\pi^2} > \frac{1}{8} E_{cm}$$

$$E_{tot} = E_{ch} + \sum_{i=1}^{N_\gamma} E_i > \frac{1}{4} E_{cm}$$

   where N_γ is the number of good neutral tracks.

Table 4.1 shows the photon multiplicity for various photon energy ranges for events satisfying the above requirements. Fig. 4.1 shows the neutral track multiplicity as a function of liquid argon energy. For energetic photons, the photon multiplicity approaches one. In addition to the above requirements we add,

Table 4.1. Neutral track multiplicity in hadronic events (in percent).

# neutrals	0	1	2	3	4	5
$1 < E < 2$	23.7	36.3	24.0	10.8	3.6	1.2
$2 < E < 3$	54.7	37.5	6.9	.8		
$3 < E < 4$	81.0	17.8	1.2			
$4 < E < 5$	91.3	8.5	.2			
$E > 5$	89.4	10.3	.2			

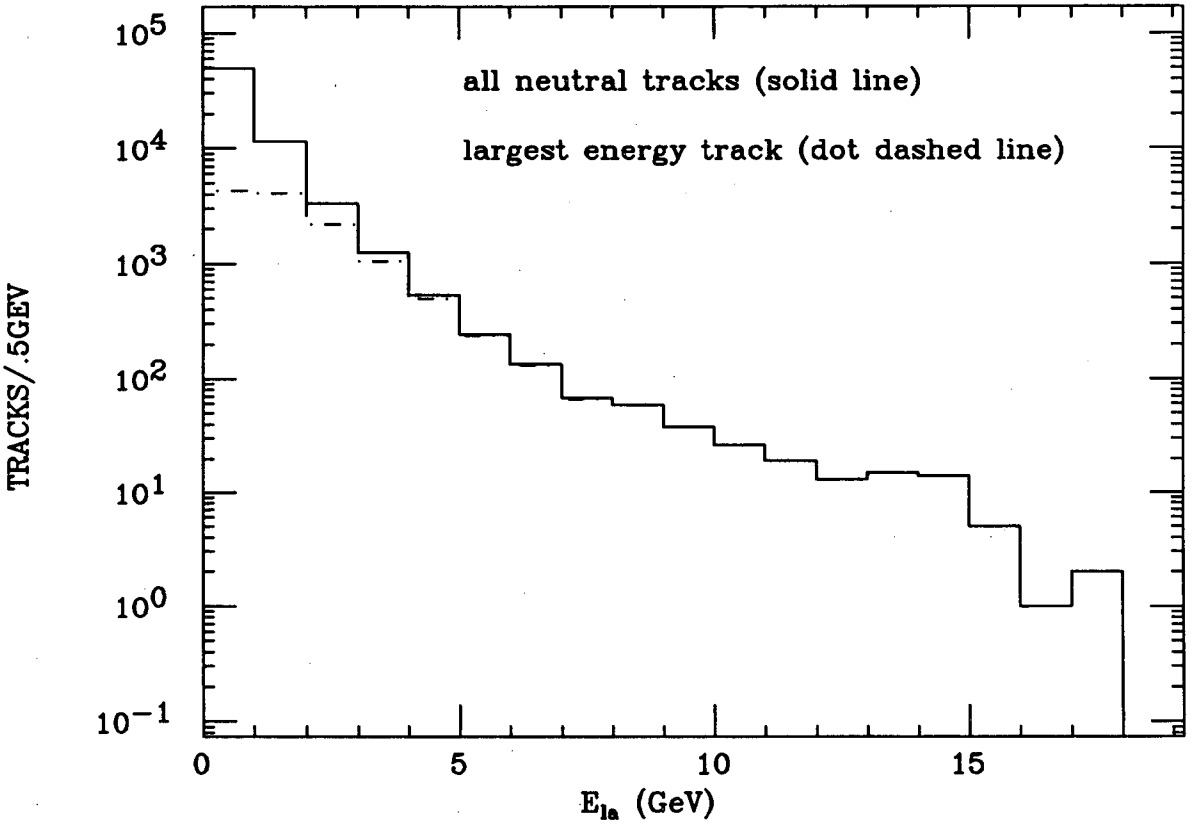

Figure 4.1. Neutral track multiplicity as a function of liquid argon energy. For energies above 5 GeV there is only one energetic neutral track per event.

6. At least one good neutral track must be hard and isolated:

   $E_{la} > 3.0$

   $\theta_{\gamma i} > 20^\circ$, where $\theta_{\gamma i}$ is the angle between the photon's and the ith track's (charged or neutral) momenta.

These requirements select approximately 1% of the hadronic cross section. The hard photon multiplicity is quite small when the 20° isolation cut is included– only .9% of the hard photon events have more then one hard photon. For simplicity, we

will always choose the hard photon as the hardest neutral track in the event. The energy spectrum of hard, isolated photons is shown in Fig. 4.2. Comparison with the $\mu\mu\gamma$ spectrum (Fig. 3.6) suggests that the non-direct background increases rapidly for small E_γ. This suspicion is supported by a Monte Carlo calculation of the non-direct photon background (shown in Fig. 4.2 as a dotted line). For the hadronic simulation we use the LUND generator (LUND version 5.2) [57] that uses a string model to simulate the quark fragmentation into hadrons. Radiative corrections were done for the initial state only according to the prescription of Berends and Kleiss. [54] We can make use of the phenomenon of jets to reduce this background: the direct photons should be at large $p_\perp$ to the jet axes. [2 3 4]

4.2 JET AXES

The determination of jet axes was necessary to increase the ratio of direct to non-direct events and for the measurement of the hadronic charge asymmetry. The method of determining the jet axes was to boost to the hadronic center of mass and then use a sphericity algorithm.

The boost to the hadronic center of mass is determined from the hard photon momentum $\vec{p}_\gamma$,

$$\vec{\beta} = \frac{-\vec{p_\gamma}}{\sqrt{s} - p_\gamma}$$

where $\sqrt{s} = 29$ GeV. To avoid unphysical values of the boost velocity due to measurement error we set $|\vec{\beta}| \leq \beta_{max}$, where β_{max} was calculated from the assumption of five pions with a momentum of at least .1 Gev. The momenta in the event are then boosted to the hadronic center of mass. Charged particles are given the pion mass. In this frame , the sphericity axis $\hat{n}$ is determined by summing over all momenta except the hard photon and minimizing the sphericity S with respect to $\hat{n}$,

$$S = \frac{3}{2}\min_{\hat{n}}\Big(\frac{\sum |\vec{p}_i \times \hat{n}|^2}{\sum p_i^2}\Big).$$

The jet four-momenta are the sum of the momenta along and opposite the sphericity axis. These four-momenta are then boosted to the laboratory system to give the

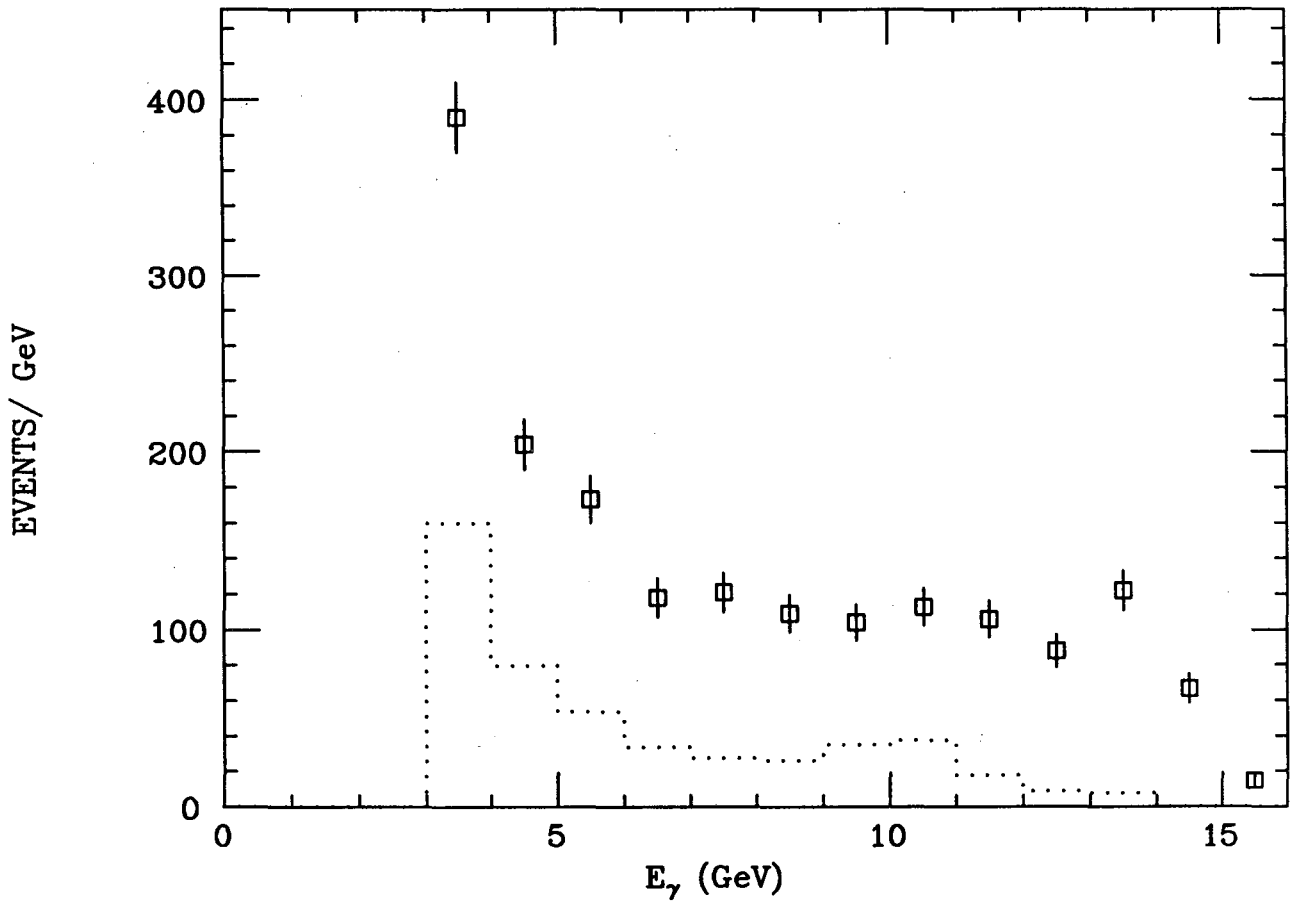

Figure 4.2. Energy of hardest photon for selected hadronic events. Dotted line is non-direct background as calculated with the LUND Monte Carlo with initial state radiation.

jet axes $\hat{J}_1, \hat{J}_2$. The reconstructed jet axes approximate the quark momenta well for Monte Carlo $q\bar{q}\gamma$ events as shown in Fig. 4.3.

The Monte Carlo can be used to estimate the signal (direct) to noise (non-direct) ratio as a function of $p_\perp$, where we define

$$p_\perp \equiv \left| \vec{p}_\gamma - |\vec{p}_\gamma \cdot \hat{J}| \hat{J} \right|.$$

For calculating this quantity the jet axis is chosen that makes $p_\perp$ a minimum. This definition is the usual one for $p_\perp$ if $\vec{p}_\gamma \cdot \hat{J} > 0$, but is different for $\vec{p}_\gamma \cdot \hat{J} < 0$ so that events with very energetic photons will have large values of $p_\perp$. With this definition, $p_\perp$ is in the range $0 < p_\perp < \sqrt{s}$. The ratio of signal to noise increases with increasing $p_\perp$ as shown in Fig. 4.4. We exclude the region of low (less then one) signal to noise ratio by requiring $p_\perp > 2.5$ GeV for the direct photon. The distribution of $p_\perp$ in the data is shown in Fig. 4.5.

4.3 Direct Photon Spectrum

With these criteria we find 1458 direct photon events. Some examples of these events are given in Fig. 4.6, Fig. 4.7, Fig. 4.8, and Fig. 4.9, showing the reconstructed event in the x-y plane. Superimposed (dotted lines) are the calculated jet axes as well as the selected direct photon. A clear " γ + 2 jet " topology is apparent.

The background from $\tau\tau(\gamma)$ is estimated from Monte Carlo to be very small, only .5% or 8 ± 2 events. The LUND Monte carlo with initial state radiation only predicts 1147 events. We therefore see an excess of

$$253 \pm 54 \pm 60 \text{ events},$$

or, expressed as a ratio of measured cross section (σ^{exp}) to that predicted from initial state radiation alone (σ^I) ,

$$\frac{\sigma^{exp}}{\sigma^I} = 1.22 \pm .04 \pm .05.$$

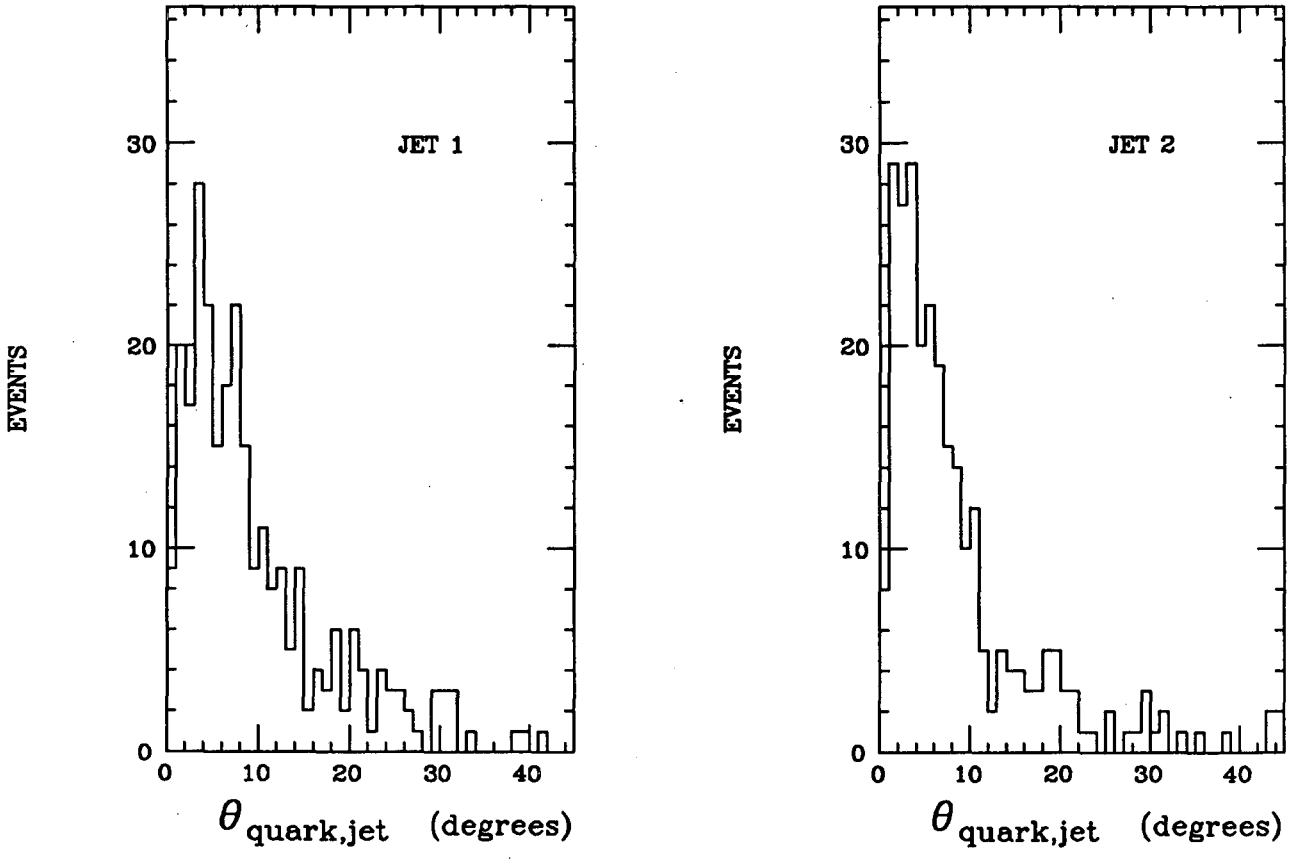

Figure 4.3. The jet axis reconstruction is compared to the produced quark momentum in the Monte Carlo.

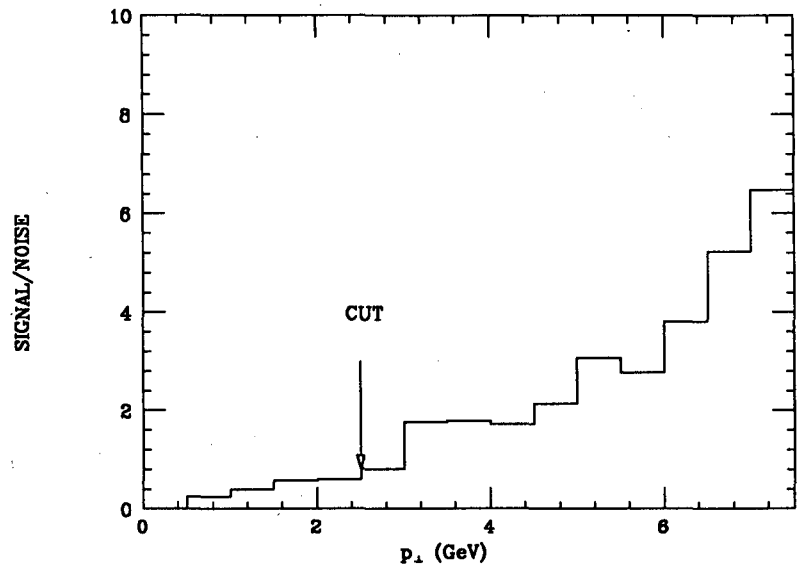

Figure 4.4. The signal (direct) to noise (non-direct) ratio as calculated by the LUND Monte Carlo as a function of $p_\perp$. Events with $p_\perp < 2.5$ GeV are excluded.

In these measurements the first error is the statistical error of the Monte Carlo calculation (39 events or 3%) combined with the statistical error of the measurement (38 events or 3%), and the second error is the 5% systematic uncertainty of the luminosity.

The resulting direct photon energy spectrum is shown in Fig. 4.10 together with the LUND Monte Carlo prediction (solid histogram) with initial state radiation only, normalized to the luminosity. The solid histogram indicates the non-direct background calculated with the Monte Carlo (the solid histogram includes this background). Comparison with Fig. 1.4 suggests that the excess of events for small E_γ is evidence for a final state radiation amplitude.

4.4 Charge Asymmetry

Further evidence for a final state radiation amplitude can be found by measuring a charge asymmetry. Just as for the $\mu\mu\gamma$ process we define the charge

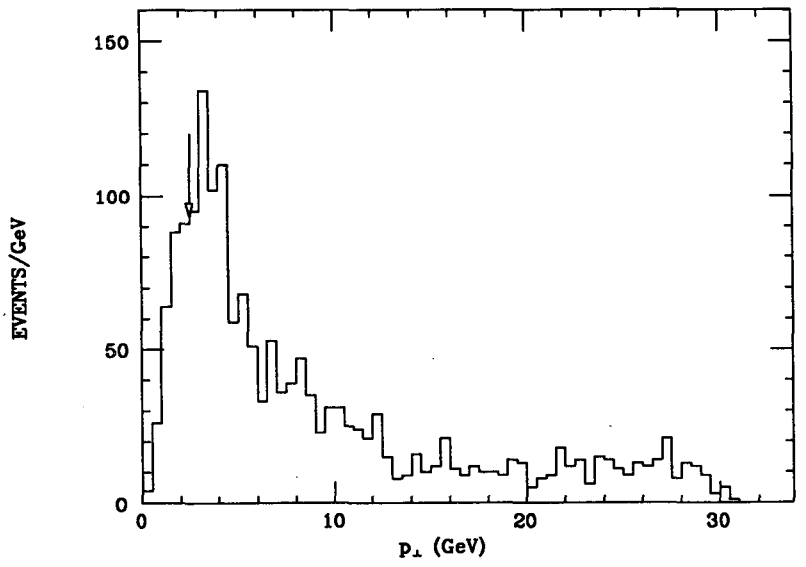

Figure 4.5. The $p_\perp$ distribution in the data. Events with $p_\perp < 2.5$ GeV are excluded.

asymmetry,

$$A = \frac{N_f - N_b}{N_f + N_b},$$

where $N_f(N_b)$ is the number of jets with $Q_J \cos\theta_J > 0$ ($Q_J \cos\theta_J < 0$), θ_J is the angle between the jet momentum and the positron beam, and Q_J is the jet charge assignment. The jet charge is assigned according to the sum of the charges in the jet,

$$Q_J = \mathrm{sgn}\Big(\sum_i \mathrm{q_i}\Big) \tag{4.1}$$

where the sign function has the values $+1, -1, 0$ depending on whether its argument is positive, negative or zero. To avoid the assignment of zero, if the sum is zero then the charge of the particle with the smallest fraction of the jet momentum in the hadronic center of mass is deleted from the sum 4.1 .

To enhance the asymmetry effect we make three additional requirements. First, we require that both jets be in opposite hemispheres. About one-third of the events fail this requirement. Second, since the asymmetry is small for large E_γ (see table

RUN 6516 REC 7860 E= 29.00 10 PRONG PLUS HADRON (5-4)
TRIGGER 08F C MARK II - PEP

TRK	P	ELATOT	ID
1	0.6		PI-
2	0.3	0.3	PI+
3	0.5	0.1	PI+
4	0.3	0.1	PI-
5	1.4		MU+
6	1.0	0.1	PI+
7	0.7	0.1	PI-
8	1.5		PI-
9	3.2	0.2	PI+
10	0.5	0.3	PI-
11	1.0	0.1	PI+
12	0.1		PI-
13	0.2	0.5	PI-
14	2.3		PI-
15	0.2		PI+
16		0.3	G
17		0.5	G
18		0.3	G
19		0.6	G
20		0.6	G
21		0.1	G
22		0.2	G
23		0.3	G
24		0.1	G
25		0.2	G
26		0.5	G
27		4.7	G
28		0.5	G
29		0.4	G
30		0.2	G
31		0.0	G

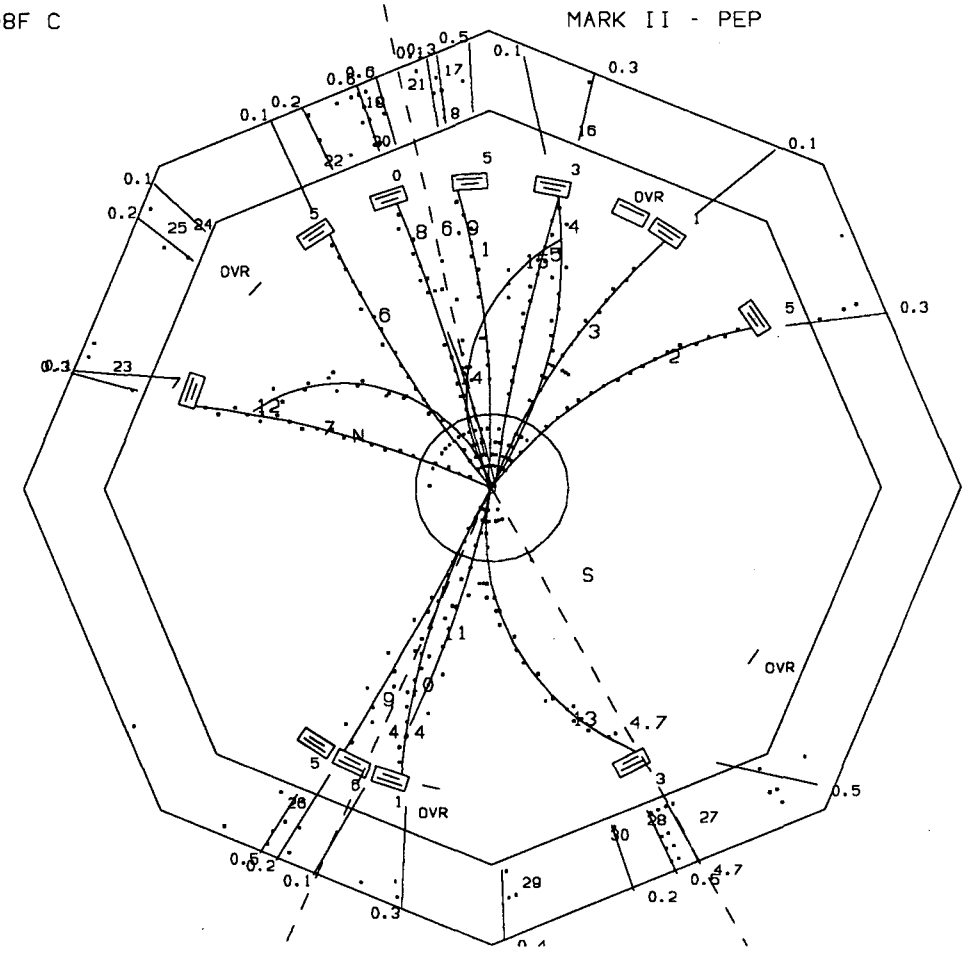

Figure 4.6. Mark II event plot showing " γ + 2 jet " topology. Superimposed (dotted lines) are the reconstructed jet axes and the selected direct photon.

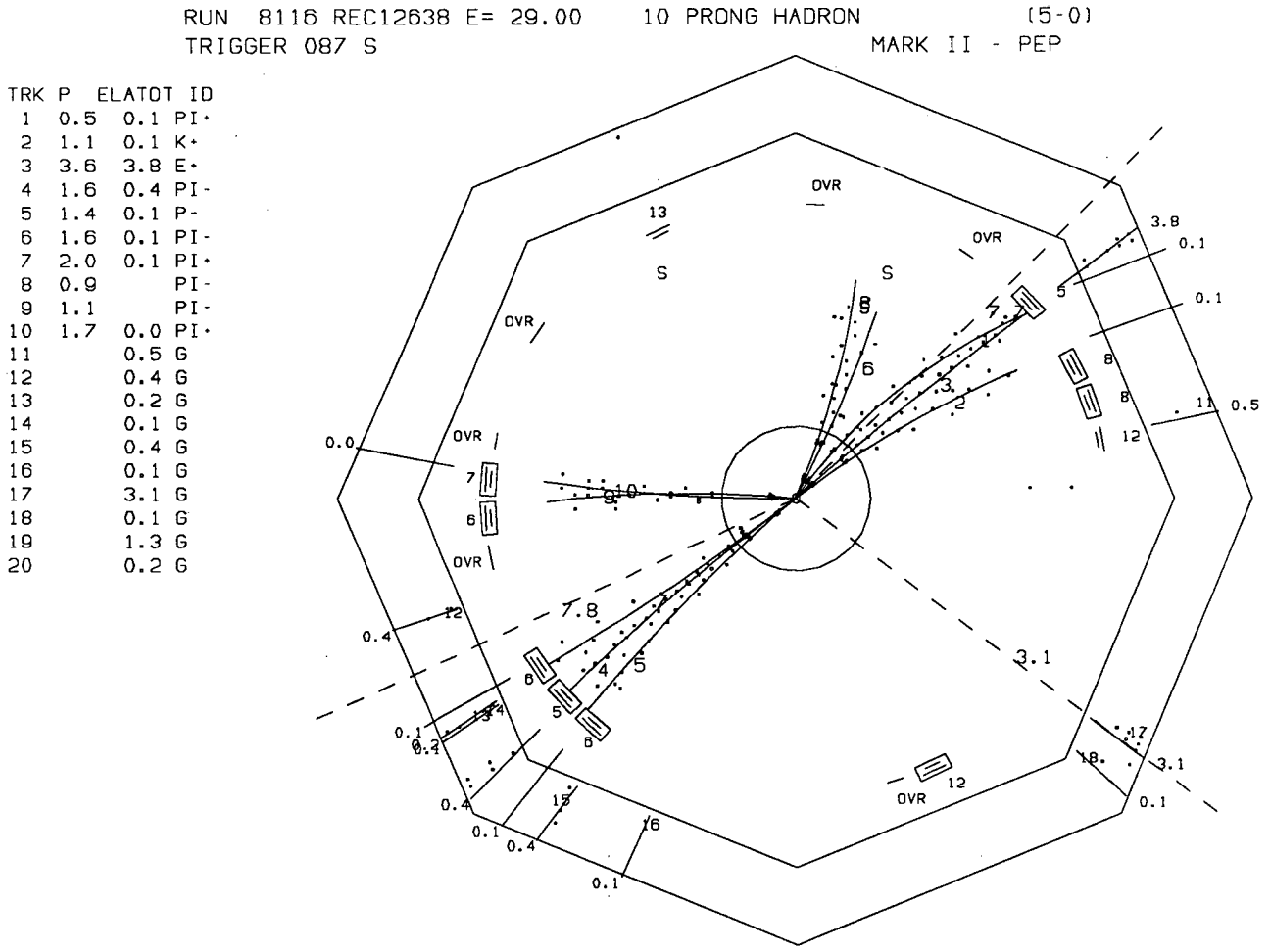

Figure 4.7. Mark II event plot showing " γ + 2 jet " topology. Superimposed (dotted lines) are the reconstructed jet axes and the selected direct photon.

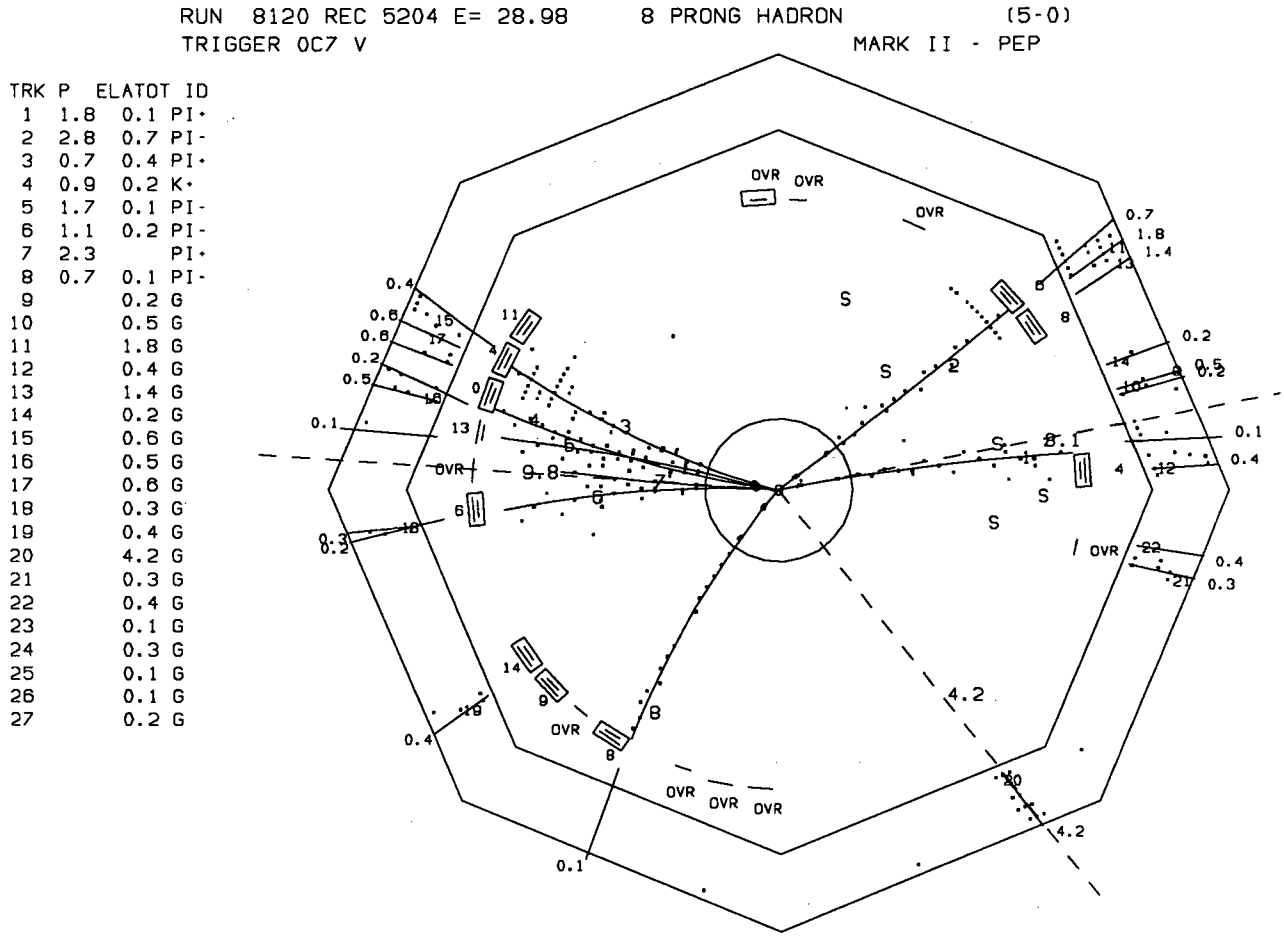

Figure 4.8. Mark II event plot showing " γ + 2 jet " topology. Superimposed (dotted lines) are the reconstructed jet axes and the selected direct photon.

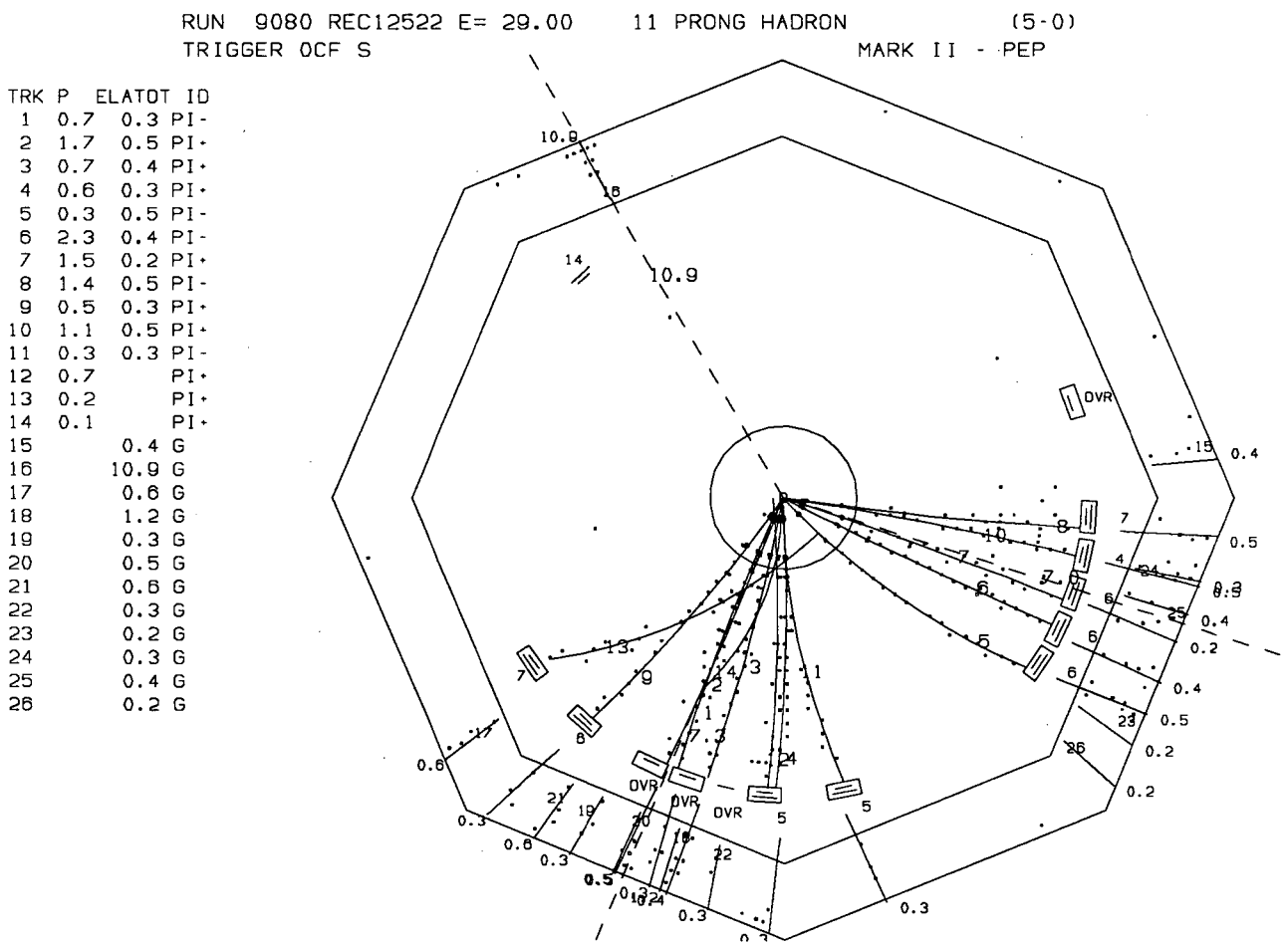

Figure 4.9. Mark II event plot showing " γ + 2 jet " topology. Superimposed (dotted lines) are the reconstructed jet axes and the selected direct photon.

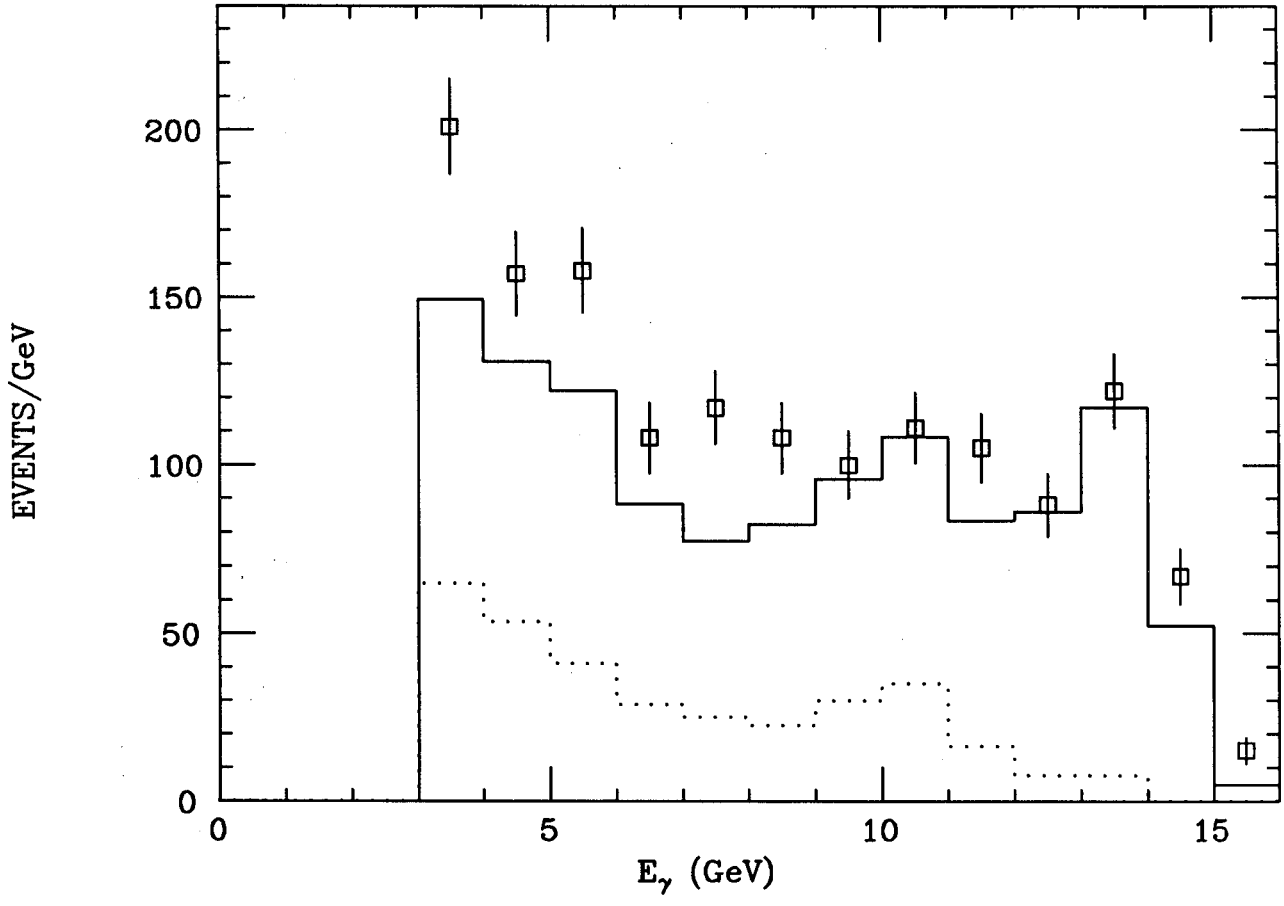

Figure 4.10. The direct photon energy spectrum. Data (points) show a small excess over the LUND Monte Carlo with initial state radiation only (solid histogram). This excess is for small E_γ as expected for final state radiation. The dotted histogram is the calculated non-direct background (the solid histogram includes this background).

3.4) we require that $E_\gamma < 7.25$ GeV. This reduces the sample by about a factor of two. Finally, we require that the charges Q_{J_1}, Q_{J_2} be opposite in sign. This requirement reduces the sample again by a about 60 % leaving 311 events. The quantity $Q_J \cos\theta_J$ is plotted for these events in Fig. 4.11. A strong asymmetry is apparent in the distribution. We find,

$$A_{exp} = -(24.6 \pm 5.5)\%$$

where the error is statistical only. The LUND Monte Carlo with initial state radiation only (dotted histogram) gives a result consistent with zero,

$$A_I = -(4.8 \pm 6.6)\%$$

the error being the statistical error of the calculation.

As a further check, we consider events that satisfy our event selection for direct photons except that instead of selecting events with a hard, isolated neutral track we look for similar events with a hard, isolated charged track. The energy spectrum of these hard, isolated charged tracks is shown in Fig. 4.12. For this analysis, only the first 141 pb^{-1} was used. These events are then subjected to the identical cuts and charge assignment algorithm as described above for the charge asymmetry measurement in the data. The quantity $Q_J \cos\theta_J$ for these events is shown in Fig. 4.13. We find for the asymmetry in these events a result consistent with zero,

$$A_{\pi\pm} = (-0.5 \pm 3.0\ )\%.$$

This provides a Monte Carlo independent check of possible systematic errors in our asymmetry measurement.

4.5 Monte Carlo

We can use the Monte Carlo generator for $\mu\mu\gamma$ of Berends, Kleiss, and Jadach (BKJ) as the basis for a hadronic Monte Carlo generator that includes both initial

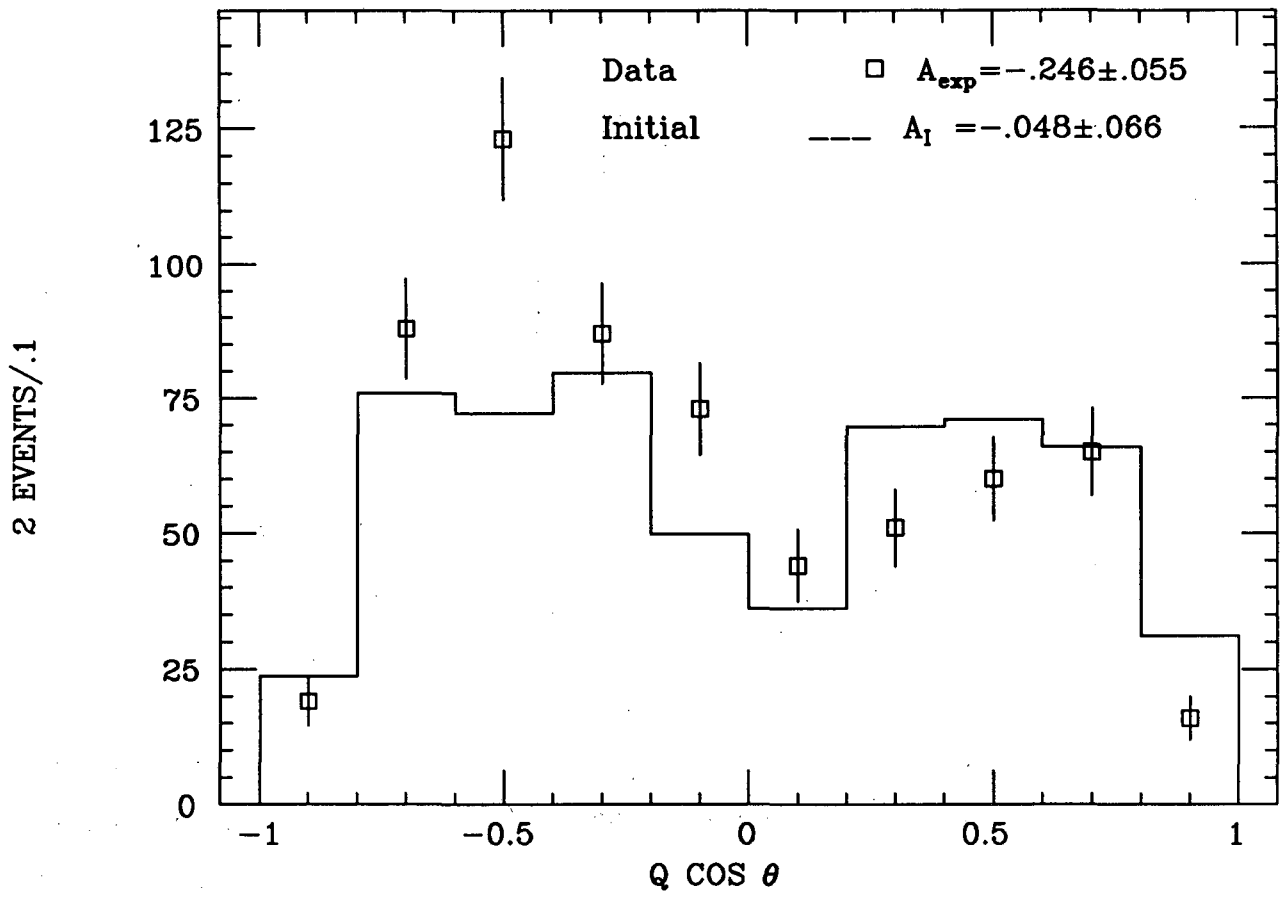

Figure 4.11. The distribution $Q_J \cos\theta_J$ for hard photon events (points) with cuts chosen to enhance the asymmetry effect. The charge is assigned according to the sum of the charges in the jet. The solid histogram is the LUND Monte Carlo with initial state radiation only.

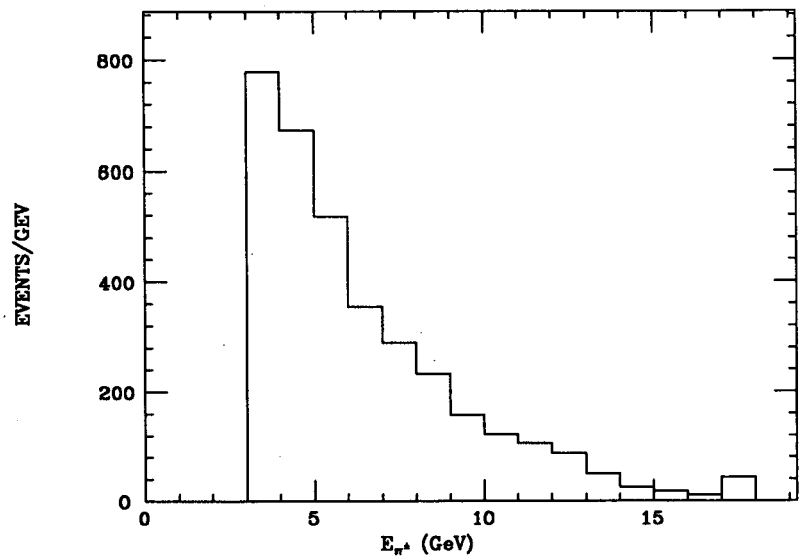

Figure 4.12. The energy spectrum from hard, isolated charged tracks that are used to check for a systematic error in the charge asymmetry measurement.

and final state radiation by a suitable change of the final state fermion couplings. [47] Once generated, the $q\bar{q}$ pair can be fragmented according to the LUND (LUND version 6.1) fragmentation scheme.

The implementation of this proceedure is outlined in the flowchart (see Fig. 4.14). First the flavor is chosen to allow the setting up of the $q\bar{q}(\gamma)$ generator appropriately. The $q\bar{q}(\gamma)$ final state is then generated according to $O(\alpha^3)$ QED (including electroweak corrections). The event is then tested to see if the mass of the $q\bar{q}$ pair is sufficient for fragmentation to a hadronic final state. The fragmentation is then done according to the LUND fragmentation scheme for a $q\bar{q}$ pair. Finally, to speed up the generation process, only those events with a hard photon ($E_\gamma > .5$ GeV , $|\cos\theta_\gamma| < .9$) were passed through the detector simulation. These events ($q\bar{q}\gamma$) were only 6.3% of the total events ($q\bar{q}(\gamma)$). A sample corresponding to about 157 pb^{-1} was generated. The flavors u,d,s,c,b were generated in the ratios 1 : .20 : .16 : .91 : .15.

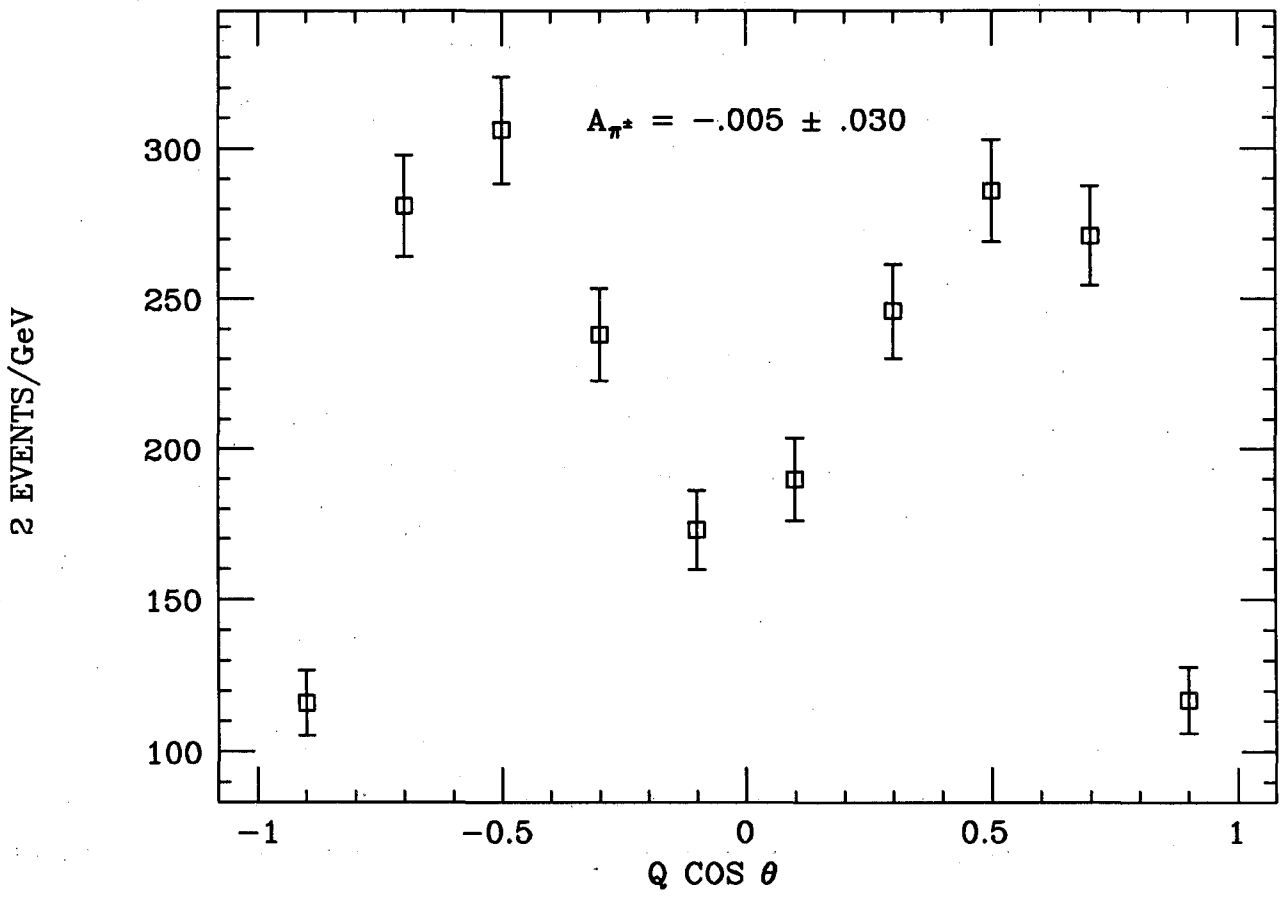

Figure 4.13. The charge asymmetry in events where a hard, isolated charged track fakes the 2 jet + γ topology. The asymmetry is consistent with zero, providing a check of systemmatic errors.

The major shortcoming of this scheme is that it ignores gluon effects. The LUND Monte Carlo generates hadrons according to the matrix elements for $q\bar{q}$, $q\bar{q}G$, and $q\bar{q}GG$ with the probabilities .2, .72, and .08 respectively . Since a method for incorporating these effects was not known, the $q\bar{q}$ approximation was made. This approximation tends to generate thinner jets.

The generated direct photon events are then mixed with the appropriate non-direct background (using LUND with initial state radiation only). The result for the direct photon energy spectrum is shown in Fig. 4.15. We see that the agreement is excellent, filling in the missing number of events in the soft photon region just as expected. We find a prediction of 1132 ± 41 direct and 319 ± 20 non-direct events. Adding in the 8 τ background events we expect 1457 ± 45 events or,

$$\frac{\sigma^{exp}}{\sigma^{I+F}} = 1.00 \pm .04 \pm .05.$$

To study the jet charge assignments and to search for an optimal assignment strategy, we considered the quantity suggested by Field and Feynman, [58]

$$Q_J(\alpha) = \mathrm{sgn}\Big(\sum_i q_i x_i^{\alpha}\Big) \tag{4.2}$$

where x_i is the fraction of momentum carried by the ith particle in the jet in the hadronic center of mass. Again, the particle with the smallest x_i was deleted from the sum if necessary to insure a non-zero result. This charge function has the nice property that in the limit $\alpha \to 0$ it agrees with our previous definition (summed charge), and in the limit of large α it approaches the assignment according to the charge of the particle with greatest fractional momentum (leading charge). Using the generated Monte Carlo, we calculated the probability $P(\alpha)$ that the assigned charge agrees with the sign of the charge of the produced quark.

Another quantity which may be used to study the charge assignment $Q_J(\alpha)$ is the charge correlation function $w(\alpha)$ defined by,

$$(2w-1)^2 = -\langle Q_{J_1} Q_{J_2} \rangle \tag{4.3}$$

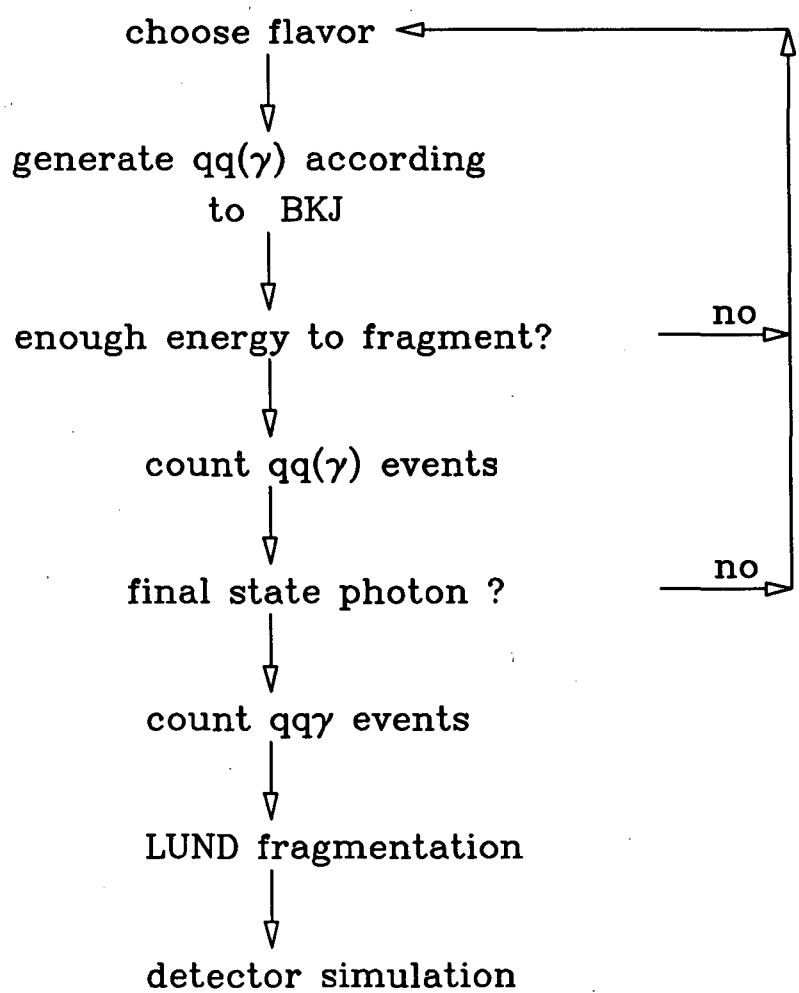

Figure 4.14. Flowchart for construction of Monte Carlo incorporating final state radiation.

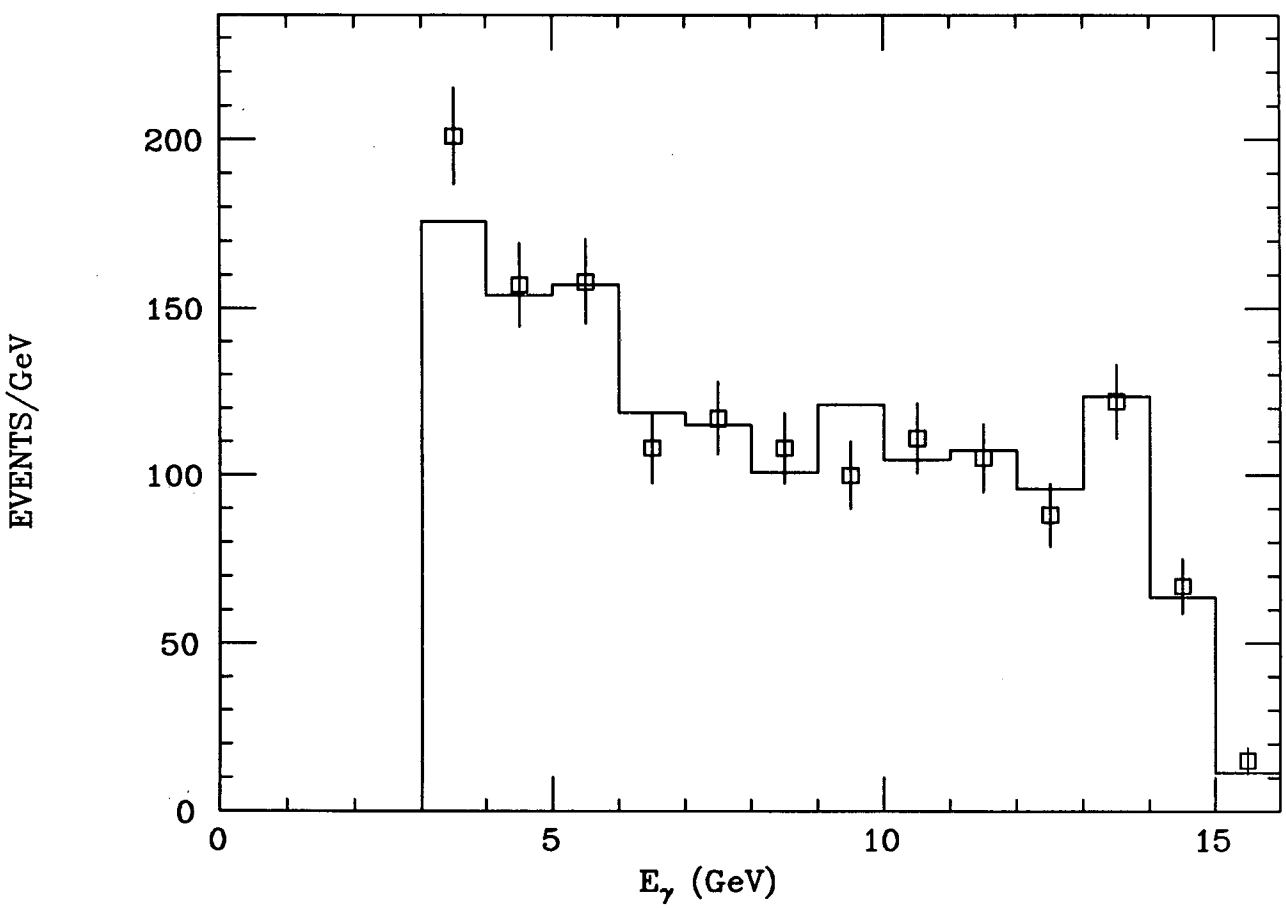

Figure 4.15. The direct photon energy spectrum in the data (points) together with the LUND Monte Carlo including final state radiation (solid histogram).

where $\langle Q_{J_1} Q_{J_2} \rangle$ is the average over events of the product of the assignments for each jet in an event. This function has the following interpretation: if the jet charge assignments are uncorrelated, then w is the probability of the charge assignments being correct. Consider the average product of charge assignments,

$$\langle Q_{J_1} Q_{J_2} \rangle = \frac{1}{N_{evts}} \sum_i^{Nevts} Q^i_{J_1} Q^i_{J_2} = \frac{N_+ - N_-}{N_+ + N_-}$$

where $N_\pm$ is the number of events with assignments of the same (opposite) sign. Then if the assignments Q_{J_1}, Q_{J_2} are uncorrelated, $N_\pm$ can be used to estimate w, the probability for assigning the correct charge:

$$\frac{N_+}{N_+ + N_-} = 2w(1-w)$$

$$\frac{N_-}{N_+ + N_-} = w^2 + (1-w)^2$$

Subtracting, we obtain the result 4.3 . For correlated assignments, w loses this simple interpretation. For the summed charge the assignments Q_{J_1}, Q_{J_2} are highly correlated due to charge conservation. We expect that $w > P$ for small α but that $w \sim P$ for large α and that they are equal in the limit of leading charge assignments. The function w is useful because it may be studied in the data as well as in the Monte Carlo.

The behavior of the functions w and P is shown in Fig. 4.16 for events satisfying all the requirements except the final requirement of opposite jet charges. Also plotted are P and w for the leading assignments. We note that for the leading assignments the Monte Carlo shows that $P = w$. Evidence for a small enhancement of the charge assignment probability P for small α ($\alpha \sim .3$). However this enahancement is much smaller then the statistical error (indicated by the error bars on the right). In general, P and w decrease with increasing α. For simplicity we shall stick with our original definition. With this definition ($\alpha = 0$) we find $P = .73 \pm .04$.

For events with the additional requirement that the jets have opposite charge, we find $P = .86 \pm .04$.

The distribution of the quantity $Q_J \cos\theta_J$ is shown in Fig. 4.17. for all direct photon events (A), and then for events satisfying the requirements chosen previously to enhance the asymmetry effect: the jets are in opposite hemispheres (B), the photon energy is less then half the beam energy (C), and the charge assignments are opposite in sign (D). We see that the Monte Carlo including final state radiation reproduces the behavior of the asymmetry quite well. The final asymmetry distribution, 4.17 (D), is reproduced in Fig. 4.18 together with the produced $q\bar{q}\gamma$ distribution. The asymmetry of the produced distribution with these requirements is quite large,

$$A_{q\bar{q}\gamma} = -(41.6 \pm 5.2)\%.$$

After the events are fragmented, passed through the detector simulation, and analyized we find that the inclusion of final state radiation reproduces the asymmentry in the data,

$$A_{exp} = -(24.6 \pm 5.5)\%$$

$$A_{I+F} = -(23.1 \pm 6.0)\%.$$

Finally, we study the asymmetry as a function of the charge assignment parameter (α) in Fig. 4.19. Again we see evidence for a slight enhancement at $\alpha \sim .3$.

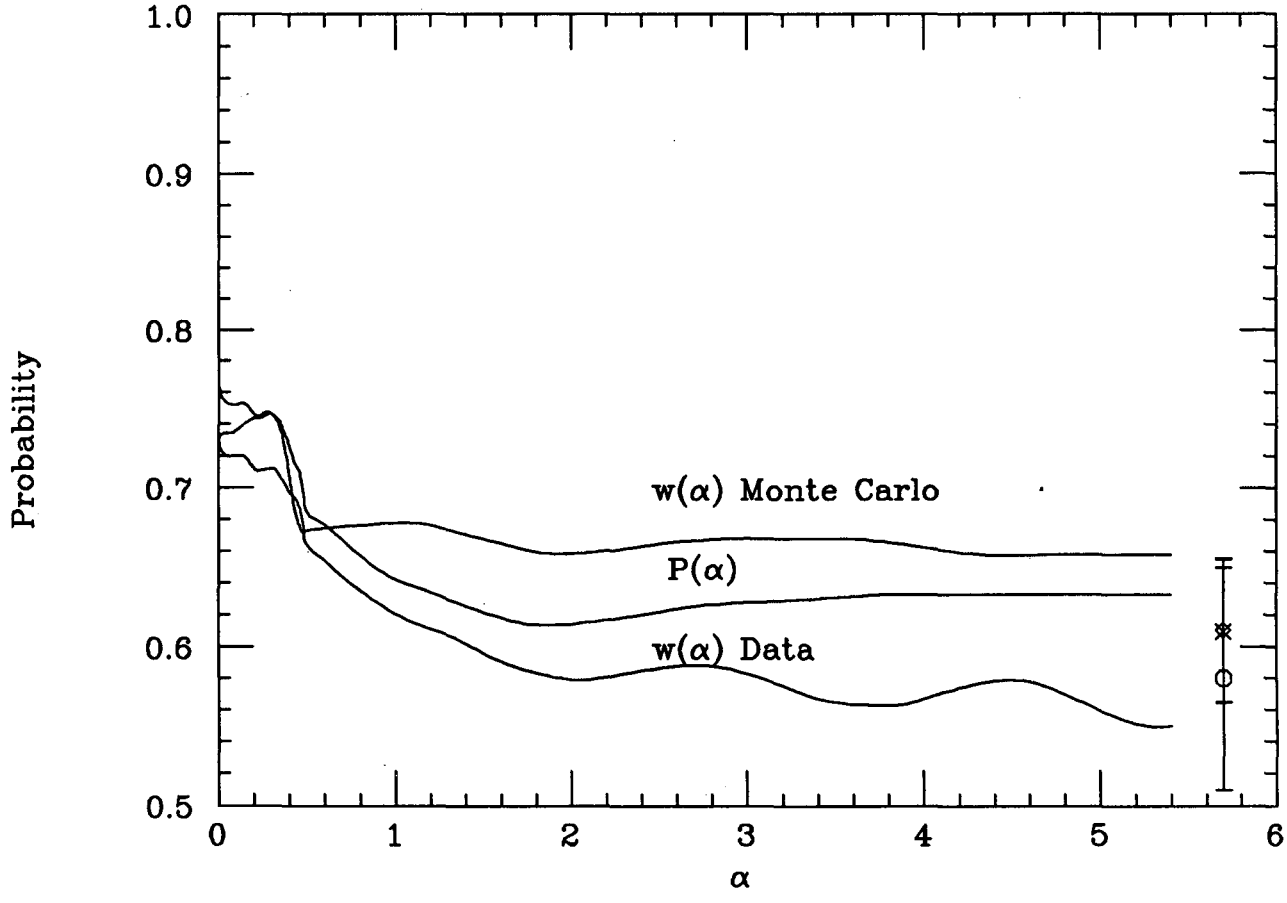

Figure 4.16. The charge assignment probability P as calculated with the Monte Carlo along with the charge correlation w as functions of the power for fractional momentum weighting α used to calculate the jet charges. The points on the far right are calculated with leading charges: P calculated in the Monte Carlo $\times$, and w in the Monte Carlo $\diamond$ and data $\circ$.

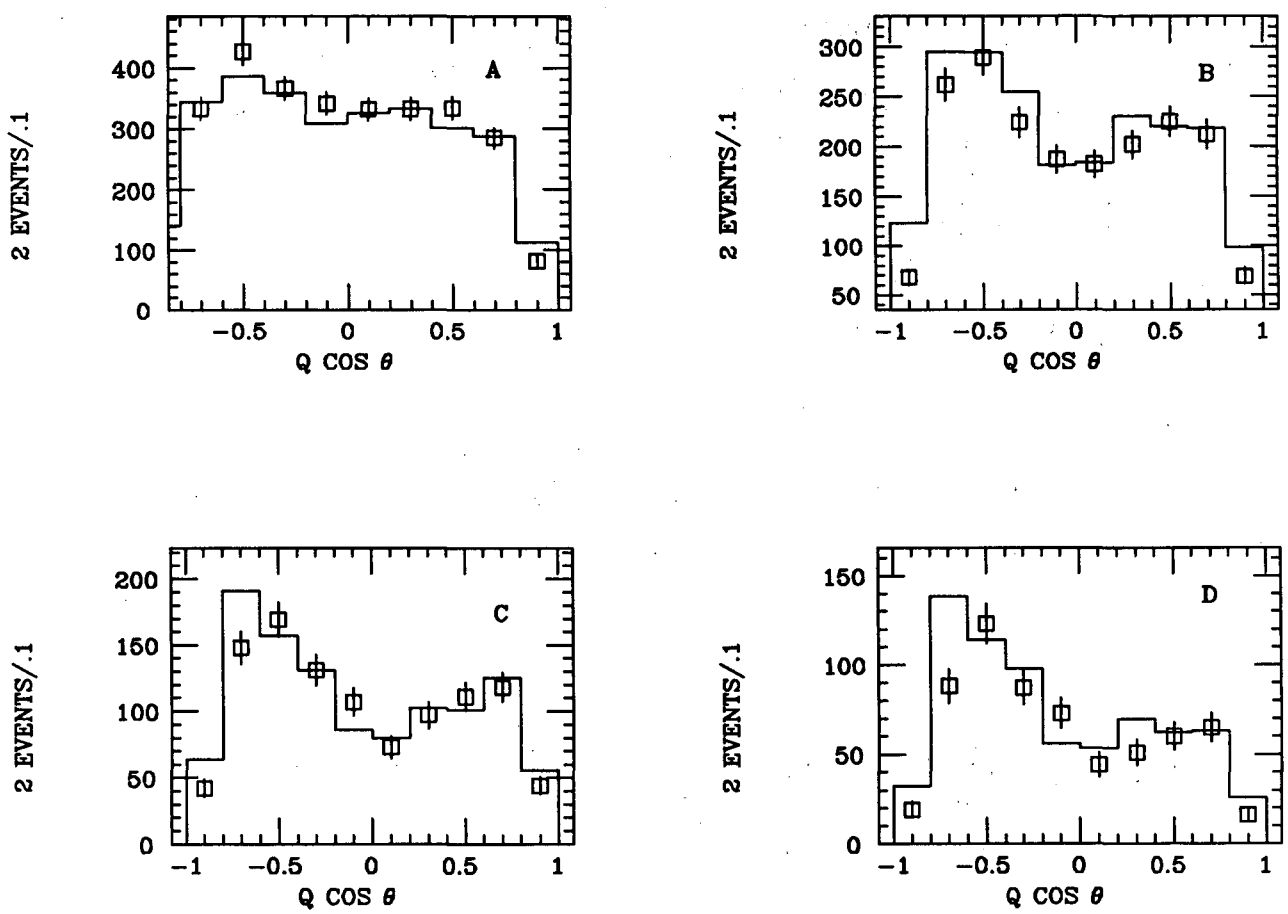

Figure 4.17. The distribution $Q_J \cos\theta_J$ for the LUND Monte Carlo with initial and final state radiation (solid histogram) and the data (points) for all direct photon events (A), and for events satisfying the additional requirement that the jets be in opposite hemispheres (B), and also having $E_\gamma < 7.25$ GeV (C), and finally the additional requirement that the charge assignments be opposite in sign (D).

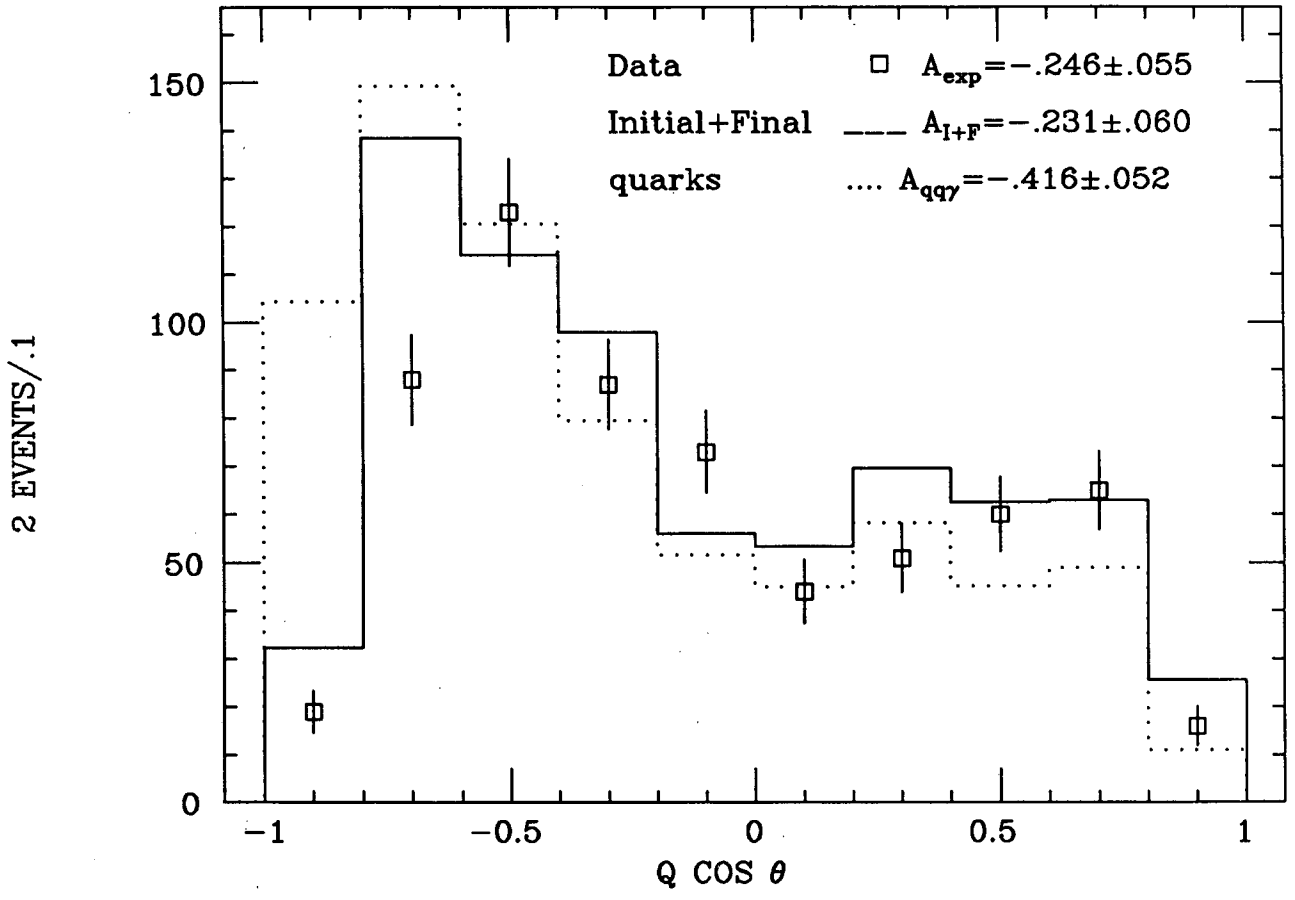

Figure 4.18. The distribution $Q_J \cos\theta_J$ for the LUND Monte Carlo with initial and final state radiation (solid histogram). Also plotted are the produced $q\bar{q}\gamma$ asymmetry (dotted histogram), and the data (points).

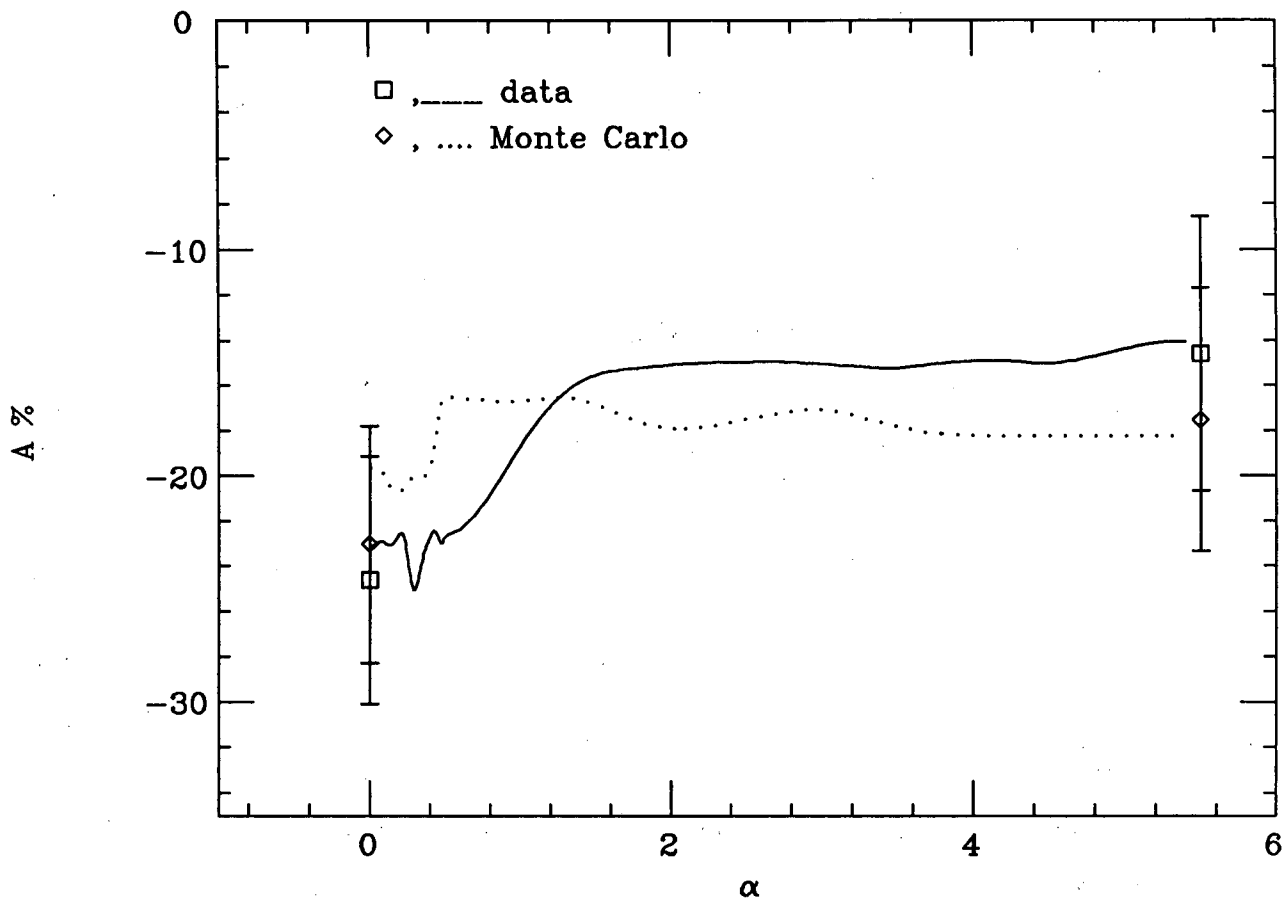

Figure 4.19. The asymmetry A as a function of the charge assignment parameter α . Also shown (points) are the limits of summed (left) and leading (right) assignments.

5. Conclusion

We have studied hard photon processes in e^+e^- annihilation. In the $\mu\mu\gamma$ process a small number of non-planar events are observed. The precise angular resolution of the detector was exploited to measure the missing energy in these events, and this energy spectrum was found to be consistent with that expected from higher order initial state radiation. The observed cross section is consisent with the predicted cross section for this process,

$$\frac{\sigma^{exp}}{\sigma^{th}} = .90 \pm .05 \pm .06.$$

The observed hard photon energy E_γ and the masses $M_{\mu\mu}$, $M_{\mu\gamma}$ are precisely measured by the angle measurements alone. The resulting distributions are in good agreement with the $O(\alpha^3)$ prediction. The measured charge asymmetry is in good agreement with the predicted value,

$$\frac{A_{exp}}{A_{th}} = .83 \pm .25 \pm .12.$$

The $\mu\gamma$ invariant mass distribution is used to place a limit on a possible excited muon coupling of (G_γ/M^*). For excited muon masses in the range $1 < M^* < 21$ GeV we place a limit of $(G_\gamma/M^*)^2 < 10^{-5}$ GeV^{-2} at a 95% confidence level.

In the $ee \rightarrow$ hadrons $+ \gamma$ process we have searched for evidence of a final state radiation amplitude. Evidence for final state radiation is found in an excess of events over that expected from initial state radiation alone of $253 \pm 54 \pm 60$ events. Further evidence for final state radiation is found in a large hadronic charge asymmetry,

$$A_{\mathrm{had}+\gamma} = -(24.6 \pm 5.5)\%.$$

Appendix A. Charge Asymmetry

In hard photon events the forward-backward charge asymmetry is a consequence of charge parity invariance in QED. That the asymmetry results from the interference of initial and final state amplitudes of opposite C-parity was first noticed by Putzolu who gave essentially the following argument. [8]

Consider the process $ee \to f\bar{f}\gamma$ where f is a fermion different from the electron that couples in the same way to the electromagnetic field. The initial $|ee\rangle$ state in an e^+e^- colliding beam experiment is clearly not an eigenstate of C-parity. It may however be written as the sum of such eigenstates since $C^2|ee\rangle = |ee\rangle$. We therefore have,

$$|ee\rangle = \frac{1}{2}[|ee\rangle + C|ee\rangle] + \frac{1}{2}[|ee\rangle - C|ee\rangle]$$
$$= |(ee)_+\rangle + |(ee)_-\rangle$$

where, $C|(ee)_\pm\rangle = \pm|(ee)_\pm\rangle$.

The process $ee \to f\bar{f}\gamma$ is to lowest order the sum of initial and final state radiation amplitudes. Since the interaction is C invariant the initial state amplitude creates $f\bar{f}$ in a C- state , and the final state amplitude creates $f\bar{f}$ in a C+ state. Intuitively, this follows from the Feynman diagrams for these amplitudes and recalling that the photon is a C- state . Since the initial state amplitude has two photons in the intermediate state and the final state amplitude only one, the result follows. To see this more explicitly we can write the Feynman diagrams in position space (see Fig. A.1) . Writing the electron charge as e and the fermion charge as f,

$$\langle f\bar{f}\gamma|S|ee\rangle = \langle f\bar{f}\gamma|S_I|ee\rangle + \langle f\bar{f}\gamma|S_F|ee\rangle$$

$$\langle f\bar{f}\gamma|S_I|ee\rangle = (-ie)^2(-if)\int dxdydz\langle f\bar{f}|J_f(z)|0\rangle iD_F(z,y)$$
$$\times\langle\gamma|A(x)|0\rangle\langle 0|T(J_e(y)J_e(x))|ee\rangle$$
$$\langle f\bar{f}\gamma|S_F|ee\rangle = (-ie)(-if)^2\int dxdydz\langle f\bar{f}|T(J_f(z)J_f(y))|0\rangle$$
$$\times\langle\gamma|A(z)|0\rangle iD_F(y,x)\langle 0|J_e(x)|ee\rangle$$

Then since CJC^{-1}=-J,

$$\langle 0|J_e|(ee)_+\rangle = \langle 0|C^{-1}CJ_eC^{-1}C|(ee)_+\rangle$$

$$= -\langle 0|J_e|(ee)_+\rangle = 0.$$

Similarly,

$$\langle 0|T(J_eJ_e)|(ee)_-\rangle = \langle (f\bar{f})_+|J_f|0\rangle = \langle (f\bar{f})_-|T(J_fJ_f)|0\rangle = 0$$

Thus we have,

$$\langle f\bar{f}\gamma|S|ee\rangle = \langle (f\bar{f})_-\gamma|S_I|(ee)_+\rangle + \langle (f\bar{f})_+\gamma|S_F|(ee)_-\rangle$$

The asymmetry is proportional to the difference,

$$A \propto |\langle f\bar{f}\gamma|S|ee\rangle|^2 - |\langle f\bar{f}\gamma|C^{-1}S|ee\rangle|^2$$

where

$$|\langle f\bar{f}\gamma|S|ee\rangle|^2 = |S_I|^2 + |S_F|^2$$

$$+2Re\{\langle (f\bar{f})_+\gamma|S_F|(ee)_-\rangle\langle (ee)_+|S_I|(f\bar{f})_-\gamma\rangle\}.$$

For $|\langle f\bar{f}\gamma|C^{-1}S|ee\rangle|^2$ clearly only the interference term will change sign. It follows that

$$A \propto 2\Re\{S_IS_F^*\}$$

It is also seen that any charge symmetric distribution such as the photon energy spectrum will be independent of the interference term.

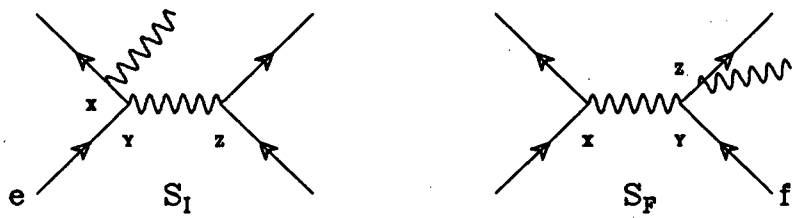

Figure A.1. Lowest order Feynman diagrams in position space for the initial state amplitude (S_I) and the final state amplitude (S_F) for the process $ee \rightarrow f\bar{f}\gamma$ where the final state fermion is different from the electron.

Appendix B. Estimate of $\pi\pi\gamma$ background

The process $ee \to \pi\pi\gamma$ can be calculated from the initial state radiation formula,

$$\frac{d\sigma}{dk} = \frac{\alpha}{\pi}\frac{1}{k}[\log(\frac{s}{m_e^2}) - 1][1 + (\frac{s'}{s})^2]\sigma_{\pi\pi}(s')$$

The cross section $\sigma_{\pi\pi}(s)$ is significant only in the neighborhood of the ρ mass where in the vector dominence model it is given by the Breit-Wigner formula,

$$\sigma_{\pi\pi}(s) = \frac{12\pi}{s}\frac{m^2\Gamma\Gamma_{ee}}{(s-m^2)^2 + \Gamma^2 m^2}$$

where m is the mass of the ρ, Γ is the total width, and Γ_{ee} is the partial width to e^+e^-. The cross section for $e^+e^- \to \pi\pi\gamma$ is then obtained by performing the integral,

$$\sigma_{\pi\pi\gamma} = \int_{k_{min}}^{k_{max}} (\frac{d\sigma_{\pi\pi}}{dk})dk$$

$$k_{max} = \frac{\sqrt{s}}{2}(1 - \frac{4m_\pi^2}{s}).$$

Since $m\Gamma \ll s$ we may approximate the Breit-Wigner by a delta function,

$$\lim_{m\Gamma\to 0}\sigma_{\pi\pi}(s) = \frac{12\pi}{m}\Gamma_{ee}\lim_{m\Gamma\to 0}\left\{\frac{m\Gamma}{(s-m^2)^2 + (m\Gamma)^2}\right\}$$

$$= \frac{12\pi}{m}\Gamma_{ee}\{\pi\delta(s-m^2)\}$$

$$= m\Gamma\sigma_{\pi\pi}(m^2)\pi\delta(s-m^2)$$

For $s' = s(1 - k/E)$ where $E = \sqrt(s)/2$ we have,

$$\sigma_{\pi\pi}(s') = m\Gamma\sigma_{\pi\pi}(m^2)\pi\delta(s'-m^2)$$

$$= \frac{\pi}{4}\sigma_{\pi\pi}(m^2)\Gamma(\frac{m}{E})\delta(k-E).$$

The cross section is then,

$$\sigma_{\pi\pi\gamma} = \frac{\alpha}{4}[\log(\frac{s}{m^2}) - 1]\sigma_{\pi\pi}(m^2)\Gamma\frac{m\Gamma}{E^2}.$$

With $\Gamma = .15$ GeV^{-1}, $m = .77$ GeV , $E = 14.5$ GeV, and $\sigma_{\pi\pi}(m^2) = 1.24\ \mu b$ we have the result,

$$\sigma_{\pi\pi\gamma} \approx 26\ pb.$$

The angular distribution of $ee \rightarrow \pi\pi\gamma$ will be that of $ee \rightarrow \gamma\gamma$ and will be highly peaked along the beam direction. From the differential cross section for $\gamma\gamma$,

$$\sigma_{\gamma\gamma}(x) = \int_{-x}^{x} \frac{d\sigma_{\gamma\gamma}}{d\cos\theta} d\cos\theta$$

$$= \frac{2\pi\alpha^2}{s}[\log(\frac{1+\beta x}{1-\beta x}) - x]$$

The ratio $\sigma_{\gamma\gamma}(.65)/\sigma_{\gamma\gamma}(1)$ is about .03 so the cross section for our acceptance is then,

$$\sigma_{\pi\pi\gamma}(.65) \approx .8\ pb.$$

We thus obtain an estimate of the number of expected $\pi\pi\gamma$ events when the mass of the $\pi\pi$ system is $\sim m$,

$$N_{exp} \approx \sigma_{\pi\pi\gamma}(.65) A_\phi \mathcal{L} \approx 145 \text{ events},$$

where a factor $A_\phi = .8$ has been included for the acceptance in ϕ. The number of $\mu\mu\gamma$ events in this region predicted from the Monte Carlo is 47, giving a total of 192 expected events. Using the muon chambers to study tagged $\mu\mu\gamma$ events, we estimate the efficiency due to triggering and tracking to be low in this kinematic region– $\epsilon \approx .47 \pm .16$. We observe 64 events, a number compatible with the prediction given the poor efficiency.

Appendix C. Statistical error on asymmetry

The quanitity A is a multinomial distribution where each event has one of four outcomes,

$N_+ = \#$ events with $\cos\theta_+ > 0$ and $\cos\theta_- < 0$.

$N_- = \#$ events with $\cos\theta_+ < 0$ and $\cos\theta_- > 0$.

$N_\mp = \#$ events with $\cos\theta_+ < 0$ and $\cos\theta_- < 0$.

$N_\pm = \#$ events with $\cos\theta_+ > 0$ and $\cos\theta_- > 0$.

where $\theta_\pm$ are the angles the $\mu_\pm$ make with respect to the positron beam. Writing $N = N_+ + N_- + N_\pm + N_\mp$ we then have

$$A = \frac{N_+ - N_-}{N}.$$

The error is then given by, [59]

$$(\Delta A)^2 = \frac{1}{N}\left[\frac{N_+(N - N_+)}{N^2} + \frac{N_-(N - N_-)}{N^2} + \frac{2N_+N_-}{N^2}\right].$$

We note the following limiting cases:

1. μ_+, μ_- always in opposite hemispheres– $N_+ + N_- = N$

$$(\Delta A)^2 = \frac{1}{N}\frac{4N_+N_-}{N^2} = \frac{1 - A^2}{N}$$

2. μ_+, μ_- independent random variables– $N_+ + N_- = N/2$

$$(\Delta A)^2 = \frac{1}{2N}$$

The actual error is close to the first case as expected.

Appendix D. μ^* formulae

In this appendix we present some formulae needed for the μ^* limit.

D.1 Decay rate

The calculation of $\mu^* \to \mu\gamma$ is straightforward from the lagrangian 1.3 . Denoting the momentum and spin of the μ^* as p, s , of the final μ by q, r, and the momentum and polarization of the photon by k, ϵ, the matrix element is :

$$\mathcal{M} = \frac{-ieG_\gamma}{2M}(2\pi)^4\delta^4(p-q-k)\Big[\frac{1}{2k^o}\frac{m_\mu}{q^o}\frac{M}{p^o}\Big]^{\frac{1}{2}}\bar{u}(q,r)\sigma_{\alpha\beta}u(p,s)2k^\alpha\epsilon^\beta$$

The decay rate is then,

$$d\Gamma = \frac{4\pi\alpha G_\gamma^2}{4M^2}(2\pi)^4\delta^4(p-q-k)\Big[\frac{1}{2k^o}\frac{m_\mu}{q^o}\frac{M}{p^o}\Big]\frac{1}{2}\sum|\bar{u}(q,r)\sigma_{\alpha\beta}u(p,s)2k^\alpha\epsilon^\beta|^2\frac{d^3qd^3k}{(2\pi)^6}.$$

Since $k\cdot\epsilon = 0$ and neglicting m_μ,

$$\sum|\bar{u}(q,r)\sigma_{\alpha\beta}u(p,s)k^\alpha\epsilon^\beta|^2 = \frac{32p\cdot kq\cdot k}{4m_\mu M}$$

$$d\Gamma = \frac{\pi\alpha G_\gamma^2}{M^2}\delta^4(p-q-k)\frac{d^3kd^3q}{(2\pi)^2}\Big[\frac{1}{2k^o}\frac{m_\mu}{q^o}\frac{M}{p^o}\Big]2\Big(\frac{32p\cdot kq\cdot k}{4m_\mu M}\Big)$$

Then in the rest frame of the μ^*,

$$\frac{d\Gamma}{d\Omega} = \int\frac{\pi\alpha G_\gamma^2}{M^2}\frac{k^2dk\delta^o(M-2k^o)}{(2\pi)^2}\frac{1}{k^oq^op^o}8Mk^oq^ok^o$$

$$= \frac{\alpha G_\gamma^2 M}{8\pi}.$$

D.2 Two body phase space

The cross section for a two body final state involving one massive particle is given in terms of the lorentz invariant matrix element $\mathcal{M}$ by,

$$\frac{d\sigma}{d\Omega} = \frac{1}{(8\pi)^2}\frac{1}{s}|\mathcal{M}|^2\Big(\frac{s-M^2}{s}\Big).$$

D.3 P* PARAMETERIZATION

The μ^* probability density function P^* has two pieces, a gaussian plus the distribution of the second $M_{\mu\gamma}$:

$$P^*(M,m) = \frac{1}{\sqrt{2\pi}r} e^{\frac{-(M-m)^2}{2r^2}} + \rho(M,m)$$

where $r = r(m)$ is the calculated mass resolution. The function ρ can be calculated from simple kinematics.

In the laboratory frame, the $\mu\mu^*$ are produced with momenta of magnitude $p = (s - M^2)/(2\sqrt{s})$. Let the μ^* momentum be in the $-\hat{z}$ direction, and the μ momentum be along the $+\hat{z}$ direction. Now consider the decay of the μ^* in its rest frame. Denoting the 4-momentum of the muon from this decay (μ') by q' and that of the photon by k' , these momenta are,

$$k' = \frac{M}{2}(1, \cos\theta, \sin\theta)$$

$$q' = \frac{M}{2}(1, -\cos\theta, -\sin\theta)$$

Boosting to the lab frame by the velocity of the μ^* in the lab , $\beta = (s-M^2)/(s+M^2)$ we have,

$$k^o = \frac{\gamma M}{2}(1 - \beta\cos\theta) \qquad q^o = \frac{\gamma M}{2}(1 + \beta\cos\theta)$$

$$k_{||} = \frac{\gamma M}{2}(\cos\theta - \beta) \qquad q_{||} = \frac{\gamma M}{2}(-\cos\theta - \beta)$$

where $\frac{\gamma M}{2} = \frac{s+M^2}{4\sqrt{s}}$. We can now calculate the mass $m^2 = M^2_{\mu\gamma}$ in terms of the production angle θ in the μ^* rest frame. (It is easily checked that $M^2_{\mu'\gamma} = (k'+q')^2 = (k+q)^2 = M^2$.)

$$m^2 = (k+p)^2 = 2k \cdot p = 2\frac{\gamma M}{2} p[1 + \beta - \cos\theta(1+\beta)]$$

$$= \frac{1}{2}(s - M^2)(1 - \cos\theta)$$

Since we know that the decay $\mu^* \to \mu\gamma$ is isotropic the desired probability density function is,

$$1 = \frac{1}{2}\int_{-1}^{1} d(\cos\theta) = \frac{1}{2}\int_{0}^{M_{max}} \left(\frac{dm}{d\cos\theta}\right)^{-1} dm = \int \rho(m)dm.$$

We therefore have,

$$\rho(m) = \frac{2m}{s - M^2}\,, \qquad M_{max} = \sqrt{s - M^2}$$

We can further improve our parameterization by introducing a gaussian smearing and replacing $\rho \to \rho_s$,

$$\rho_s(m) = \int_0^a \rho(m')R(m,m')dm'$$

where $a = s - M^2$ and R is a gaussian centered at m with width $r(m)$. For $a - m \gg r$ we have $\rho_s \approx \rho$ and for $a - s \sim r$,

$$\lim_{a-m\sim r} \rho_s(m) \approx \rho(m)\left[\frac{1}{2}erf(u) + \frac{1}{2} + \frac{1}{2}\sqrt{\frac{2}{\pi}}\frac{r}{m}e^{-u^2}\right]$$

where $u = (a-m)/(\sqrt{2}r)$ and the error function is defined by $erf(u) = \frac{2}{\sqrt{\pi}}\int_0^u e^{-x^2}dx$.

REFERENCES

1. Y. S. Tsai,SLAC-PUB-2741(1981).
2. S.J. Brodsky,C.E. Carlson, and R. Suaya, Phys. Rev. D 14(1976)2264.
3. T. F. Walsh and P. Zerwas, Phys. Lett. 44*B*(1973)195.
4. K. Sasaki, Phys. Rev. D 24(1981)1177; E. Laermann, T.F. Walsh, I. Schmitt, and P. M. Zerwas, Nucl. Phys. B207(1982)205;J.R. Cudell, F. Halzen, and F. Herzog, Phys Lett 140B(1984)83.
5. S.J. Brodsky and S. D. Drell, Ann. Rev. Nucl. Sci. *v*.20,(1970)147.
6. M. Consoli, S. Lo Presti and L. Maiani, Nucl. Phys. *B*223 (1983) 474.
7. Precision tests of the electroweak theory at the Z, G. Altarelli *et al.*,CERN 86-02,Volume 1(1986)
8. G. Putzolu, Il Nuovo Cimento, Vol. XX,N.3(1961)542
9. F.A. Berends and R. Kleiss, Nucl. Phys. *B*177 (1981)257.
10. F. E. Low, Phys. Rev. Lett., 15,238(1965)
11. A. Litke,Ph.D. Thesis,Harvard Univ. 1970 (unpublished).
12. That the choice of a minus sign, which implies a non-hermitian hamiltonian can lead to a unitary S-matrix was first shown by T. D. Lee and G. C. Wick, Nucl. Phys. *B*9(1969)209.
13. For a review see L. Lyons, Progress in Particle and Nuclear Physics, 10(1983)227.
14. A. De Rujula and B. Lauthrup, Lett. Nuovo Cimento, 3 (1972)49; H. Goldberg, Phys. Rev. D.,24(1981)1991
15. S. J. Brodsky and S. D. Drell, Phys. Rev. D, 22(1980) 2236.
16. F. Combley, *et al.*, Phys. Rep. 68(1981)93.
17. M. Suzuki, Phys. Lett. 143*B*(1984)237; H. Terazawa, M. Yashe, K. Akama, M. Hayashi, Phys. Lett. 112*B* (1982)387.
18. F. M. Renard, Phys. Lett. 116*B*(1982)264.
19. There remains, however, the problem of parity doubling, which would require the existence of a light partner to the muon. See S. J. Brodsky and S. D. Drell, Phys. Rev. D 22(1980)2236.

20. UA1 coll., G. Arnison *et al.*, Phys. Lett. 126*B*(1983)398; UA1 coll., P. Bagnaia *et al.*, Phys. Lett. 129*B*(1983)130; UA1 coll., G. Arnison *et al.*, Phys. Lett. 135*B*(1984)250.

21. F. A. Berends and P. H. Daverveldt Nucl. Phys. *B*272 (1986) 131.

22. G. Hanson *et al.*, Phys. Rev. Lett., 35 (1975)1609.

23. E. Fernandez, *et al.*, Phys. Rev. D 31(1985)1537.

24. F. E. Close, Introduction to quarks and partons, Academic Press, San Francisco(1979).

25. J. R. Cudell, F. Halzen, and F. Herzog, Phys. Lett. 140*B* (1984)83.

26. T. Jayaraman, G. Rajasekaran, and S.D. Rindani, Phys. Rev. D, 32(1985)1262; X. He,S. Pakvasa,G. Rajasekaran, submitted to XXIII International Conference of High Energy Physics , Berkeley (1986).

27. R. H. Schindler *et al.*, Phys. Rev. D 24(1981)78.

28. J. Jaros in Proceedings of the International Conference on Instrumentation for Colliding Beam Physics, SLAC-Report 250, edited by W. Ash, Stanford CA, 29 (1982).

29. For a description of the various detector configurations at PEP see M. E. Nelson, Ph. D. Thesis, U. of California, Berkeley(1983) (unpublished).

30. J. Jaros, Proceedings of Int. Conference for Instrumentation for Colliding Beam Physics, SLAC Report 250, edited by W. Ash, Stanford (1982).

31. W. Davies-White *et al.*, Nucl. Instr. and Meth. 160.(1979)227.

32. W. J. Willis and V. Radeka, Nucl. Instr. Meth. 120(1974) 221.

33. G. S. Abrams et. al., IEE Trans. Nucl. Sc., $ns-25$, no. 1(1978)309.

34. K. G. Hayes, Ph.D. Thesis, Stanford University, SLAC-Report-2371 (1981) (unpublished).

35. T. Himel, Ph.D. Thesis, Stanford University, SLAC-223(1979)(unpublished).

36. F. A. Berends and R. Kleiss, Nucl. Phys. *B*228 (1983) 537.

37. N. Lockyer, MARKII internal memorandum, June 21, 1984

38. F. Gutbrod and Z. J. Rek, Z. Phys. c1,(1979)171.

39. C. Weizsäcker and E. T. Williams, Z. Physik. 88(1934) 612.

40. J. D. Jackson, Classical Electrodynamics John Wiley and Sons, Inc., N.Y.(1975).

41. G. Bonneau and F. Martin, Nucl. Phys. *B*27 (1971)381.

42. F. A. Berends and R. Kleiss, Nucl. Phys. *B*178 (1981) 141.

43. F. Block and A. Nordsieck, Phys. Rev. 52(1937)54.

44. Y. S. Tsai SLAC-PUB-3129 (1983).

45. This argument is due to Y. S. Tsai, private communication.

46. It is interesting to note that this procedure breaks down at $t_e = 1$. This is the so-called Landau singularity which implies that even pure QED must break down and become inconsistent at sufficiently high energy. The result also follows from considering the running coupling constant which becomes greater then 1 at sufficiently high energy implying the breakdown of perturbation theory. For any accessible energy, t_e is very small. $t_e(29\text{ GeV}) \approx .1$ and the value at which $t_e = 1$ is 10^{43} GeV which is much larger then even the Planck mass. It has been proposed that under special circumstances such as the process $e^+e^- \rightarrow Z^o\gamma$ perturbation theory will break down very much sooner, at laboratory energies just above the Z mass. See N. Dombey, J. Cole, and F. Boudjema, Phys. Lett. 167*B* E(1986)108.

47. F. A. Berends, R. Kleiss, and S. Jadach, Nucl. Phys. *B*202 (1982)63.

48. W. T. Ford *et al.*, Phys. Rev. Lett. 51(1983)257.

49. W. Bartel *et al.*, Z. Physics C 24(1984)223.

50. Cello Collab.,F. A. Beherend et. al., DESY 84-101,(1984).

51. M. C. Peyranere, J. Layssac and F. M. Renard, Phys. Lett. 158B(1985)276.

52. The error on this number comes from binomial statistics and is given by the formula, $\Delta w = \frac{1}{\sqrt{N}} \frac{\sqrt{w(1-w)}}{2(2w-1)}$.

53. Jerome H. Friedman, J. Comp. Phys.,7 (1971)201; Roger Chaffee, SLAC Computation Group Technical Memo No. 195 (1979).

54. F. A. Berends and R. Kleiss, Nucl. Phys. *B*178 (1981)141.

55. F. James and M. Ross MINUIT, CERN program library No. D506.

56. P. C. Rowson, Ph.D. Thesis,U. of California, Berkeley,1985 (unpublished)

57. B. Andersson *et al.*, Phys. Rep. 97(1983)31.

58. R.D. Field and R.P. Feynman, Nucl. Phys. B136(1978)1

59. See, for example, A. G. Frodesen, O. Skjeggestad, and H. Tøfte, Probability and Statistics in Particle Physics ,Universitetsforlaget,Bergen(1979).

This report was done with support from the Department of Energy. Any conclusions or opinions expressed in this report represent solely those of the author(s) and not necessarily those of The Regents of the University of California, the Lawrence Berkeley Laboratory or the Department of Energy.

Reference to a company or product name does not imply approval or recommendation of the product by the University of California or the U.S. Department of Energy to the exclusion of others that may be suitable.

LAWRENCE BERKELEY LABORATORY
TECHNICAL INFORMATION DEPARTMENT
UNIVERSITY OF CALIFORNIA
BERKELEY, CALIFORNIA 94720